Supporting Information

Five Shades of Green: Substituent Influence on the (Spectro-) Electrochemical Properties of Diferrocenylphenyl Methylium Dyes

Larissa A. Casper, [a] Viktoria Ebel[a], Michael Linseis[a], and Rainer F. Winter*[a]

Table of Contents

Figure S1: Top: Picture taken of complex cations **1⁺**-**5⁺** under ambient conditions, demonstrating their stability; Bottom: Comparison of the UV/Vis/NIR spectra of the five cations.

NMR-Spectroscopy

7.35
7.33
6.85
6.83
4.17
4.14
4.10
3.85
3.82
3.26

2.00
2.00
1.94
8.84
2.53
2.00
1.91
2.99
0.94
0.43

7.6 7.4 7.2 7.0 6.8 6.6 6.4 6.2 6.0 5.8 5.6 5.4 5.2 5.0 4.8 4.6 4.4 4.2 4.0 3.8 3.6 3.4 3.2 3.0 2.8 2.6 2.4 2.2 2.0
δ [ppm]
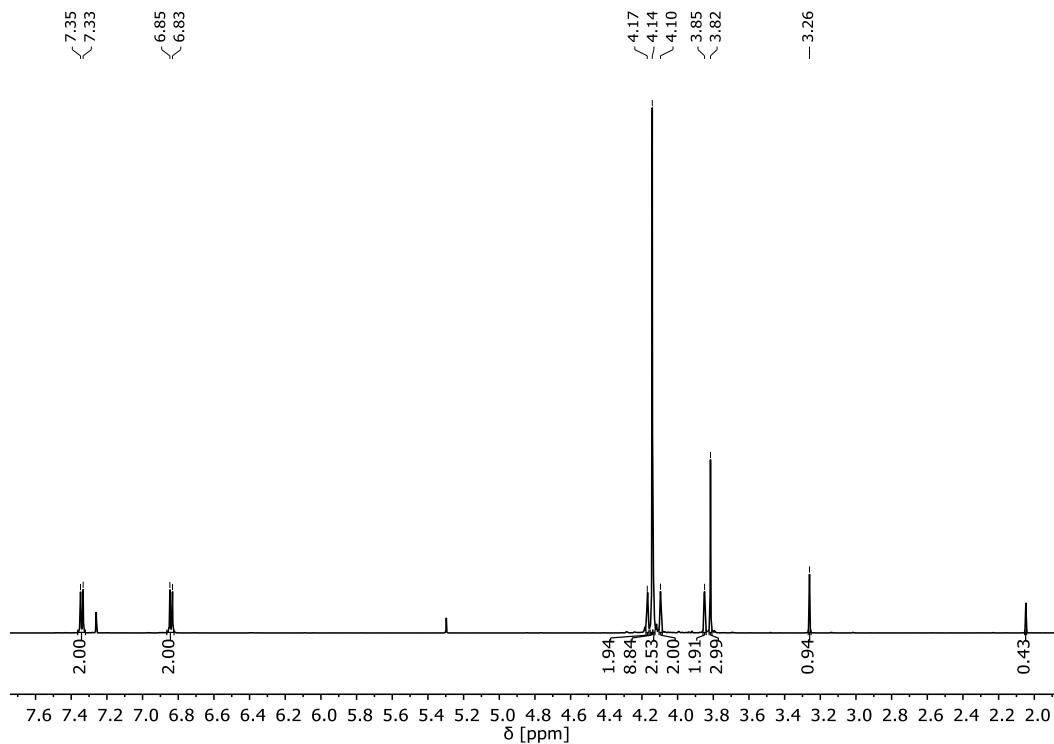
Figure S2: ^{1}H-NMR spectrum of **1-OH** (CDCl$_3$, 400 MHz).

158.14
139.39
127.55
112.37
100.30
73.48
68.76
68.31
68.12
67.50
67.19
55.36

165 160 155 150 145 140 135 130 125 120 115 110 105 100 95 90 85 80 75 70 65 60 55 50
δ [ppm]
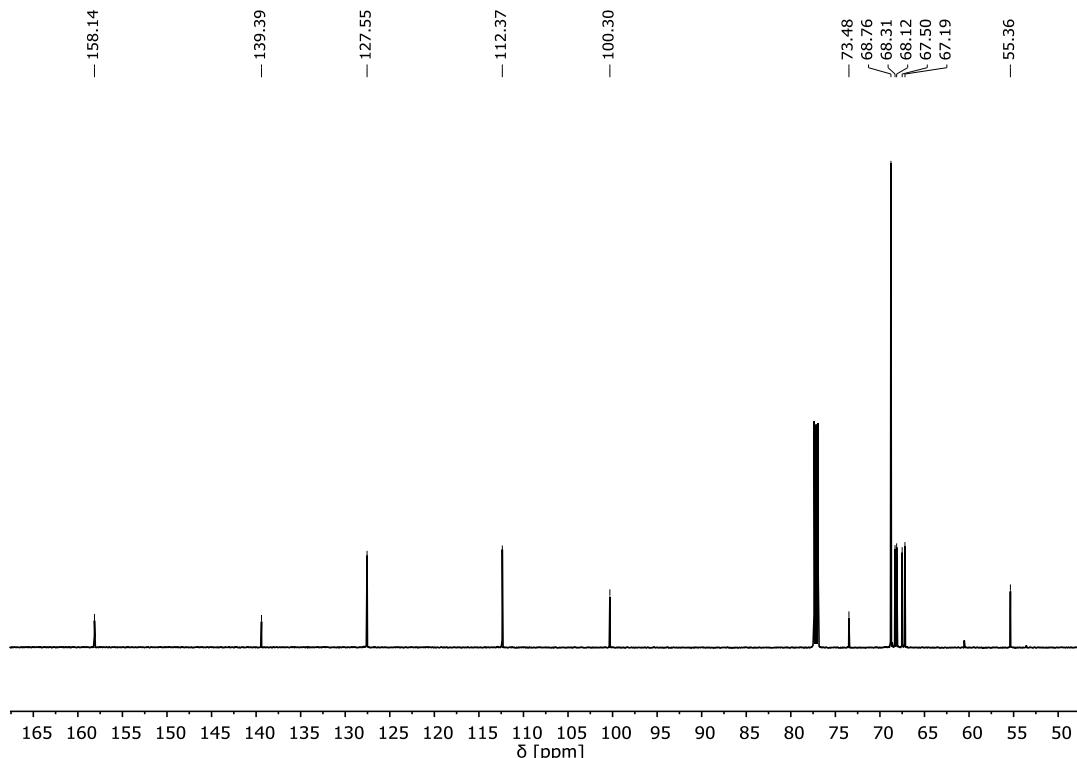
Figure S3: ^{13}C-NMR spectrum of **1-OH** (CDCl$_3$, 400 MHz).

3
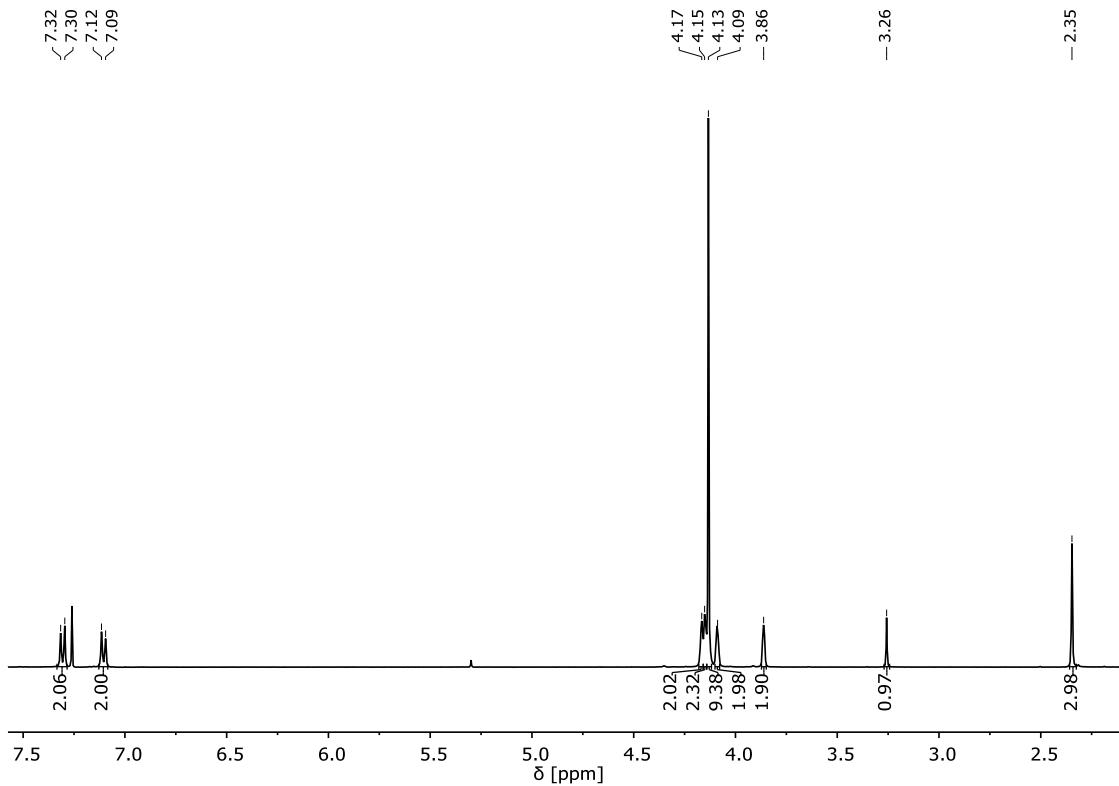
Figure S4: ¹H-NMR spectrum of **2-OH** (CDCl₃, 400 MHz).
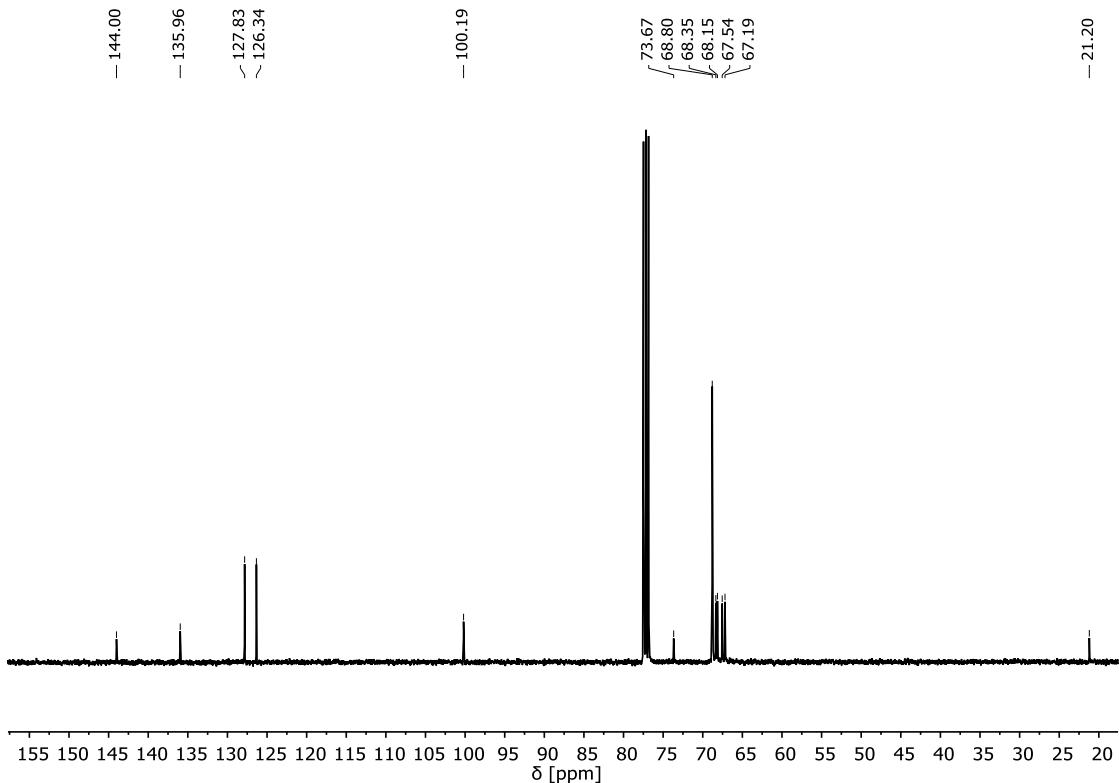
Figure S5: ¹³C-NMR spectrum of **2-OH** (CDCl₃, 400 MHz).

4
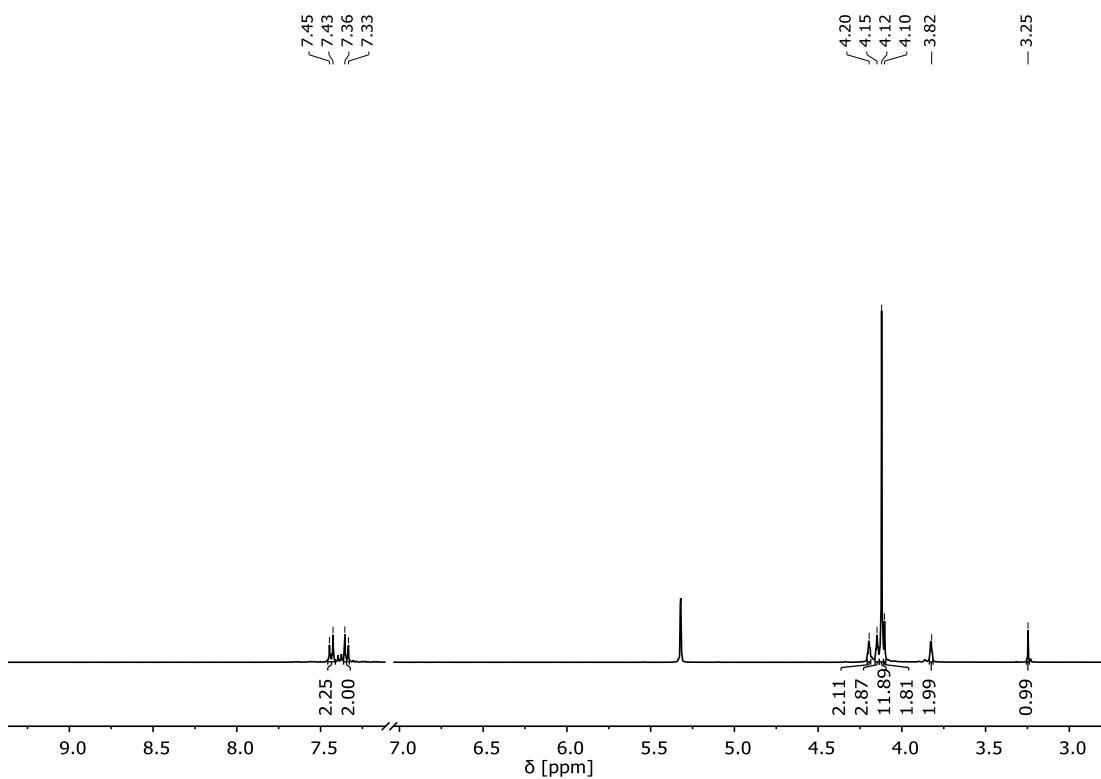
Figure S6: ^{1}H-NMR spectrum of **3-OH** (CD$_2$Cl$_2$, 400 MHz).

Peaks (ppm): 7.45, 7.43, 7.36, 7.33, 4.20, 4.15, 4.12, 4.10, 3.82, 3.25

Integrations: 2.25, 2.00, 2.11, 2.87, 11.89, 1.81, 1.99, 0.99
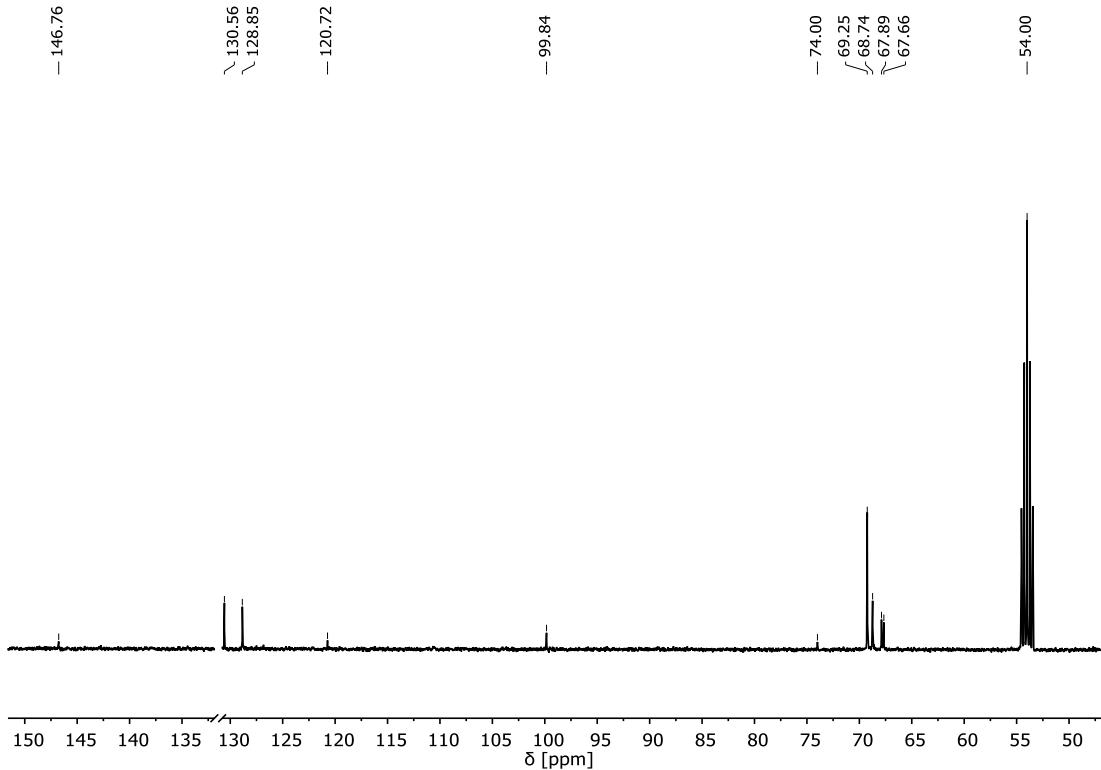
Figure S7: ^{13}C-NMR spectrum of **3-OH** (CD$_2$Cl$_2$, 400 MHz).

Peaks (ppm): 146.76, 130.56, 128.85, 120.72, 99.84, 74.00, 69.25, 68.74, 67.89, 67.66, 54.00

5
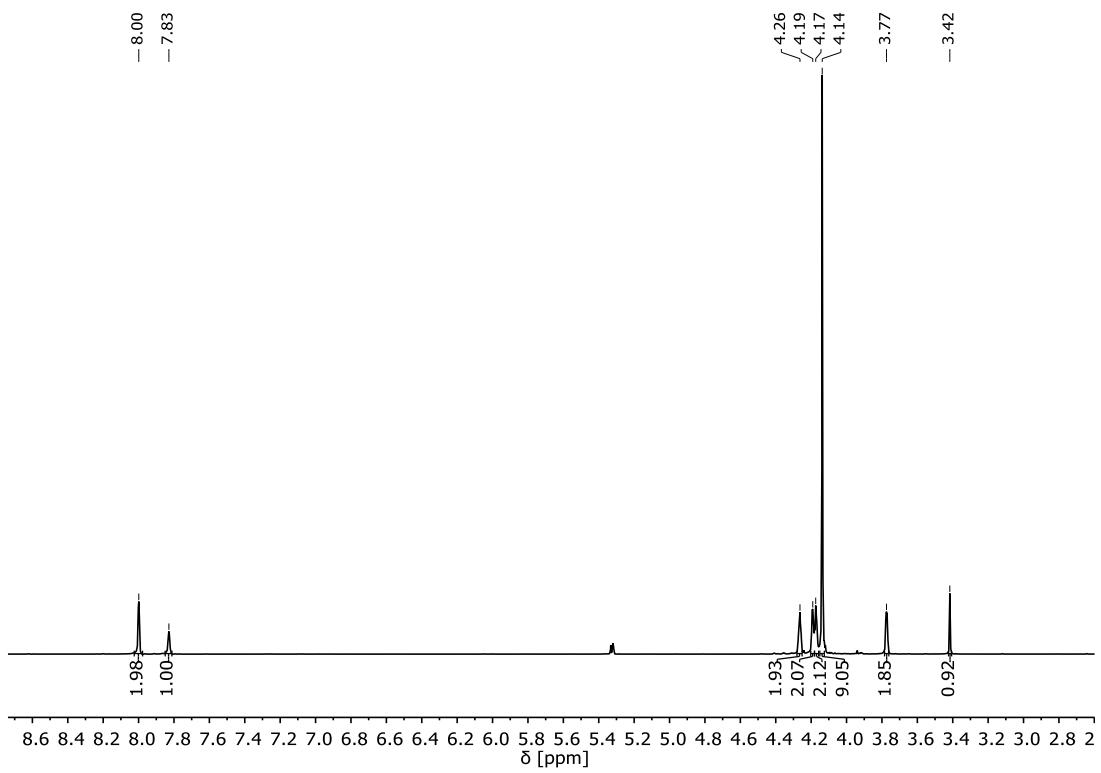
Figure S8: ^{1}H-NMR spectrum of **4-OH** (CD$_2$Cl$_2$, 400 MHz).
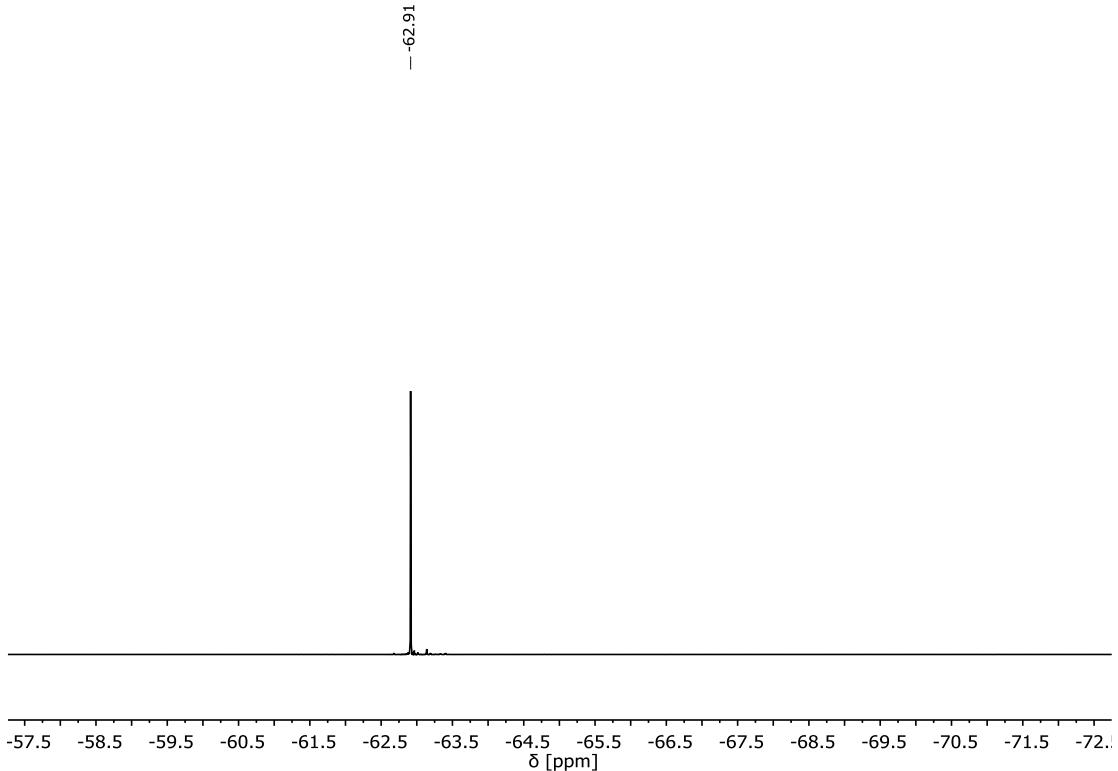
Figure S9: ^{19}F-NMR spectrum of **4-OH** (CD$_2$Cl$_2$, 400 MHz).
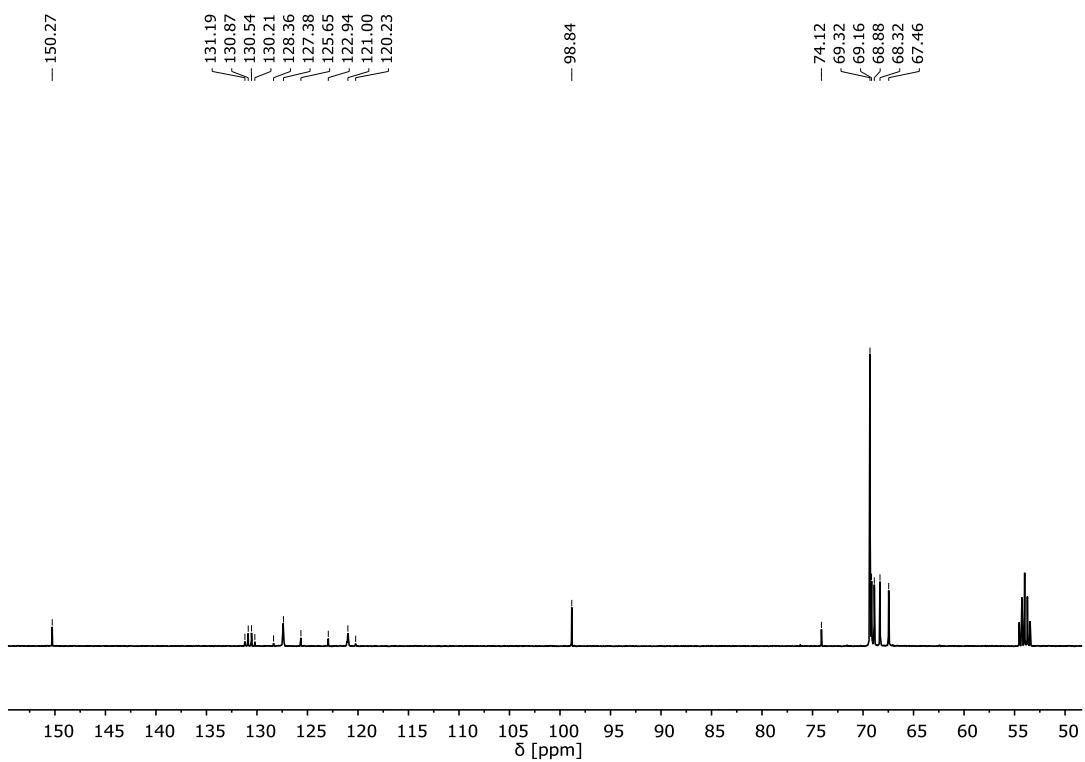
Figure S10: ^{13}C-NMR spectrum of **4-OH** (CD$_2$Cl$_2$, 400 MHz).
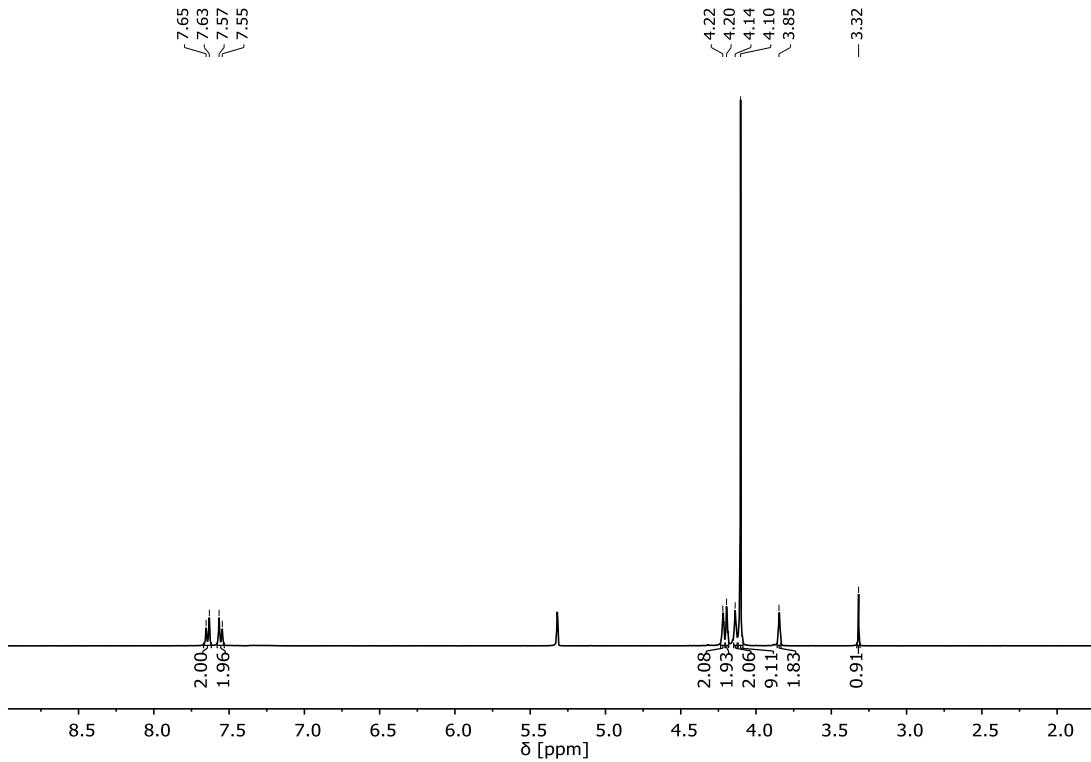
Figure S11: ^{1}H-NMR spectrum of **5-OH** (CD$_2$Cl$_2$, 400 MHz).
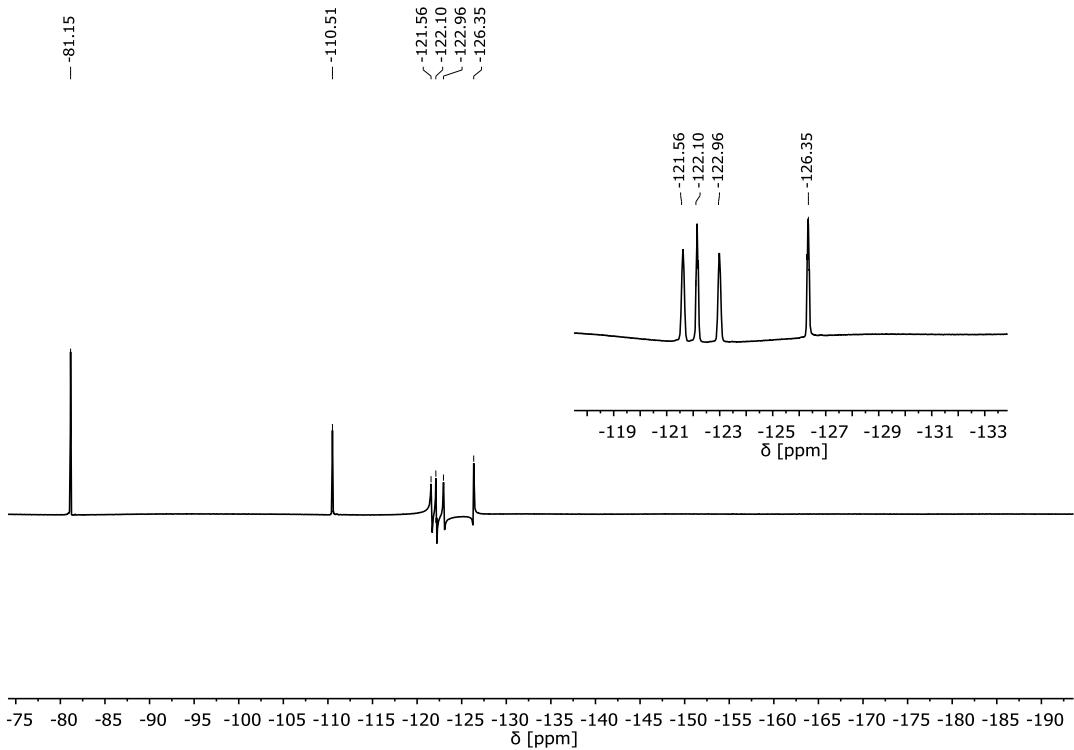
Figure S12: ^{19}F-NMR spectrum of **5-OH** (CD$_2$Cl$_2$, 400 MHz).
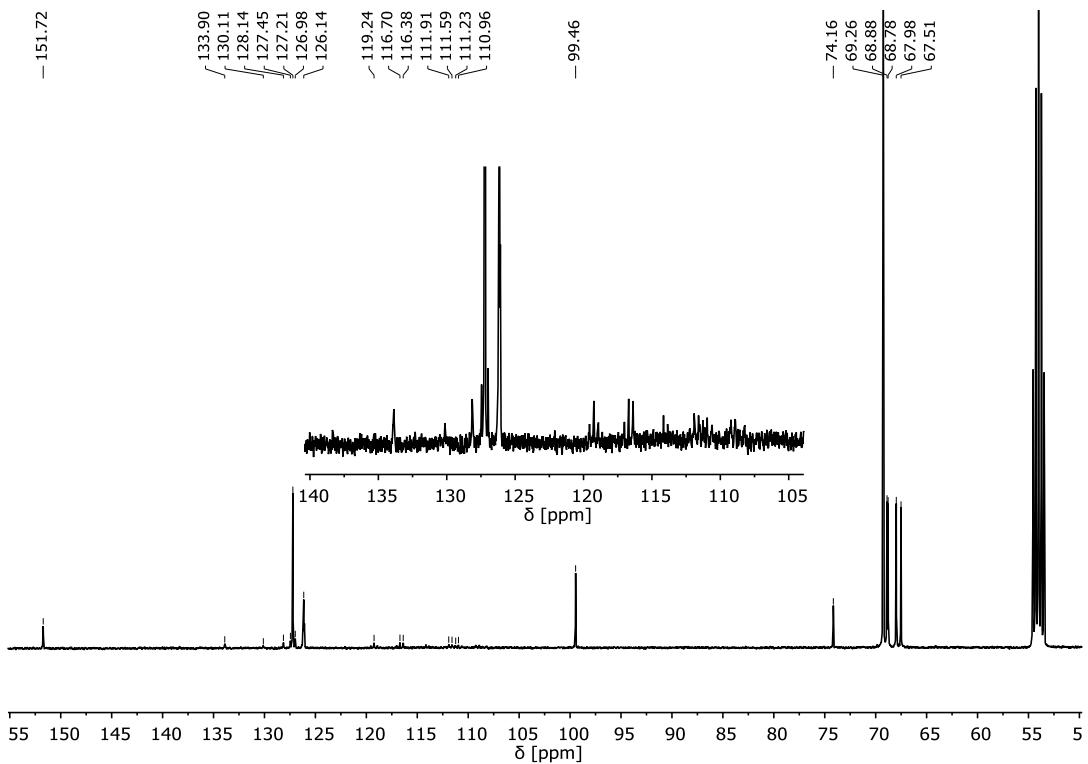
Figure S13: ^{13}C-NMR spectrum of **5-OH** (CD$_2$Cl$_2$, 400 MHz).
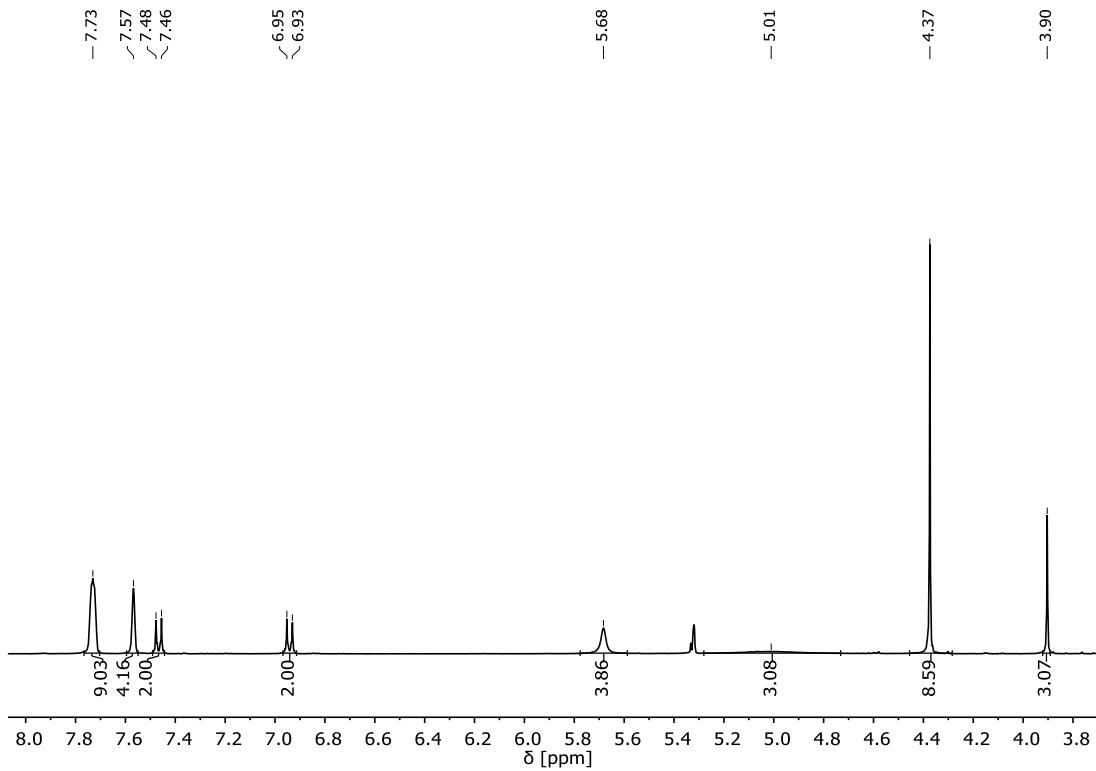
Figure S14: ^{1}H-NMR spectrum of **1$^+$ BAr$^F_{24}$$^-$** (CD$_2Cl_2$, 400 MHz).

Figure S15: ^{13}C-NMR spectrum of **1$^+$ BAr$^F_{24}$$^-$** (CD$_2Cl_2$, 400 MHz).
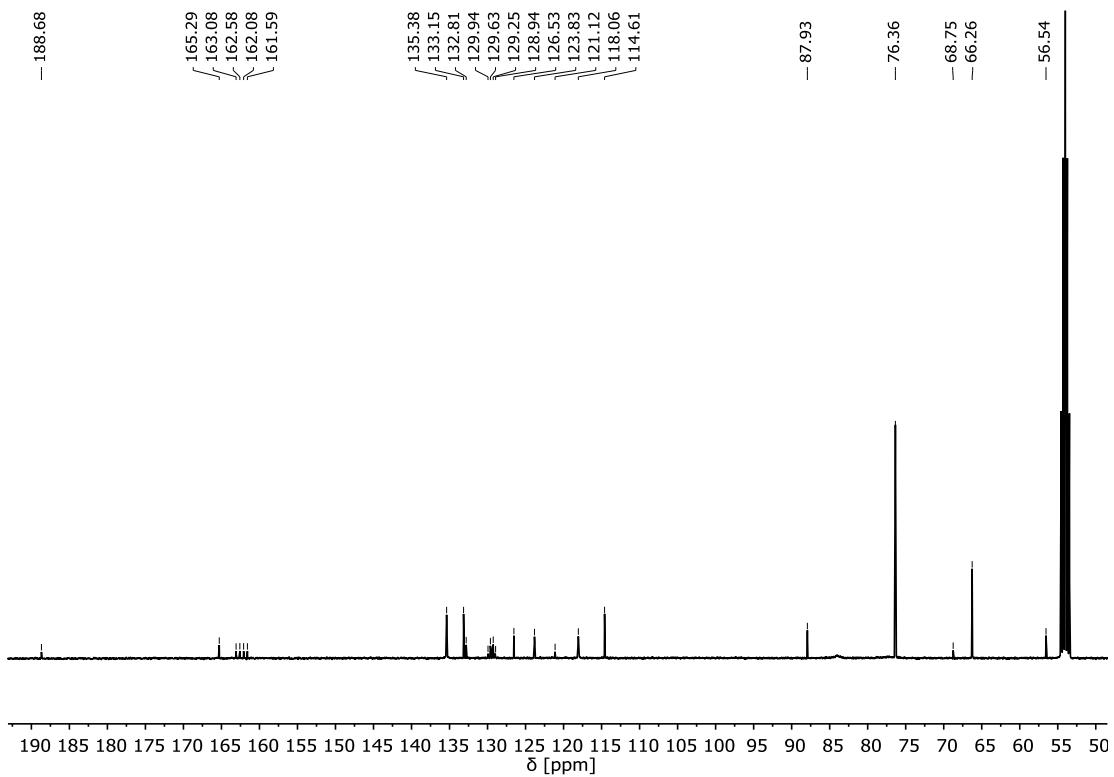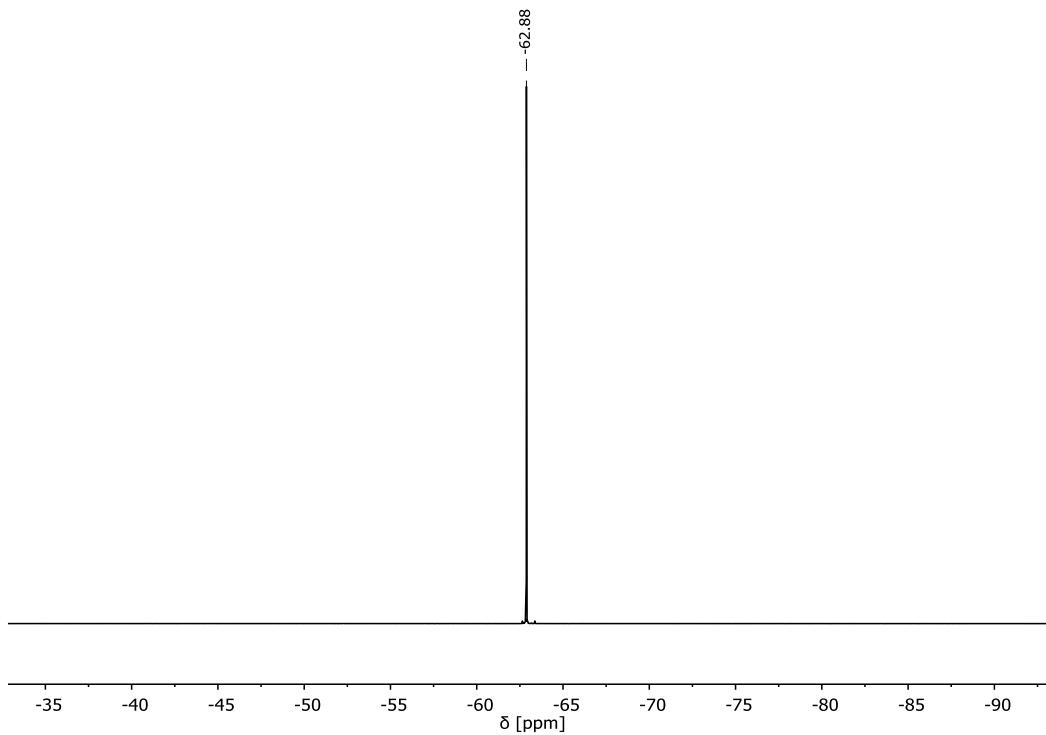
Figure S16: ^{19}F-NMR spectrum of **1$^+$ BArF$_{24}^-$** (CD$_2$Cl$_2$, 400 MHz).
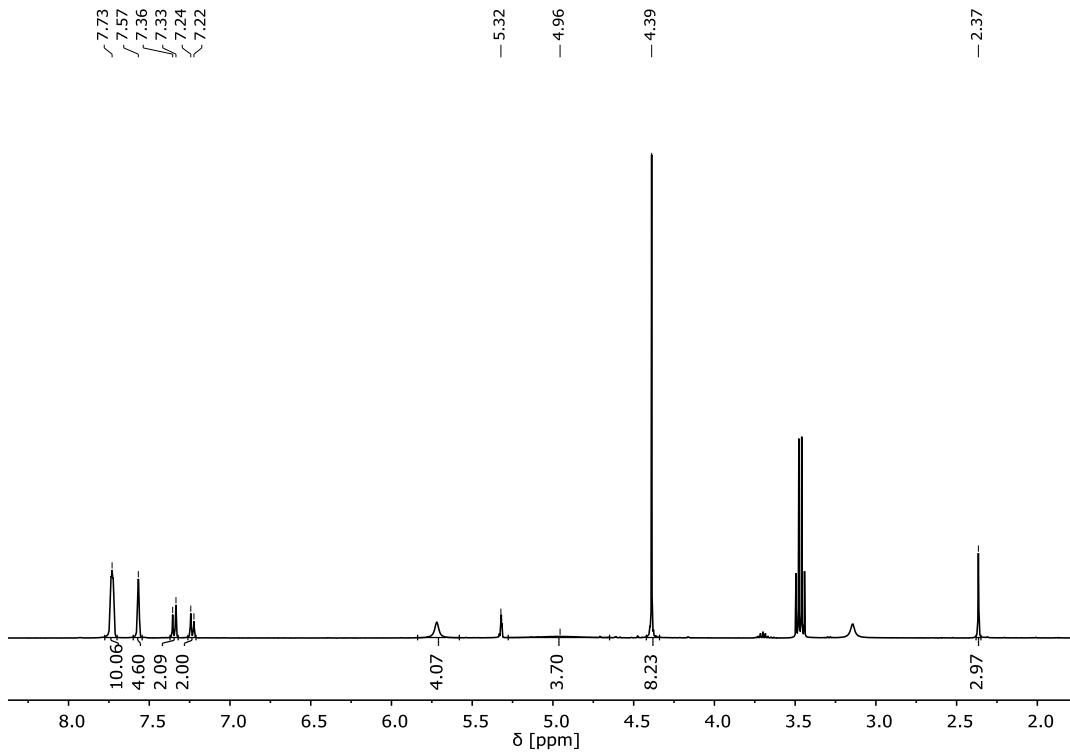
Figure S17: ^{1}H-NMR spectrum of **2$^+$ BArF$_{24}^-$** (CD$_2$Cl$_2$, 400 MHz).
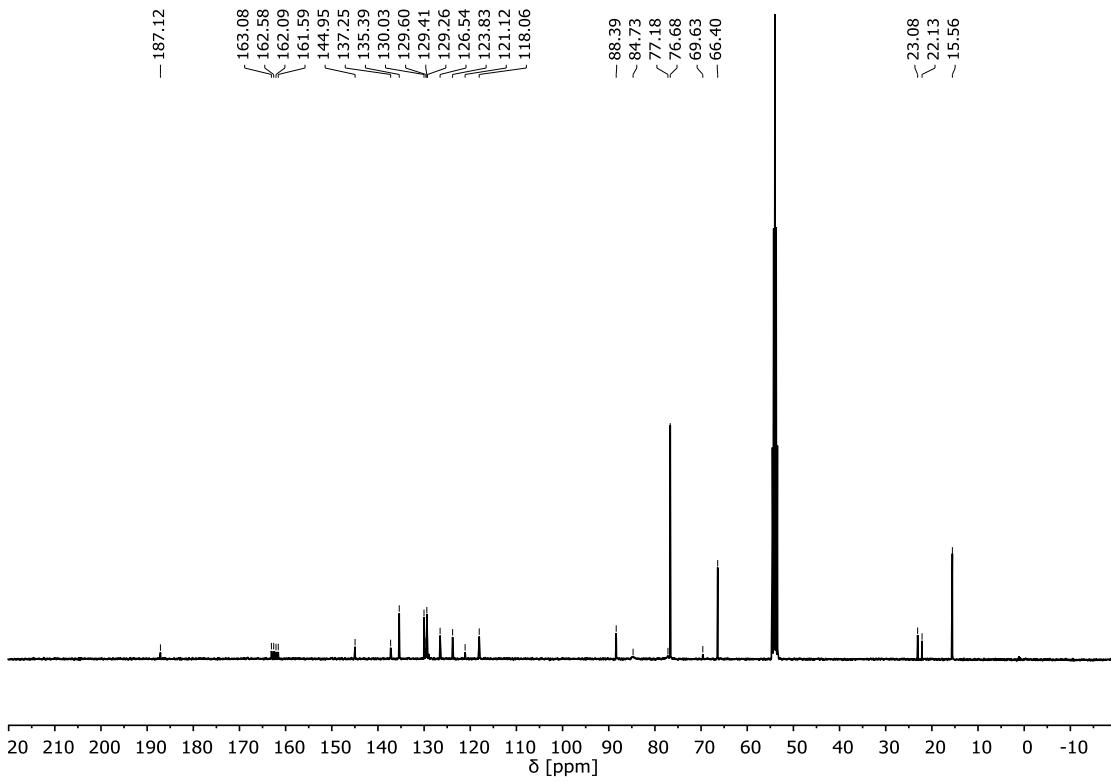
Figure S18: ^{13}C-NMR spectrum of 2^+ BAr$^F_{24}^-$ (CD$_2$Cl$_2$, 400 MHz).
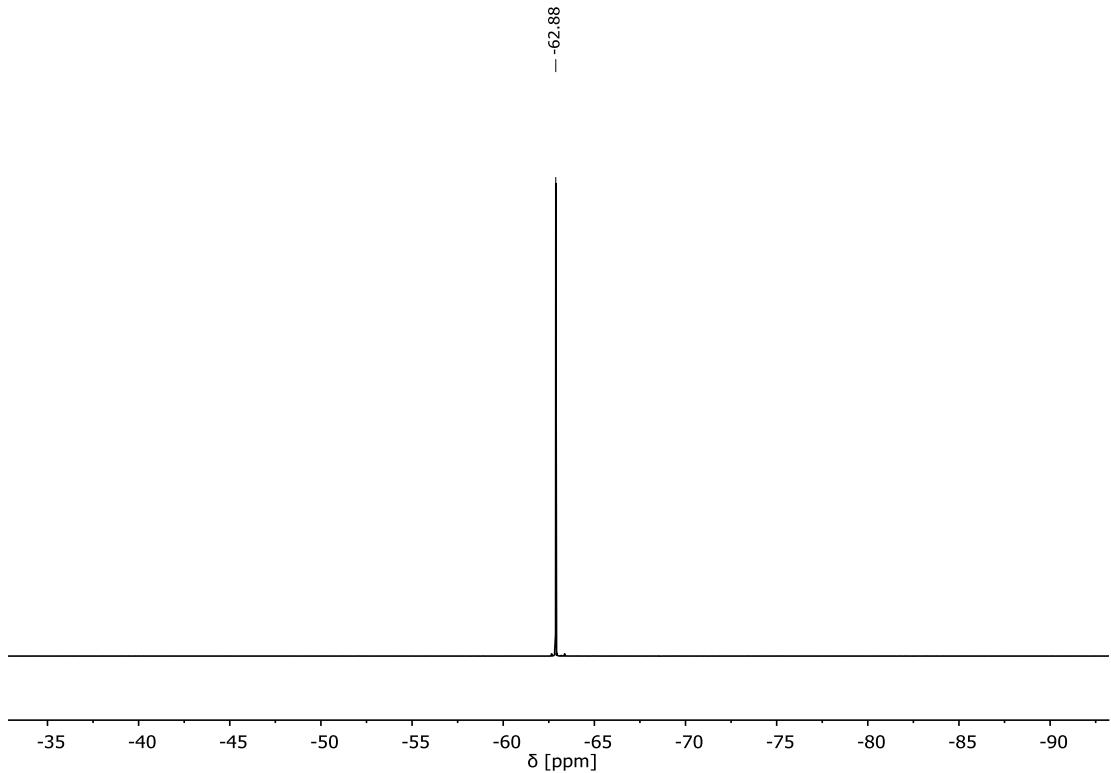
Figure S19: ^{19}F-NMR spectrum of 2^+ BAr$^F_{24}^-$ (CD$_2$Cl$_2$, 400 MHz).

11
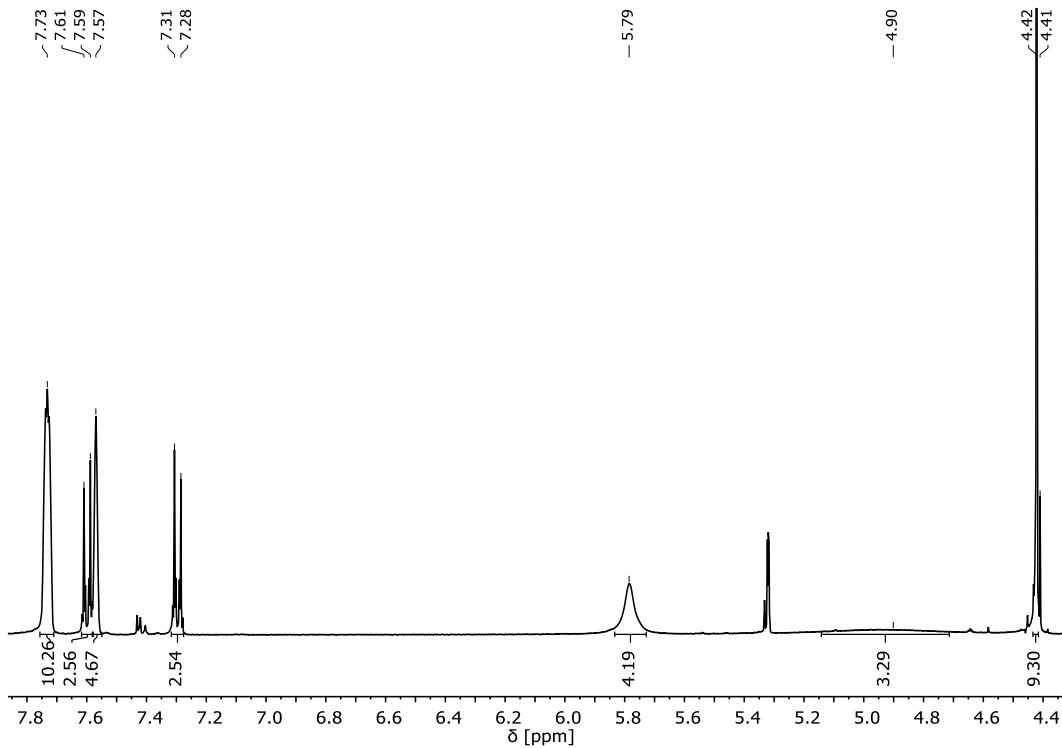
Figure S20: ^{1}H-NMR spectrum of **3$^+$BAr$^F_{24}$** (CD$_2$Cl$_2$, 400 MHz).
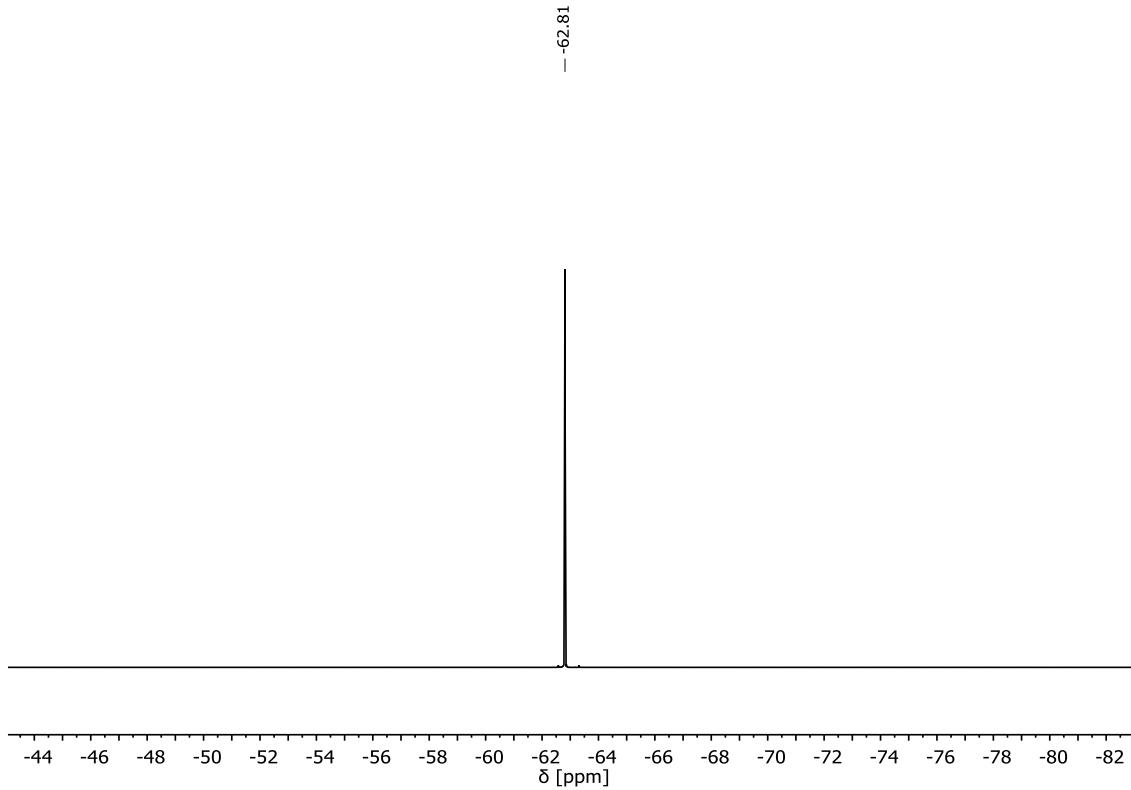
Figure S21: ^{19}F-NMR spectrum of **3$^+$BAr$^F_{24}$** (CD$_2$Cl$_2$, 400 MHz).
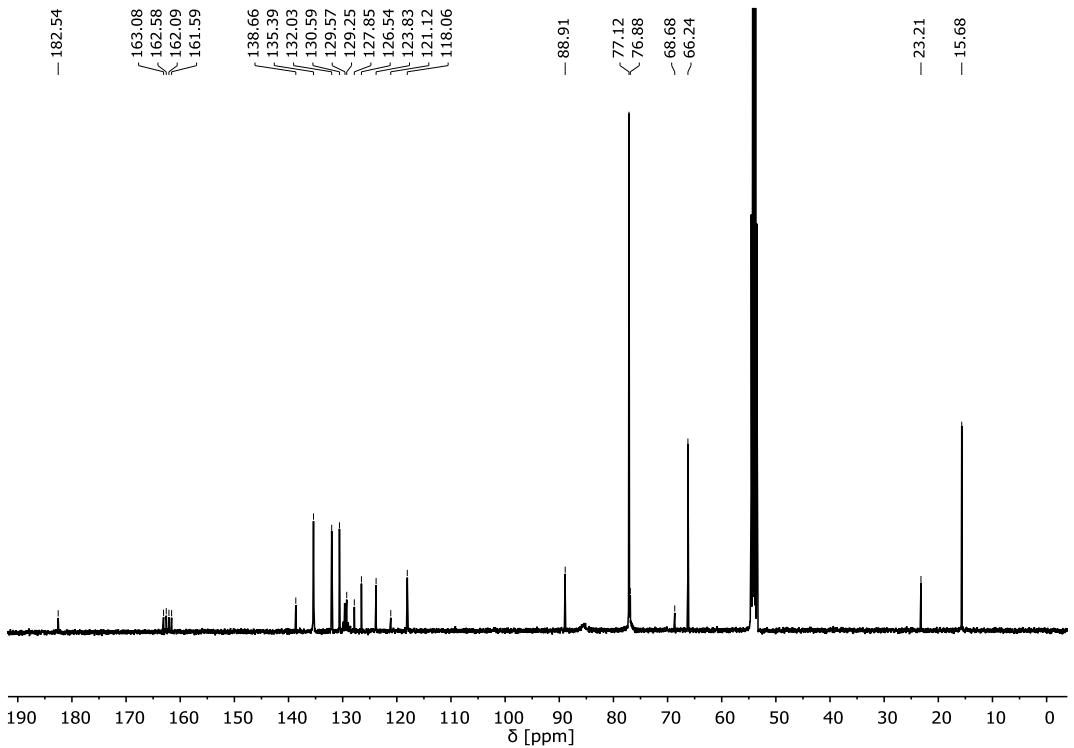
Figure S22: ^{13}C-NMR spectrum of **3$^+$ BAr$^F_{24}$** (CD$_2$Cl$_2$, 400 MHz).
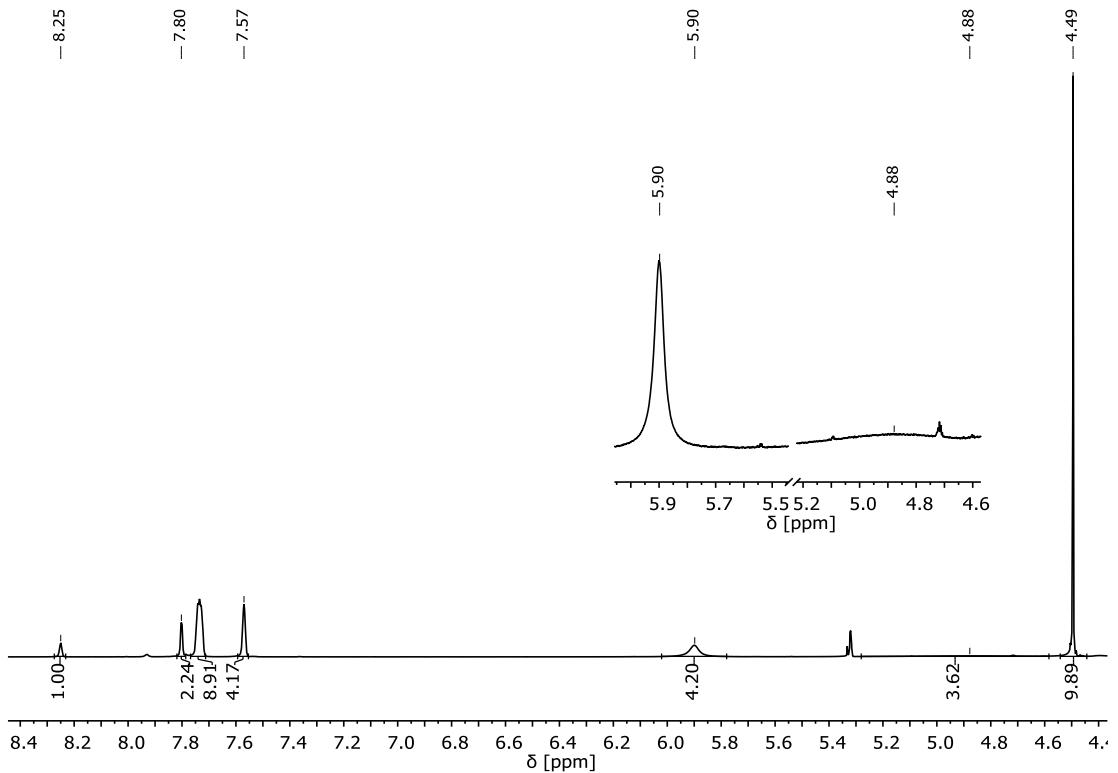
Figure S23: ^{1}H-NMR spectrum of **4$^+$ BAr$^F_{24}$** (CD$_2$Cl$_2$, 400 MHz).
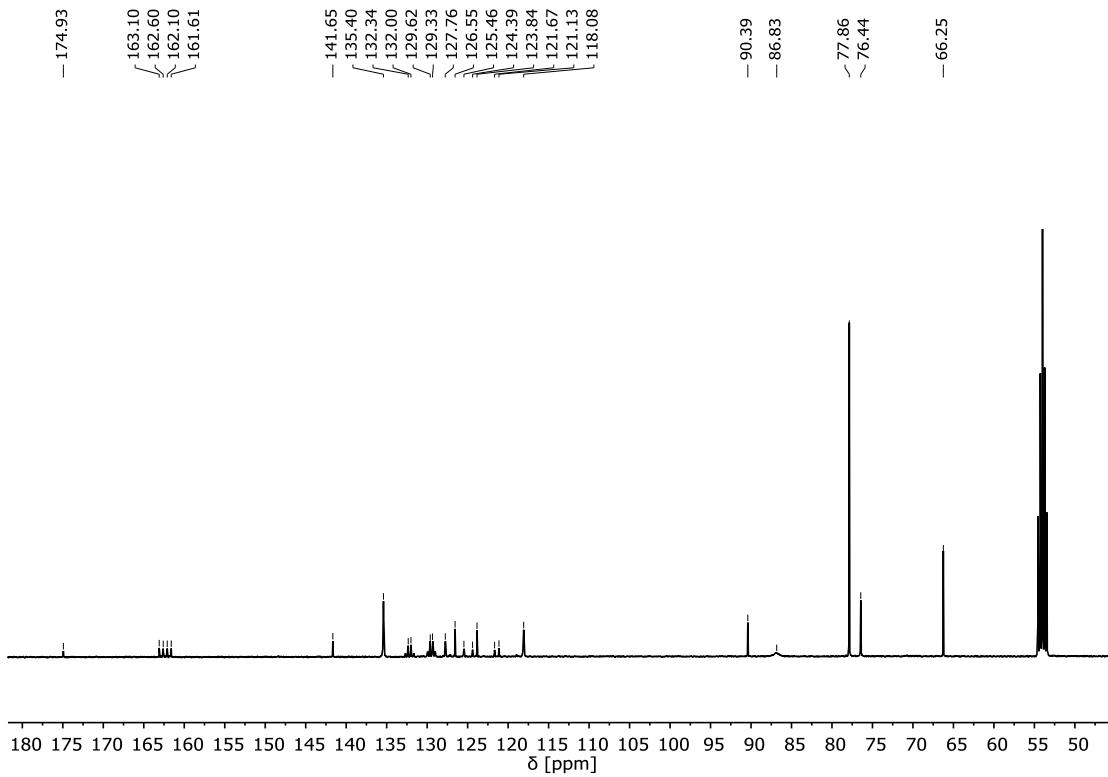
Figure S24: ^{13}C-NMR spectrum of **4$^+$ BAr$^F_{24}$$^-$** (CD$_2Cl_2$, 400 MHz).

Figure S25: ^{19}F-NMR spectrum of **4$^+$ BAr$^F_{24}$$^-$** (CD$_2Cl_2$, 400 MHz).
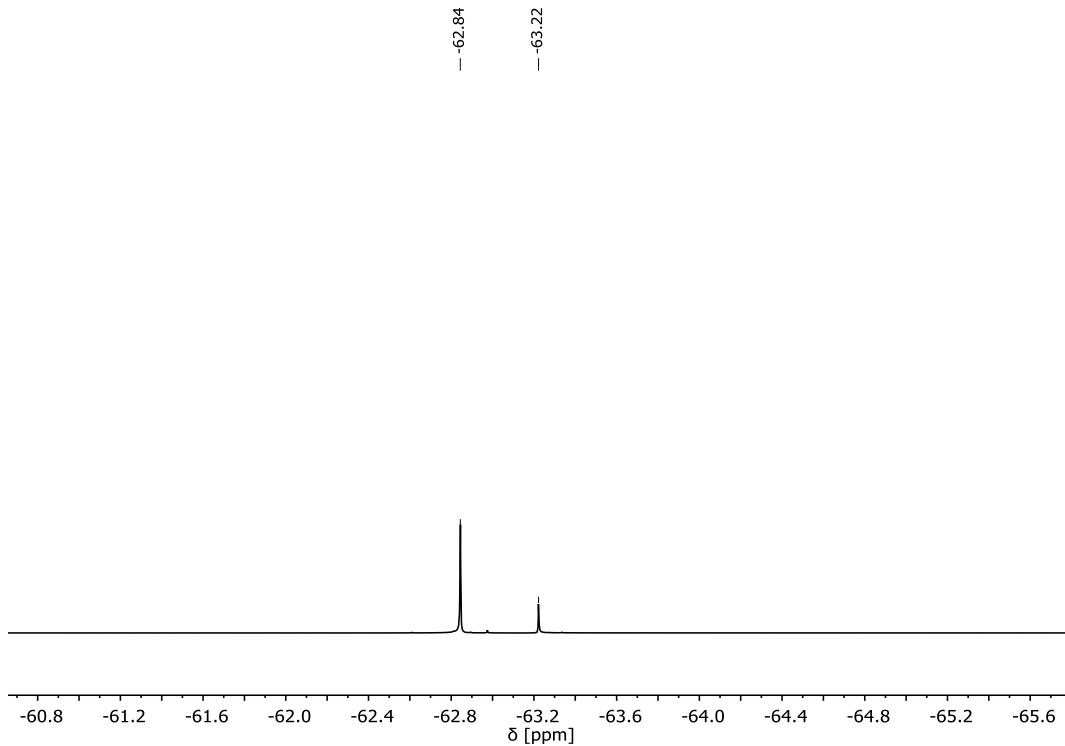
14
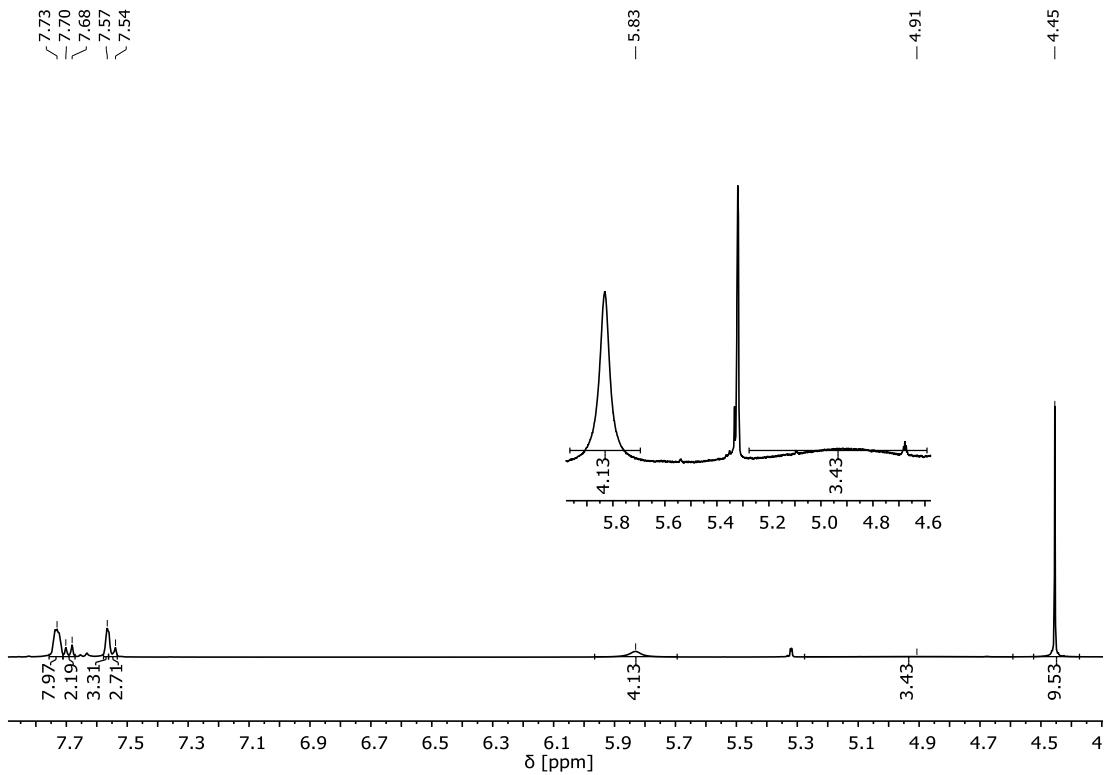
Figure S26: ^{1}H-NMR spectrum of **5$^+$ BAr$^F_{24}$** (CD$_2$Cl$_2$, 400 MHz).
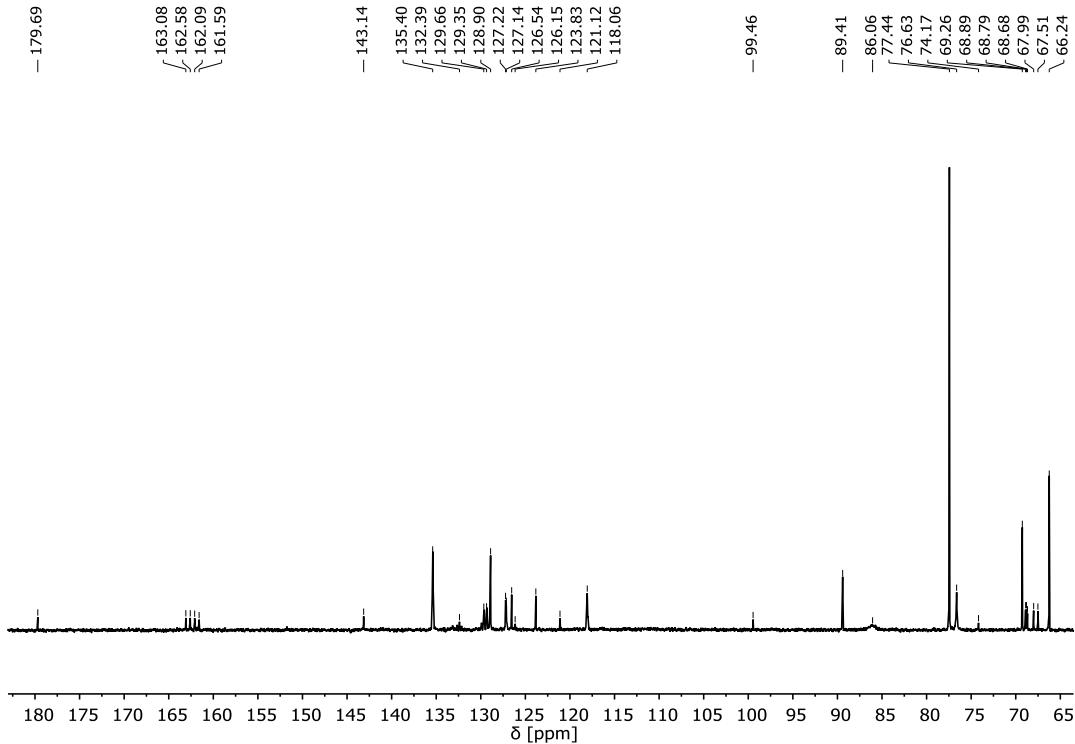
Figure S27: ^{13}C-NMR spectrum of **5$^+$ BAr$^F_{24}$** (CD$_2$Cl$_2$, 400 MHz).

15
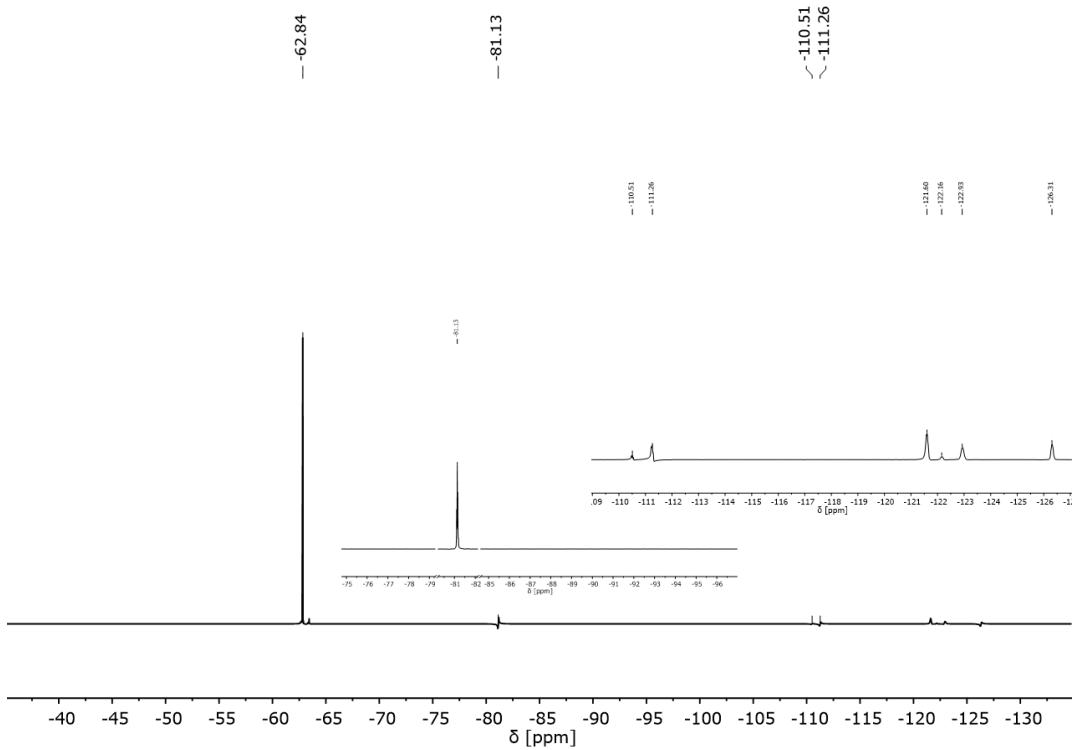
Figure S28: ^{19}F-NMR spectrum of **5$^+$ BAr$^F_{24}$$^-$** (CD$_2Cl_2$, 400 MHz).

Mass Spectrometry

Figure S29: ESI-mass spectrum of **1⁺** (experimental on the top, simulation at the bottom).

Figure S30: ESI-mass spectrum of **2⁺** (experimental on the top, simulation at the bottom).

Figure S31: ESI-mass spectrum of **3⁺** (experimental on the top, simulation at the bottom).

Figure S32: ESI-mass spectrum of **4⁺** (experimental on the top, simulation at the bottom).

Figure S33: ESI-mass spectrum of **5⁺** (experimental on the top, simulation at the bottom).

Hammett Plots: Part I

Figure S34: Hammett plot for the chemical shifts of the resonance signal of the methylium carbon atom C5; σ_p (C_6F_{13}) is here approximated by the pink lines to +0.26 [±0.06].

Figure S35: ^{1}H-NMR spectrum of **2$^+$ BAr$^F_{24}$** between 3 and 6 ppm at different temperatures between 280 K and 330 K (1,2-C$_2$D$_4$Cl$_2$, 600 MHz).

Figure S36: ^{13}C-NMR spectrum of **2$^+$ BAr$^F_{24}$** at 300 K and 330 K in spectral range of the ferrocenyl C atoms (1,2-C$_2$D$_4$Cl$_2$, 600 MHz and CD$_2$Cl$_2$, 400 MHz).

Figure S37: ^{1}H-NMR spectrum of **2$^+$BAr$^F_{24}$$^-$** at different temperatures between 280 K and 330 K with zoom into the ferrocenyl region at the top (1,2-C$_2$D$_4$Cl$_2$, 600 MHz).
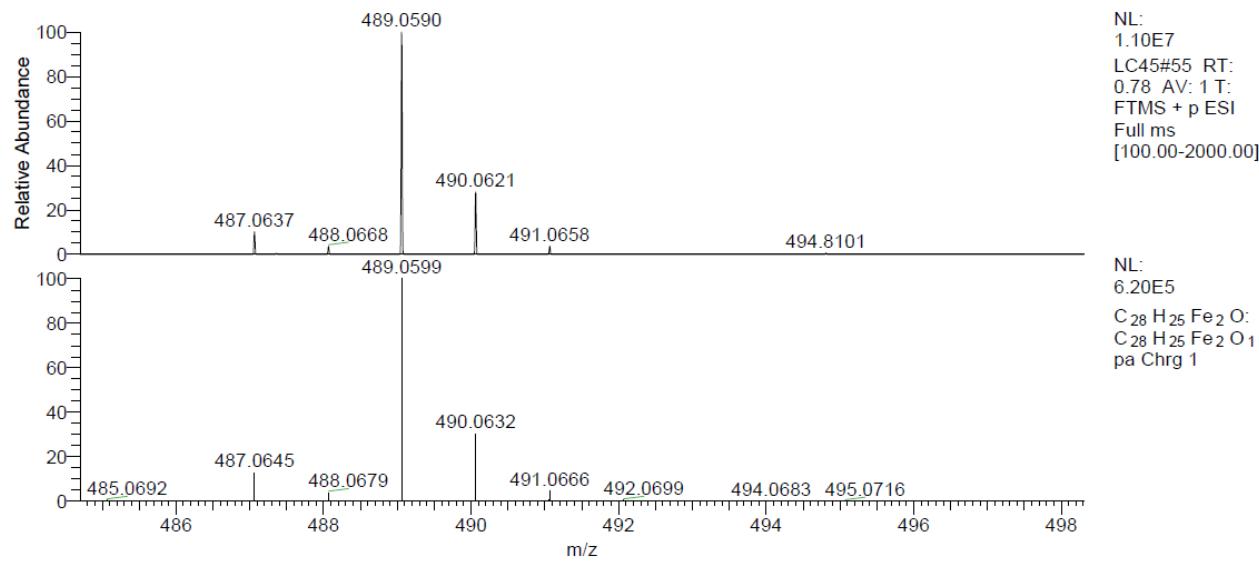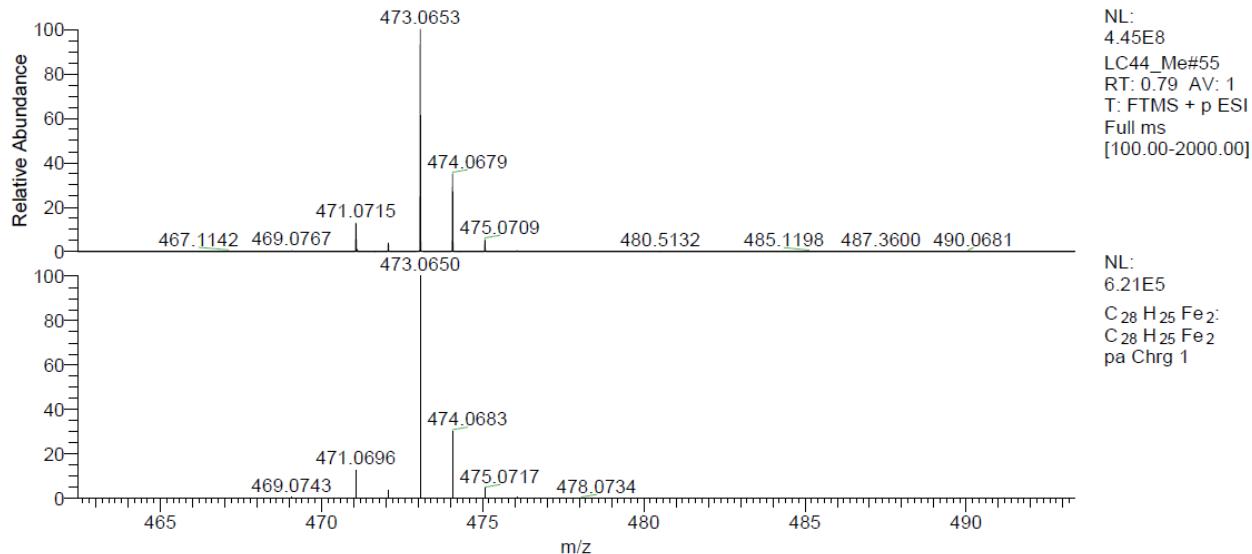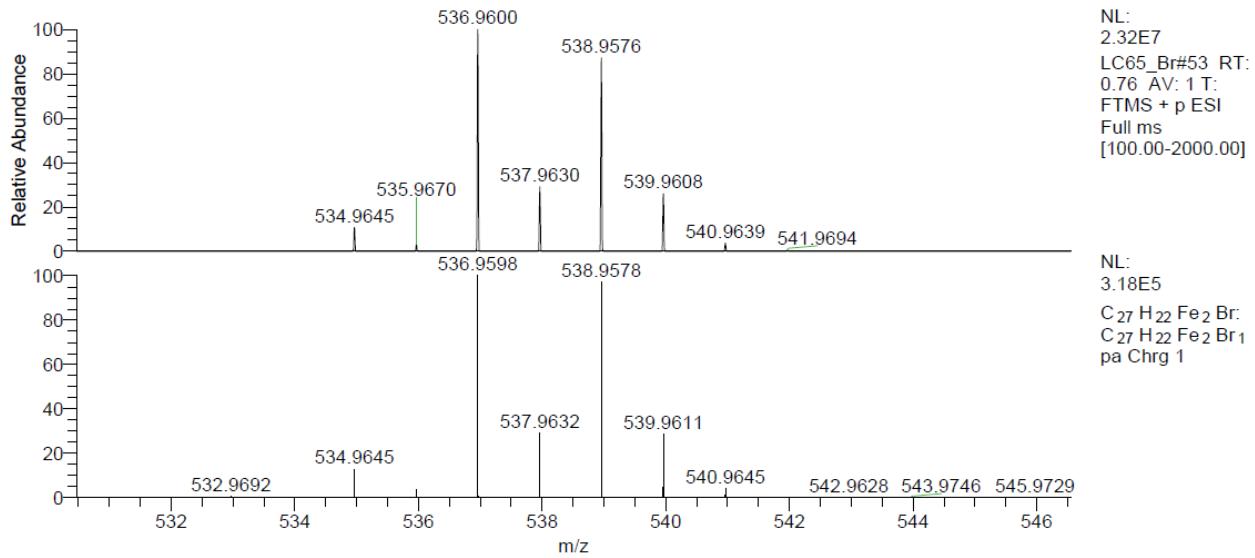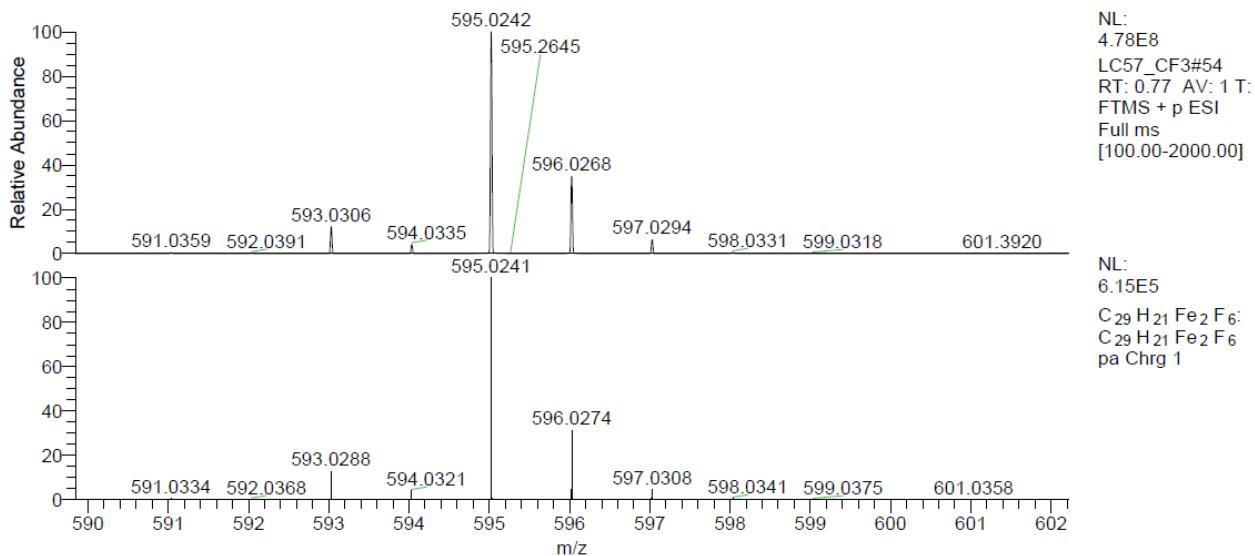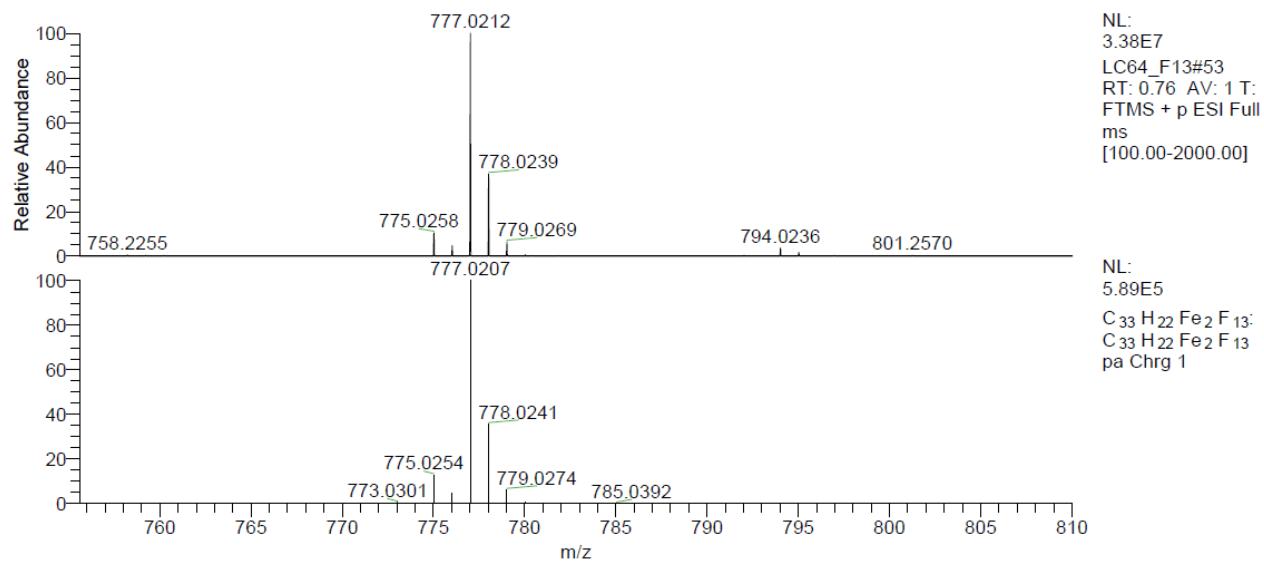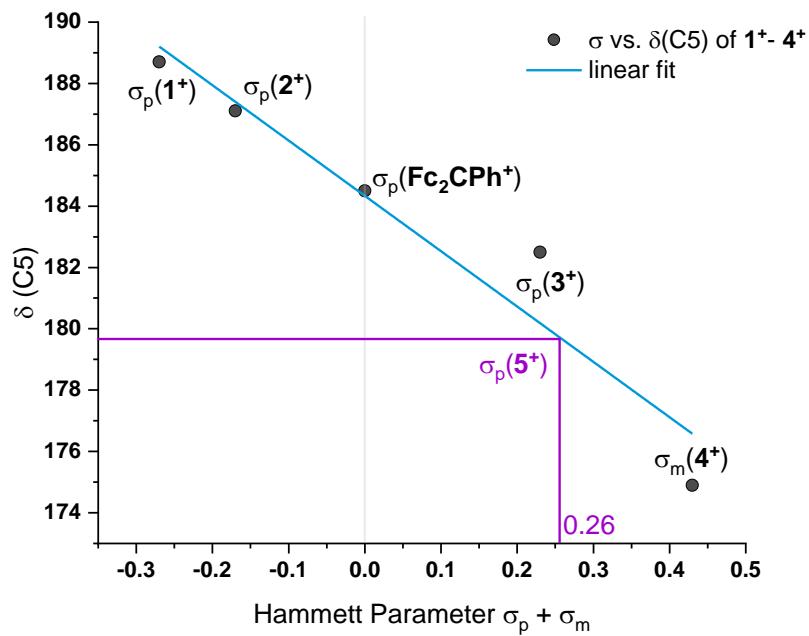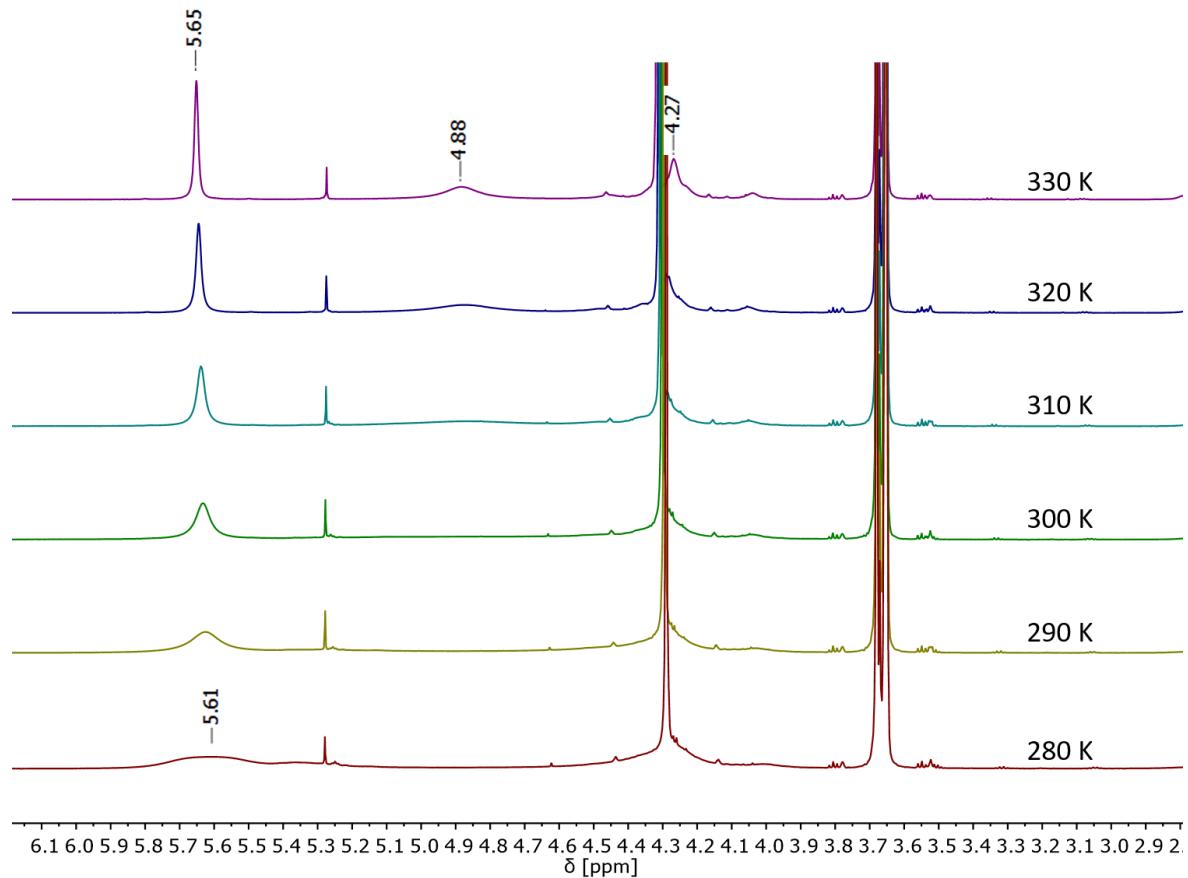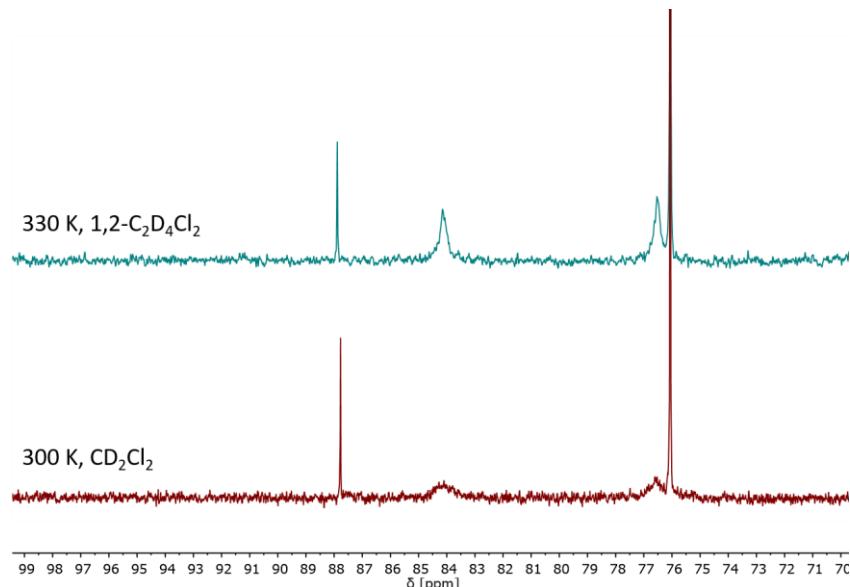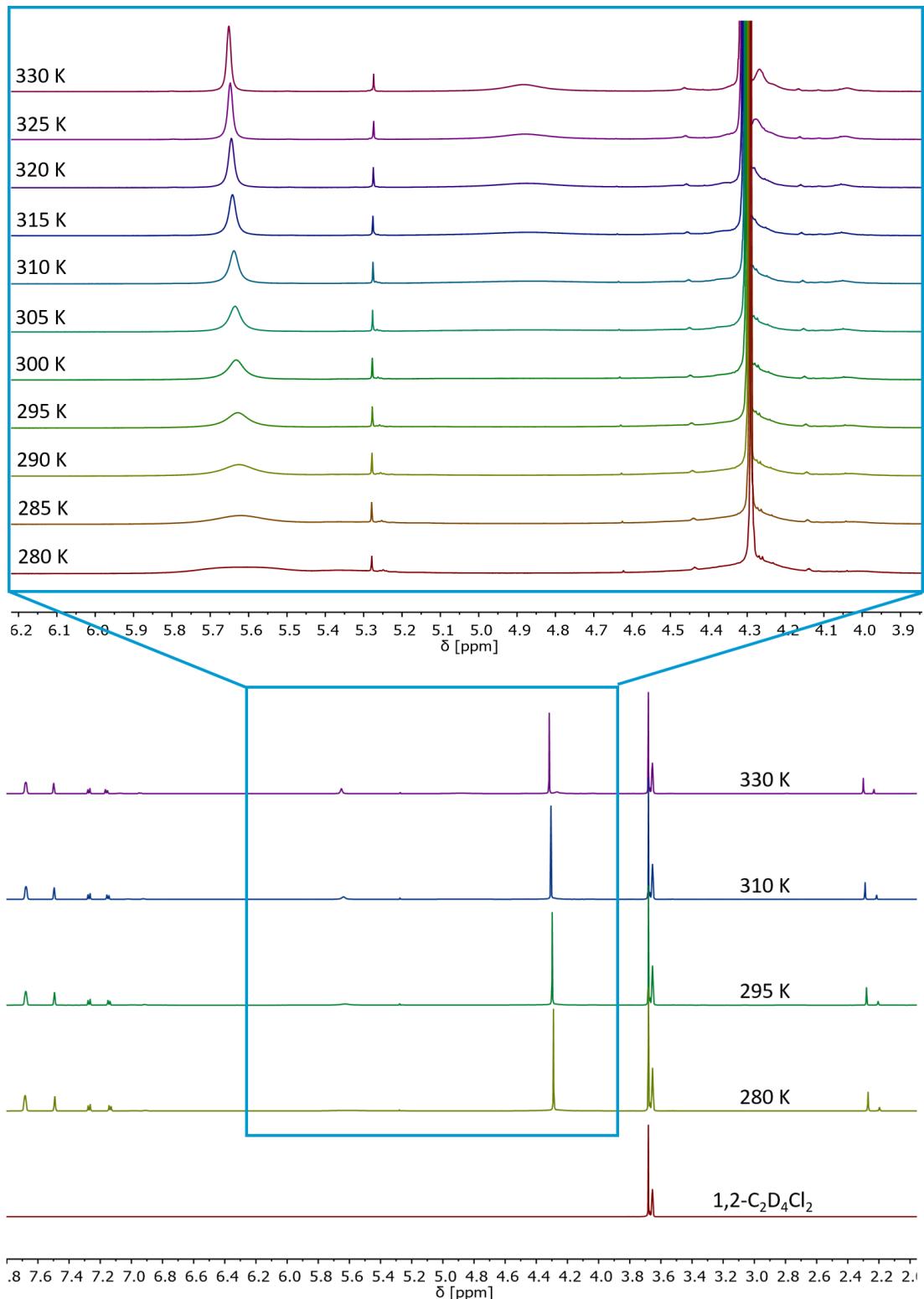
XRD- Crystal Data

Table S1: Comparison of the crystal data of carbinols **1-OH** to **5-OH**.

	1-OH	2-OH	3-OH	4-OH	5-OH
Crystal System, Space Group	triclinic, $P\bar{1}$	triclinic, $P\bar{1}$	monoclinic, $P2_1/c$	orthorhombic, $Fdd2$	orthorhombic, $Fdd2$
Angle (CpFe1-CpFe1)	3.34°	2.41°	3.91°	4.00	4.59°
Angle (CpFe2-CpFe2)	4.47°	4.56°	3.52°	2.35	2.22°
Angle (CpFe1Cp-CpFe2Cp)	111.05(13)°	109.99(13)°	109.76(2)°	109.40(2)°	109.35(2)°
Angle (CpFe1Cp-Ph)	108.20(14)°	109.03(13)°	109.85(18)°	108.87(2)°	109.80(2)°
Angle (CpFe2Cp-Ph)	110.17(14)°	109.48(13)°	109.33(2)°	110.87(2)°	110.04(2)°
d(C-OH)[a]	1.442(2)	1.437(2)	1.436(3)	1.433(3)	1.436(4)
d(C-Ph)[a]	1.538(3)	1.541(2)	1.532(3)	1.522(4)	1.532(4)
d(C-CpFe1)[a]	1.517(2)	1.517(2)	1.512(3)	1.520(4)	1.514(4)
d(C-CpFe2)[a]	1.512(2)	1.517(2)	1.520(4)	1.509(4)	1.524(4)
d_{top}Cp-Fe1[a]	1.646	1.648	1.650	1.658	1.649
d_{bottom}Cp-Fe1[a]	1.649	1.649	1.655	1.659	1.653
d_{top}Cp-Fe2[a]	1.647	1.650	1.650	1.648	1.646
d_{bottom}Cp-Fe2[a]	1.653	1.655	1.651	1.657	1.652
Fe1	-10.09°, -9.71°, -9.71°, -9.92°, -9.00°	-5.79°, -5.87°, -5.99°, -6.23°, -5.72°	-5.49°, -5.35°, -5.37°, -5.44°, -5.07°	-1.15°, -1.12°, -0.85°, -0.87°, -0.11	-10.98, -11.04°, -10.64°, -10.93°, -10.29°
Fe2	-13.28°, -12.73°, -13.42°, -13.18°, -11.61°	-8.59°, -8.82°, -8.86°, -8.90°, -8.24°	-6.04°, -6.12°, -6.14°, -6.11°, -5.67°	-23.73°, -23.73°, -23.73°, -23.72°, -23.25°	-21.79, -21.70, -21.65, -21.96, -20.37°

[a] Distances d in Å.

Crystal data and structure refinement for **1-OH**.
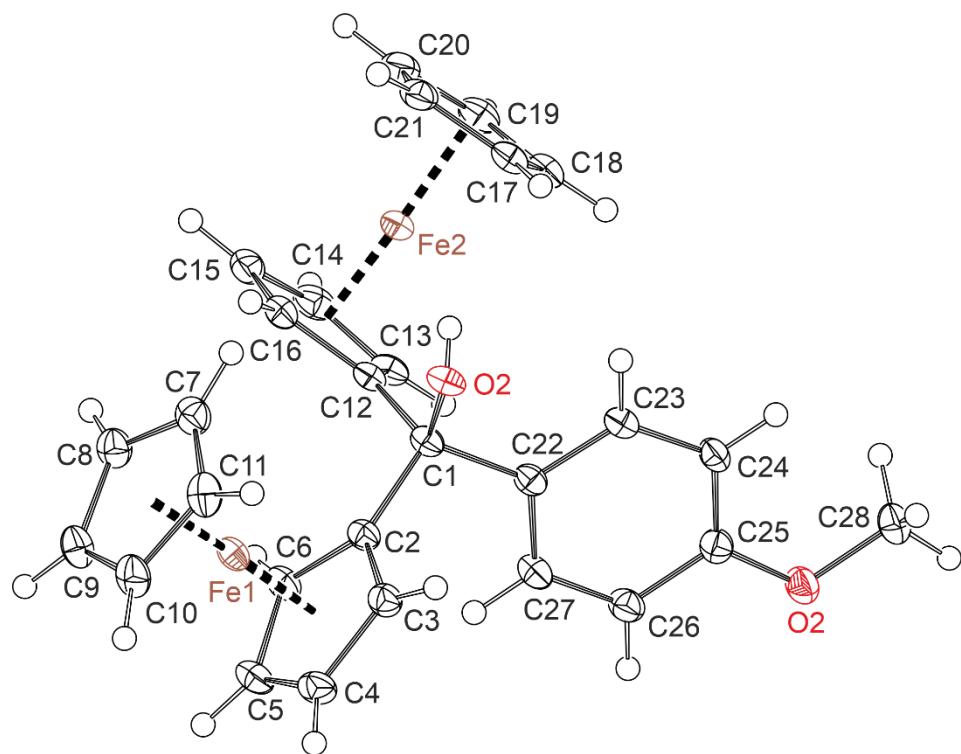
Figure S38: Perspective view of one of the independent molecules in the unit cell of complex **1-OH**. The ellipsoids are displayed at a 50% probability level.

Table S2: Structure solution and refinement data for **1-OH**.

Empirical formula	$C_{28}H_{26}O_2Fe_2$
Formula weight	506.19
Temperature/K	100.15
Crystal system	triclinic
Space group	$P\overline{1}$
a/Å	9.2870(9)
b/Å	10.1320(11)
c/Å	12.9067(16)
α/°	112.121(9)
β/°	96.839(9)
γ/°	101.771(8)
Volume/Å^3	1075.4(2)
Z	2
ρ_{calc}g/cm^3	1.563
μ/mm^{-1}	1.373
F(000)	524.0
Crystal size/mm^3	0.5 × 0.277 × 0.08
Radiation	MoKα (λ = 0.71073)
2Θ range for data collection/°	4.418 to 53.47
Index ranges	-11 ≤ h ≤ 11, -12 ≤ k ≤ 12, -16 ≤ l ≤ 16
Reflections collected	15773
Independent reflections	4548 [R_{int} = 0.0824, R_{sigma} = 0.0497]
Data/restraints/parameters	4548/0/293
Goodness-of-fit on F^2	1.038
Final R indexes [I>=2σ (I)]	R_1 = 0.0317, wR_2 = 0.0782
Final R indexes [all data]	R_1 = 0.0342, wR_2 = 0.0795
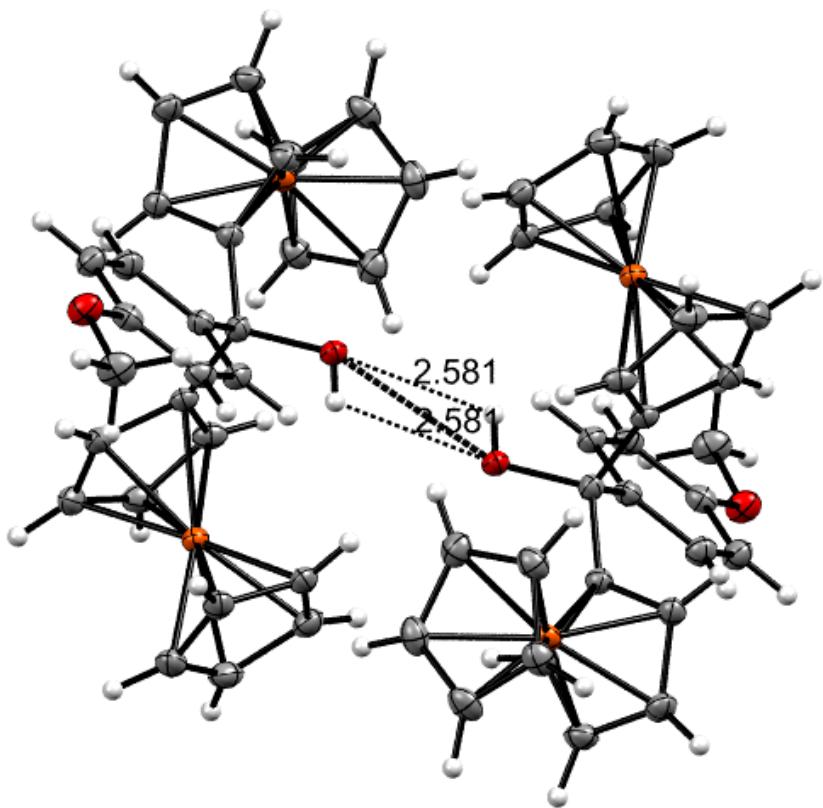
Figure S39: Perspective view of hydrogen bonded dimers of complex **1-OH**. The ellipsoids are displayed at a 50% probability level.

Crystal data and structure refinement for **2-OH**.
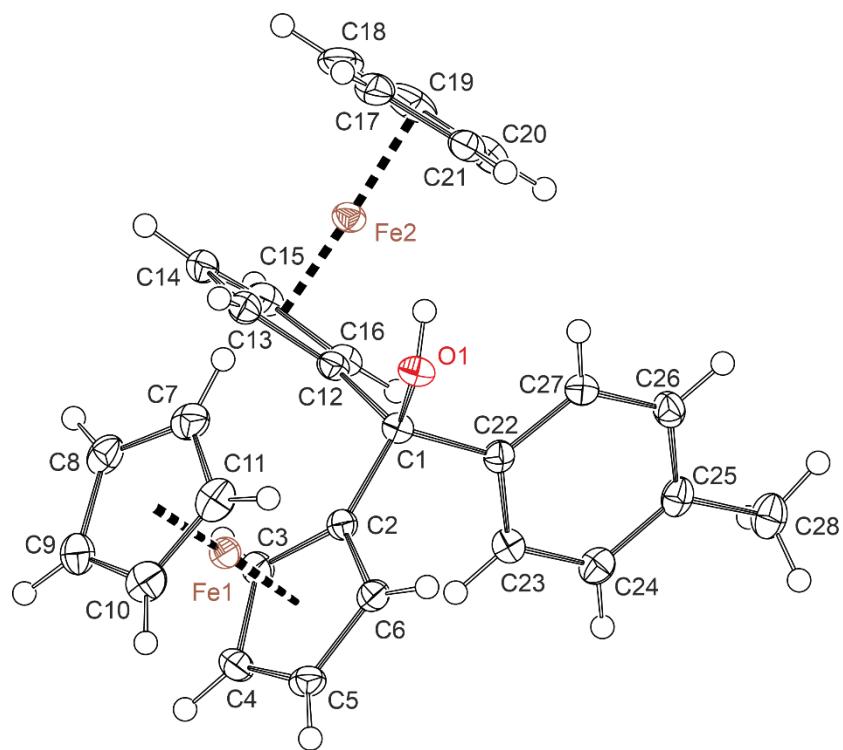
Figure S40: Perspective view of one of the independent molecules in the unit cell of complex **2-OH**. The ellipsoids are displayed at a 50% probability level.

Table S3: Structure solution and refinement data for **2-OH**.

Empirical formula	$C_{28}H_{26}Fe_2O$
Formula weight	490.19
Temperature/K	100(2)
Crystal system	triclinic
Space group	$P\bar{1}$
a/Å	8.992(3)
b/Å	10.149(3)
c/Å	12.791(4)
α/°	77.41(2)
β/°	69.79(2)
γ/°	86.91(2)
Volume/Å^3	1068.8(6)
Z	2
ρ_{calc}g/cm^3	1.523
μ/mm^{-1}	1.376
F(000)	508.0
Crystal size/mm^3	0.3 × 0.2 × 0.1
Radiation	MoKα (λ = 0.71073)
2Θ range for data collection/°	4.786 to 53.698
Index ranges	-11 ≤ h ≤ 11, -12 ≤ k ≤ 12, -16 ≤ l ≤ 16
Reflections collected	12543
Independent reflections	4508 [R_{int} = 0.0184, R_{sigma} = 0.0150]
Data/restraints/parameters	4508/0/282
Goodness-of-fit on F^2	1.029
Final R indexes [I>=2σ (I)]	R_1 = 0.0256, wR_2 = 0.0655
Final R indexes [all data]	R_1 = 0.0291, wR_2 = 0.0678
Largest diff. peak/hole / e Å^{-3}	0.35/-0.44
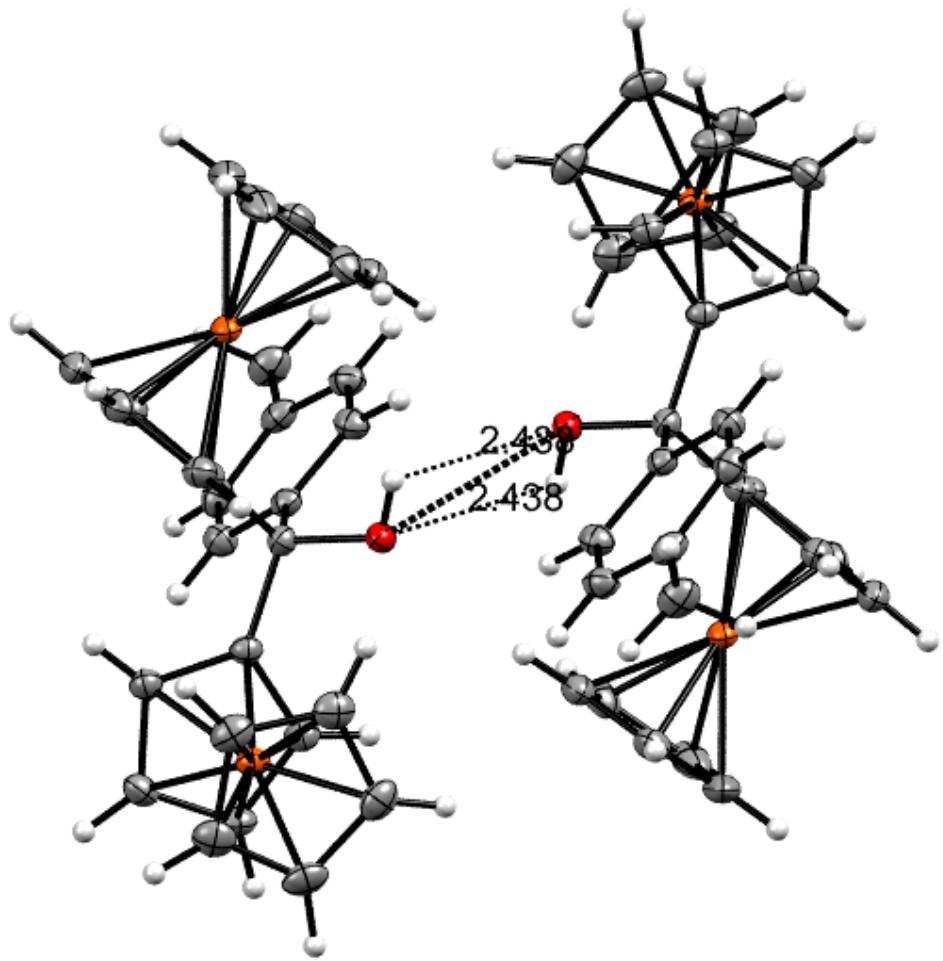
Figure S41: Perspective view of hydrogen bonded dimers of complex **2-OH**. The ellipsoids are displayed at a 50% probability level.

Crystal data and structure refinement for **3-OH**.
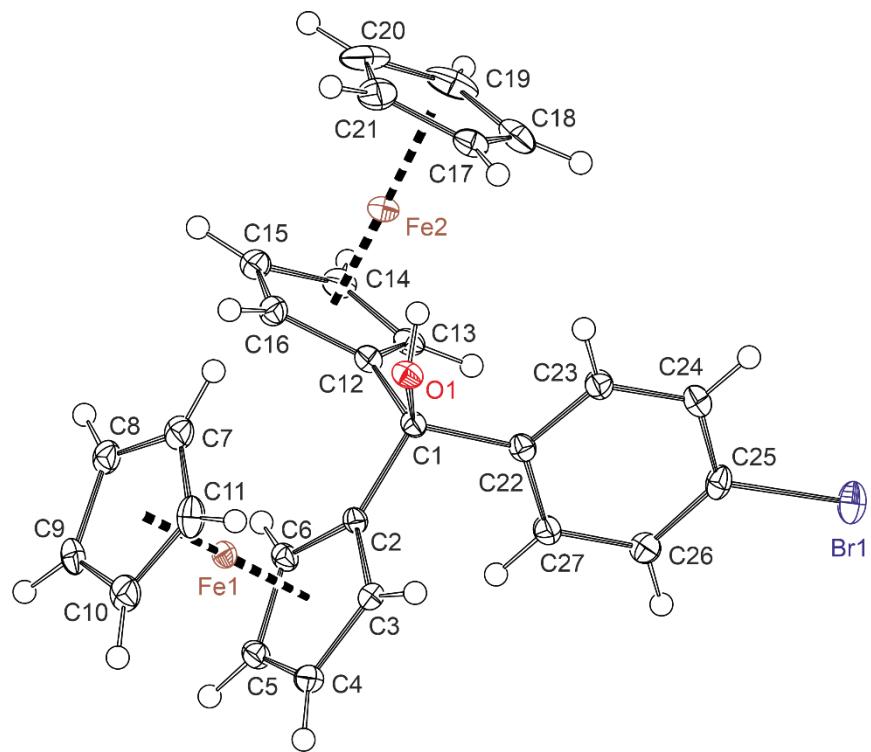
Figure S42: Perspective view of one of the independent molecules in the unit cell of complex **3-OH**. The ellipsoids are displayed at a 50% probability level.

Table S4: Structure solution and refinement data for **3-OH**.

|	
Empirical formula	$C_{27}H_{23}BrFe_2O$
Formula weight	555.06
Temperature/K	100(2)
Crystal system	monoclinic
Space group	$P2_1/c$
a/Å	10.2087(3)
b/Å	22.3002(8)
c/Å	9.2773(2)
α/°	90
β/°	92.140(2)
γ/°	90
Volume/Å^3	2110.56(11)
Z	4
ρ_{calc}g/cm^3	1.747
μ/mm^{-1}	3.286
F(000)	1120.0
Crystal size/mm^3	0.3 × 0.2 × 0.1
Radiation	MoKα (λ = 0.71073)
2Θ range for data collection/°	3.652 to 53.998
Index ranges	-13 ≤ h ≤ 12, -28 ≤ k ≤ 28, -11 ≤ l ≤ 9
Reflections collected	11459
Independent reflections	4585 [R_{int} = 0.0240, R_{sigma} = 0.0210]
Data/restraints/parameters	4585/0/282
Goodness-of-fit on F^2	1.075
Final R indexes [I>=2σ (I)]	R_1 = 0.0315, wR_2 = 0.0775
Final R indexes [all data]	R_1 = 0.0375, wR_2 = 0.0831
Largest diff. peak/hole / e Å^{-3}	0.55/-0.84
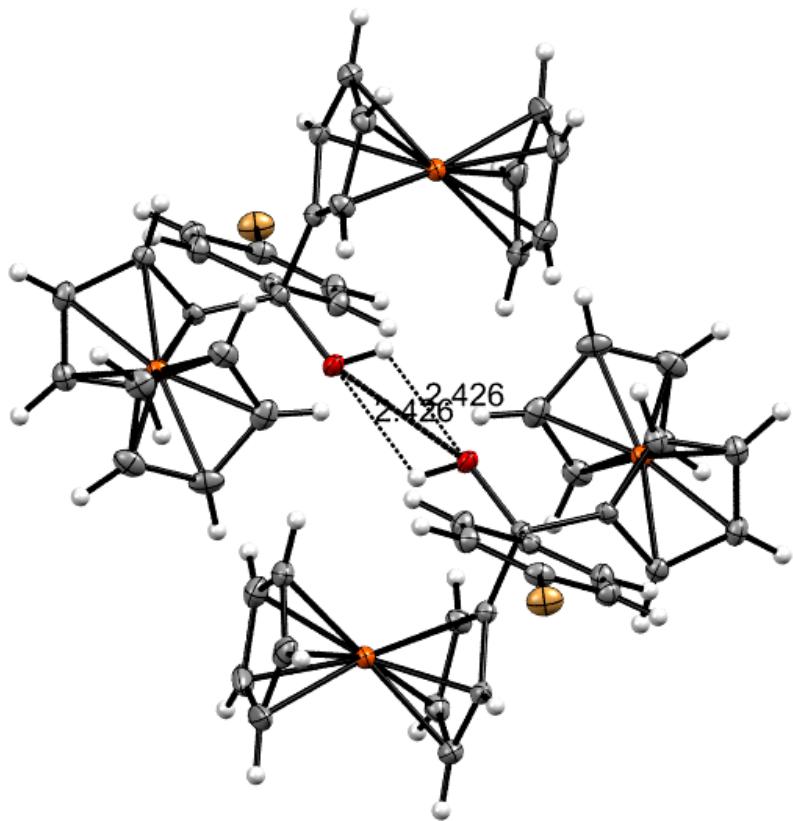
Figure S43: Perspective view of hydrogen bonded dimers of complex **3-OH**. The ellipsoids are displayed at a 50% probability level.

Crystal data and structure refinement for **4-OH**.
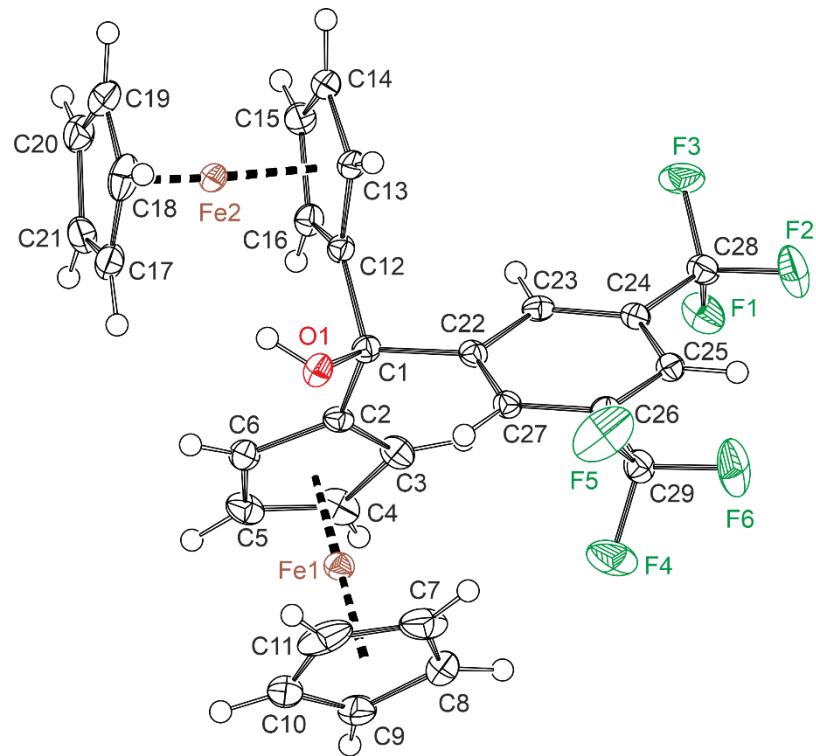
Figure S44: Perspective view of one of the independent molecules in the unit cell of complex **4-OH**. The ellipsoids are displayed at a 50% probability level.
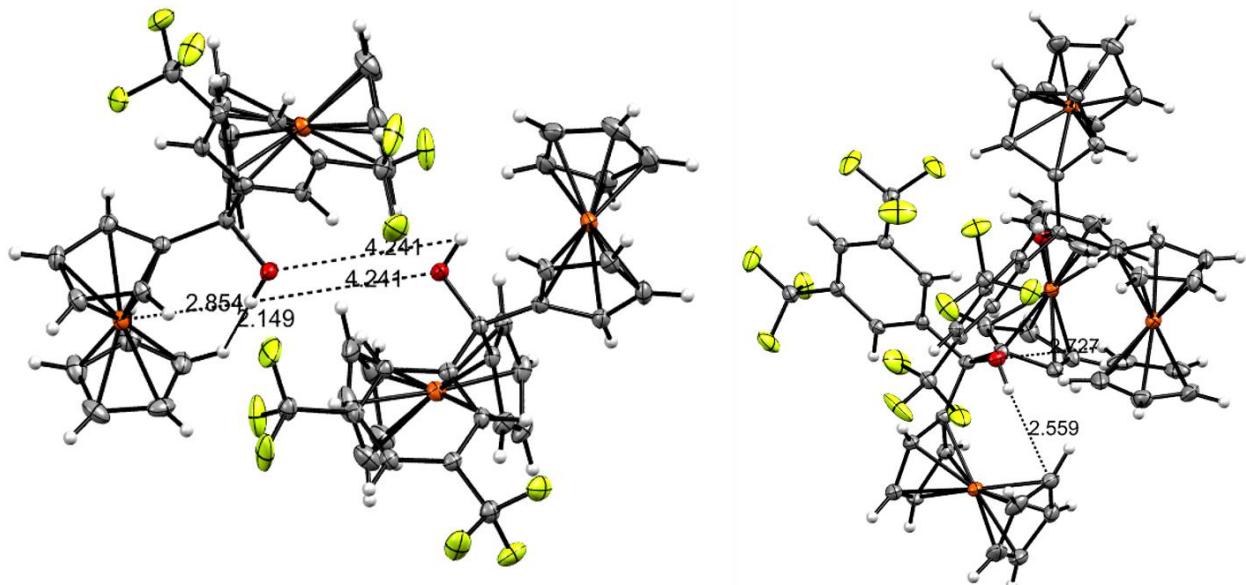
Figure S45: Perspective view of two molecules of complex **4-OH** lacking true hydrogen bonds. The ellipsoids are displayed at a 50% probability level.
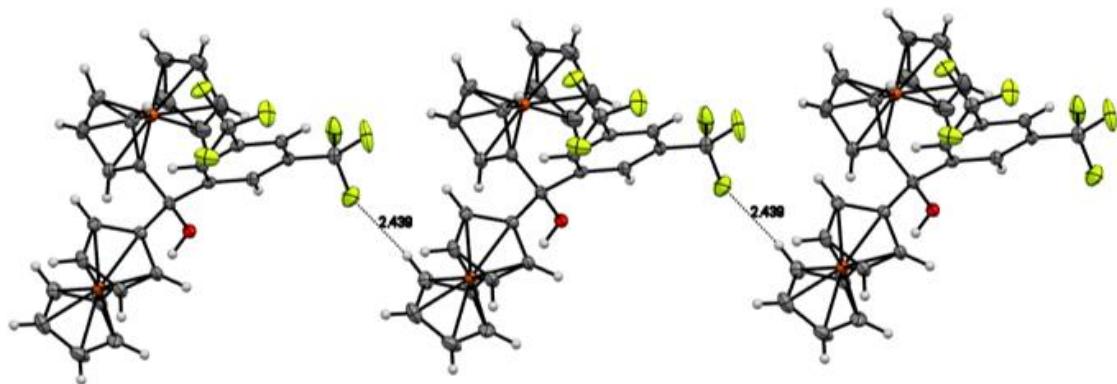
Figure S46: Perspective view of three molecules of complex **4-OH** with single C-H···F contacts of 2.439 Å interconnecting the individual molecules. The ellipsoids are displayed at a 50% probability level.

Table S5: Structure solution and refinement data for **4-OH**.

Empirical formula	$C_{29}H_{22}F_6Fe_2O$
Formula weight	612.16
Temperature/K	100
Crystal system	orthorhombic
Space group	*Fdd*2
a/Å	15.9862(5)
b/Å	40.2342(8)
c/Å	14.6279(3)
α/°	90
β/°	90
γ/°	90
Volume/Å^3	9408.5(4)
Z	16
ρ_{calc}g/cm^3	1.729
μ/mm^{-1}	1.304
F(000)	4960.0
Crystal size/mm^3	0.6 × 0.467 × 0.2
Radiation	MoKα (λ = 0.71073)
2Θ range for data collection/°	4.844 to 55.152
Index ranges	-20 ≤ h ≤ 20, -51 ≤ k ≤ 52, -18 ≤ l ≤ 18
Reflections collected	9610
Independent reflections	5389 [R_{int} = 0.0226, R_{sigma} = 0.0276]
Data/restraints/parameters	5389/1/346
Goodness-of-fit on F^2	1.024
Final R indexes [I>=2σ (I)]	R_1 = 0.0238, wR_2 = 0.0577
Final R indexes [all data]	R_1 = 0.0264, wR_2 = 0.0589
Largest diff. peak/hole / e Å^{-3}	0.27/-0.37
Flack parameter	0.000

Crystal data and structure refinement for **5-OH**.
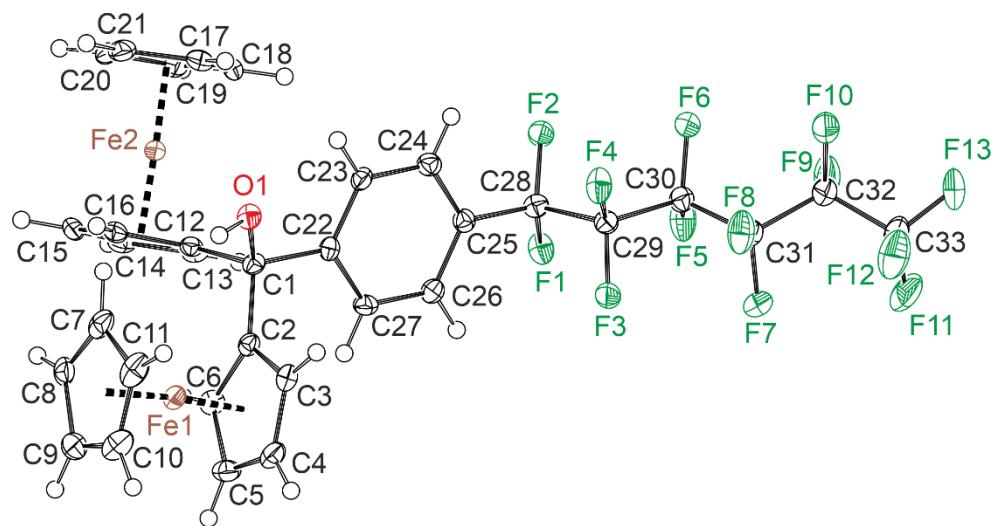
Figure S47: Perspective view of one of the independent molecules in the unit cell of complex **5-OH**. The ellipsoids are displayed at a 50% probability level.
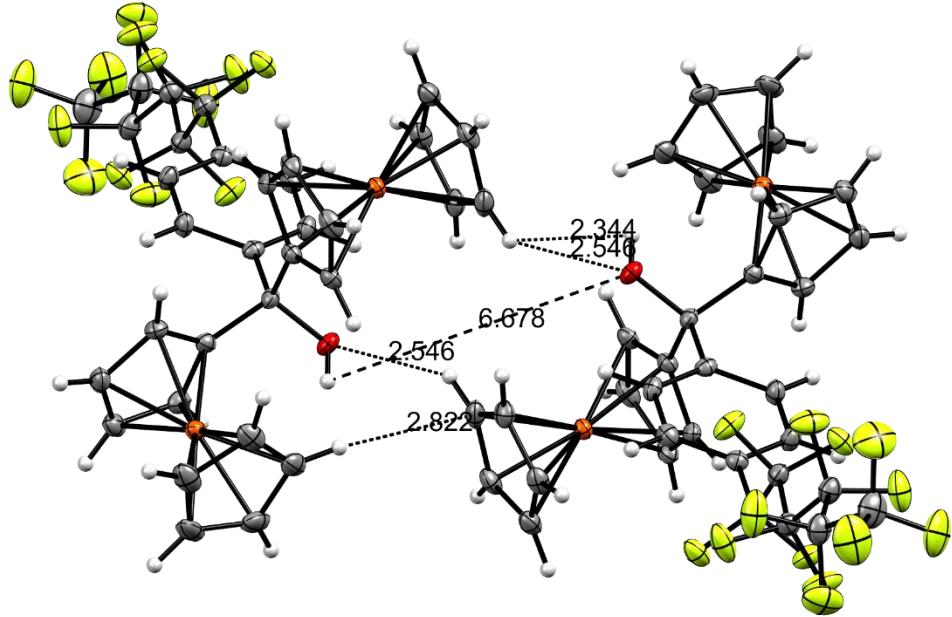
Figure S48: Perspective view of two molecules of complex **5-OH**. The ellipsoids are displayed at a 50% probability level.
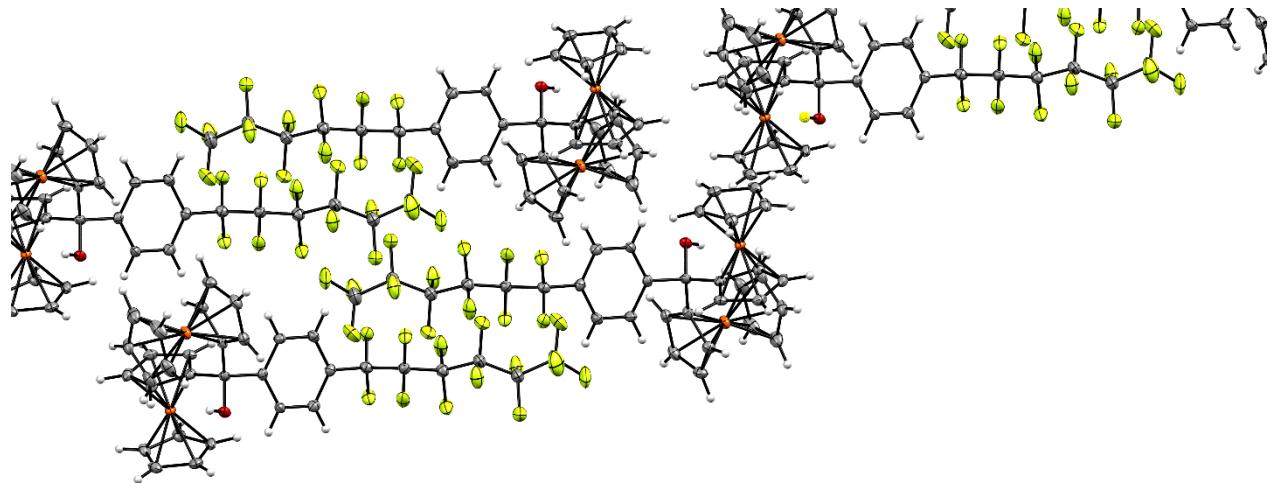

Figure S49: Perspective view of molecule chains in the crystal of **5-OH**. The ellipsoids are displayed at a 50% probability level.

Table S6: Structure solution and refinement data for **5-OH**.

Empirical formula	$C_{29}H_{22}F_6Fe_2O$
Formula weight	612.16
Temperature/K	100
Crystal system	orthorhombic
Space group	*Fdd*2
a/Å	15.9862(5)
b/Å	40.2342(8)
c/Å	14.6279(3)
α/°	90
β/°	90
γ/°	90
Volume/Å^3	9408.5(4)
Z	16
ρ_{calc}g/cm^3	1.729
μ/mm^{-1}	1.304
F(000)	4960.0
Crystal size/mm^3	0.6 × 0.467 × 0.2
Radiation	MoKα (λ = 0.71073)
2Θ range for data collection/°	4.844 to 55.152
Index ranges	-20 ≤ h ≤ 20, -51 ≤ k ≤ 52, -18 ≤ l ≤ 18
Reflections collected	9610
Independent reflections	5389 [R_{int} = 0.0226, R_{sigma} = 0.0276]
Data/restraints/parameters	5389/1/346
Goodness-of-fit on F^2	1.024
Final R indexes [I>=2σ (I)]	R_1 = 0.0238, wR_2 = 0.0577
Final R indexes [all data]	R_1 = 0.0264, wR_2 = 0.0589
Largest diff. peak/hole / e Å^{-3}	0.27/-0.37
Flack parameter	0.000

Table S7: Comparison of the crystal data of the three cationic complexes **1+**, **4+** and **5+**.

	1+	**4+**	**5+**
Crystal System, Space Group	triclinic, $P\overline{1}$	monoclinic, $P2_1/n$	triclinic, $P\overline{1}$
Angle (CpFe1-CpFe1)	5.28°	6.36°	8.51
Angle (CpFe2-CpFe2)	5.49°	6.77°	5.62
Angle (CpFe1Cp-CpFe2Cp)	125.3(3)°	126.5(10)°	123.6(8)°
Angle (CpFe1Cp-Ph)	116.6(3)°	114.7(10)°	117.6(8)°
Angle (CpFe2Cp-Ph)	118.1(3)°	118.8(10)°	118.7(8)°
d(C-Ph)	1.477(5)	1.505(15)	1.488(12)
d(C-CpFe1)	1.435(4)	1.415(15)	1.437(13)
d(C-CpFe2)	1.426(6)	1.422(16)	1.397(13)
Fe1 (HCCH torsion angles of ferrocene) [°]	-1.71, -1.59, -1.95, -1.38, -0.74 **ø-1.474**	-25.57, -20.75, -21.96, -23.28, -23.89 **ø-23.09**	-3.01, -1.73, -0.11, -2.39, -0.97 **ø-1.642**
Fe2 (HCCH torsion angles of ferrocene) [°]	-7.38, -5.18, -6.01, -4.95, -3.74 **ø-5.452**	-5.78, -8.07, -6.96, -6.03, -5.90 **ø-6.548**	-21.73, -18.42 -20.66, -19.04, -16.39 **ø-19.248**
Ph: C_{ipso}-C_{ortho}	1.394(5)/ 1.400(6) **ø1.397(6)**	1.388(15)/ 1.390(16) **ø1.389(16)**	1.371(13)/ 1.393(13) **ø1.382(13)**
Ph: C_{meta}-C_{para}	1.382(7)/ 1.384(6) **ø1.383(7)**	1.335(15)/ 1.367(16) **ø1.351(16)**	1.375(16)/ 1.391(15) **ø1.383(16)**
Ph: C_{ortho}-C_{meta}	1.374(6)/ 1.380(6) **ø1.377(6)**	1.367(16)/ 1.413(16) **ø1.390(16)**	1.398(14)/ 1.410(13) **ø1.404(14)**
Dihedral angle C2-C1-C22-C27	-46.25°	-45.50°	-57.55°
Dihedral angle C12-C1-C22-C23	-47.40°	-46.87°	-60.98°
Rotation out of plane Cp(Fe1) to Phenyl	66.73°	61.39°	66.72°
Rotation out of plane Cp(Fe2) to Phenyl	60.55°	61.94°	65.12°
Rotation out of plane Cp(Fe1) to Cp(Fe2)	18.78°	20.90°	25.83°
d(C1-ipso-C-atoms(Cp))	1.444(5), 1.437(5), 1.443(6), 1.451(6)	1.489(15), 1.455(15), 1.458(16), 1.456(16)	1.504(14), 1.447(13), 1.432(16), 1.482(16)
Angle $C_{Cp,centr.}$-$C_{ipso,Fc}$-C^+ (Fe1/Fe2)	172.13/ 166.39	173.73/ 168.20	167.16/ 168.30
d(Cp_{centr}-Fe1Cp_{centr})	174.19	172.89	173.24
d(Cp_{centr}-Fe2Cp_{centr})	174.31	173.40	173.49

[a] Distances d in Å.

Crystal data and structure refinement for **1⁺**.
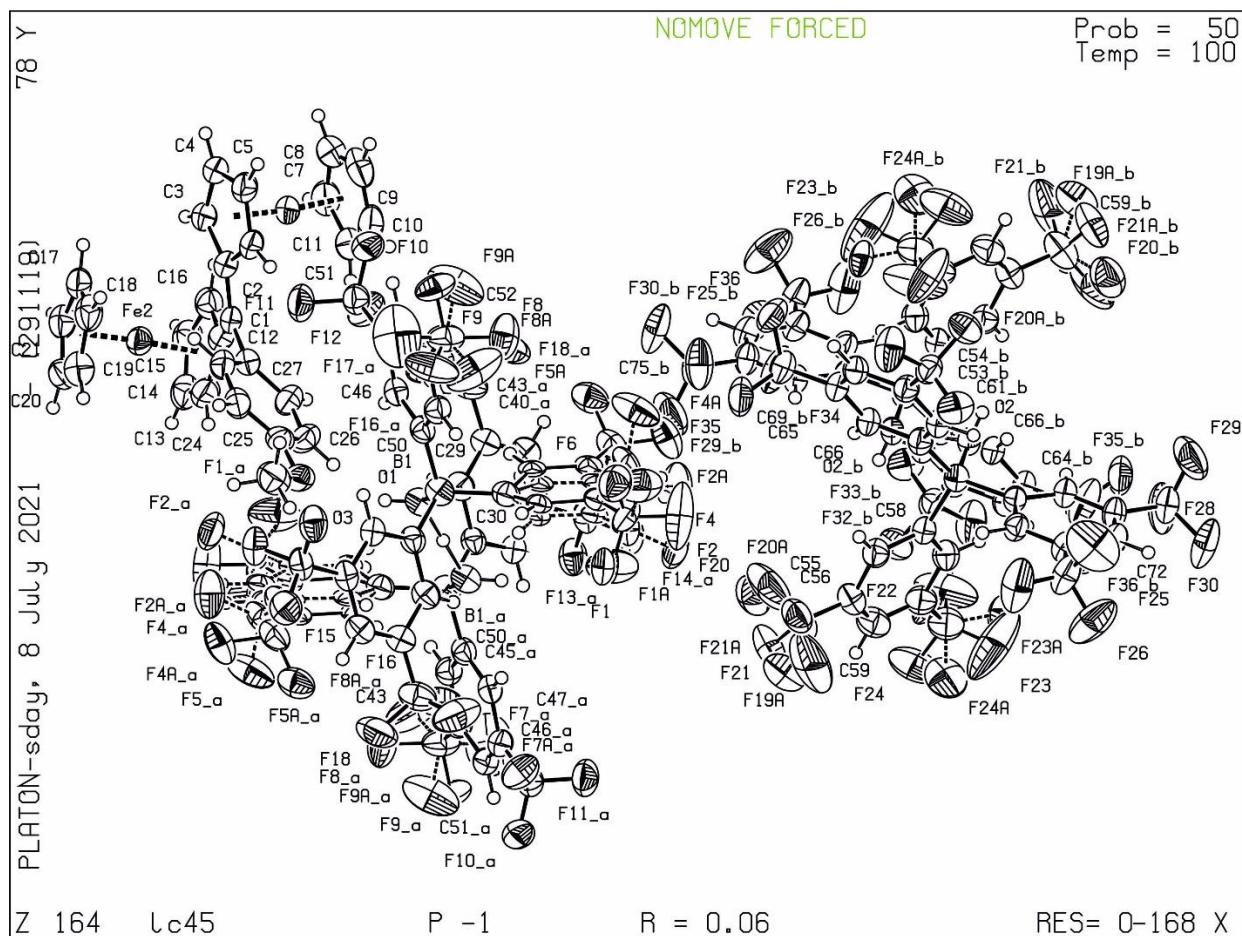
Figure S50: Perspective view of one of the independent molecules (cations and anions) in the unit cell of complex **1⁺**. The ellipsoids are displayed at a 50% probability level.

Table S8: Structure solution and refinement data for **1+**.

Empirical formula	$C_{76}H_{46}B_2F_{36}Fe_2O_3$
Formula weight	1824.45
Temperature/K	100.0
Crystal system	triclinic
Space group	$P\overline{1}$
a/Å	12.8380(4)
b/Å	15.1737(5)
c/Å	23.1393(8)
α/°	95.572(3)
β/°	99.689(3)
γ/°	101.636(3)
Volume/Å^3	4311.7(3)
Z	2
ρ_{calc}g/cm^3	1.405
μ/mm^{-1}	0.457
F(000)	1824.0
Crystal size/mm^3	0.15 × 0.123 × 0.1
Radiation	MoKα (λ = 0.71073)
2Θ range for data collection/°	4.054 to 53.7
Index ranges	-16 ≤ h ≤ 15, -19 ≤ k ≤ 19, -29 ≤ l ≤ 29
Reflections collected	41329
Independent reflections	18527 [R_{int} = 0.0452, R_{sigma} = 0.0619]
Data/restraints/parameters	18527/212/1285
Goodness-of-fit on F^2	1.026
Final R indexes [I>=2σ (I)]	R_1 = 0.0619, wR_2 = 0.1592
Final R indexes [all data]	R_1 = 0.1164, wR_2 = 0.1883
Largest diff. peak/hole / e Å^{-3}	0.61/-0.54
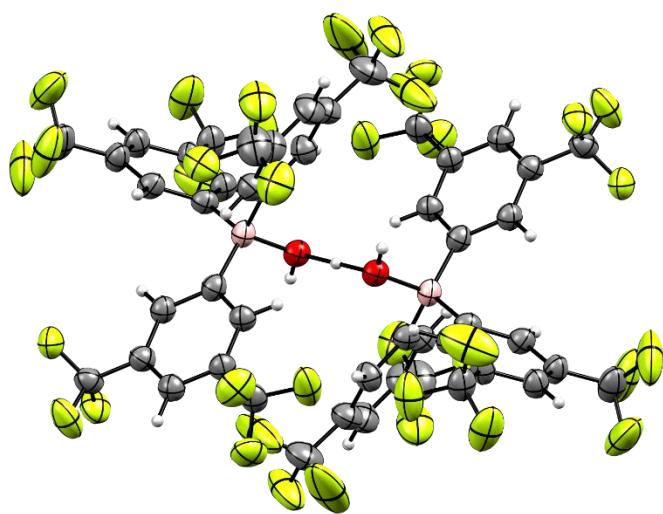
Figure S51: Perspective view of one of the hydrogen-bonded dimeric anions in complex **1⁺**. The ellipsoids are displayed at a 50% probability level.
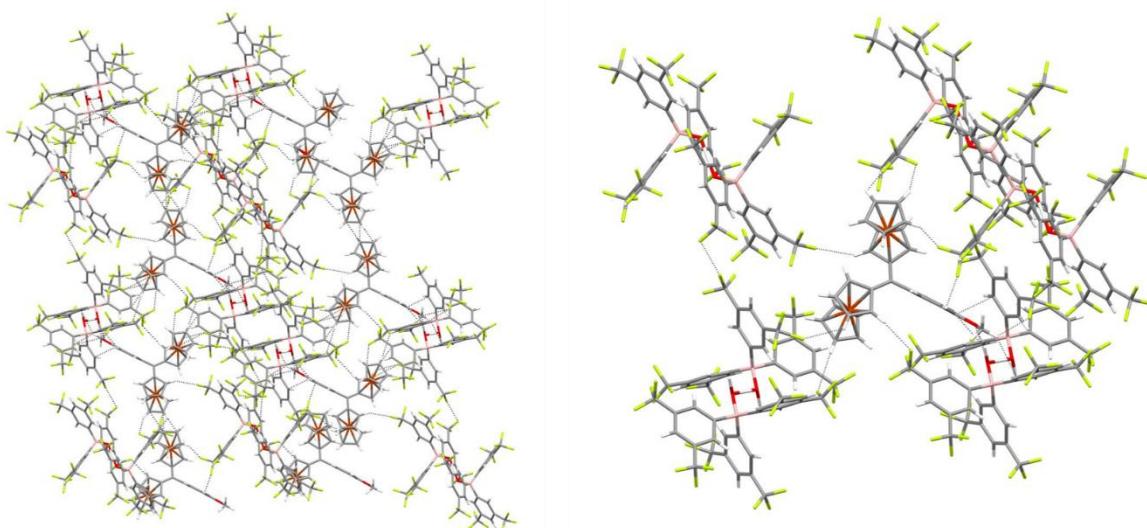
Figure S52: Perspective view of multiple cations and anions from complex **1⁺**.
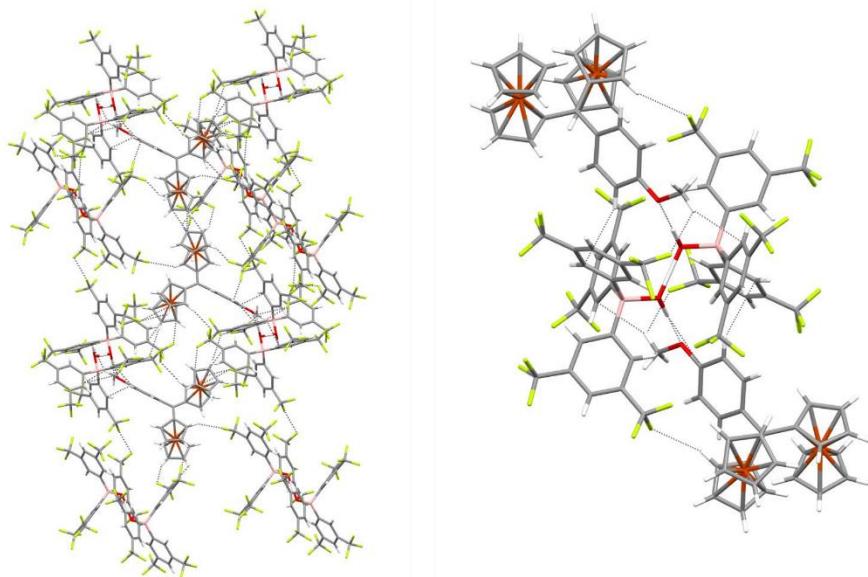
Figure S53: Perspective view of the hydrogen bonding patterns within the molecules in complex **1⁺**.
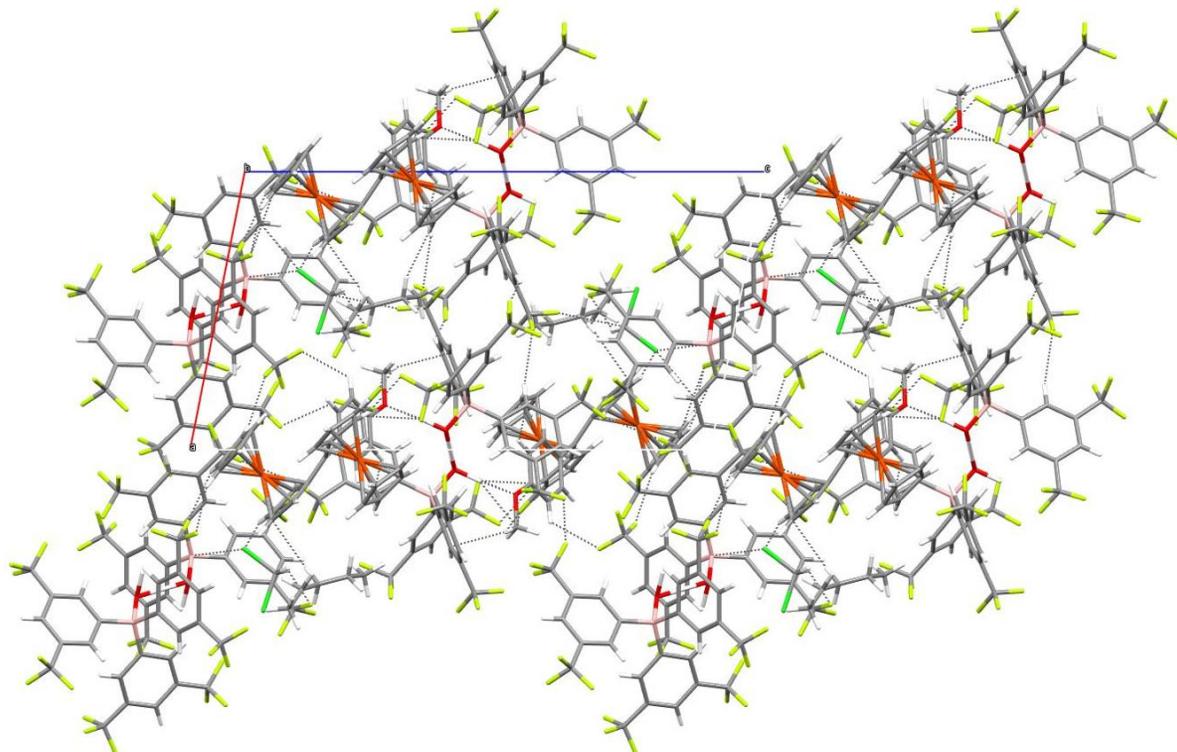
Figure S54: Perspective view along the *a* and *c* axis of the unit cell of complex **1⁺**.

Crystal data and structure refinement for **4⁺**.
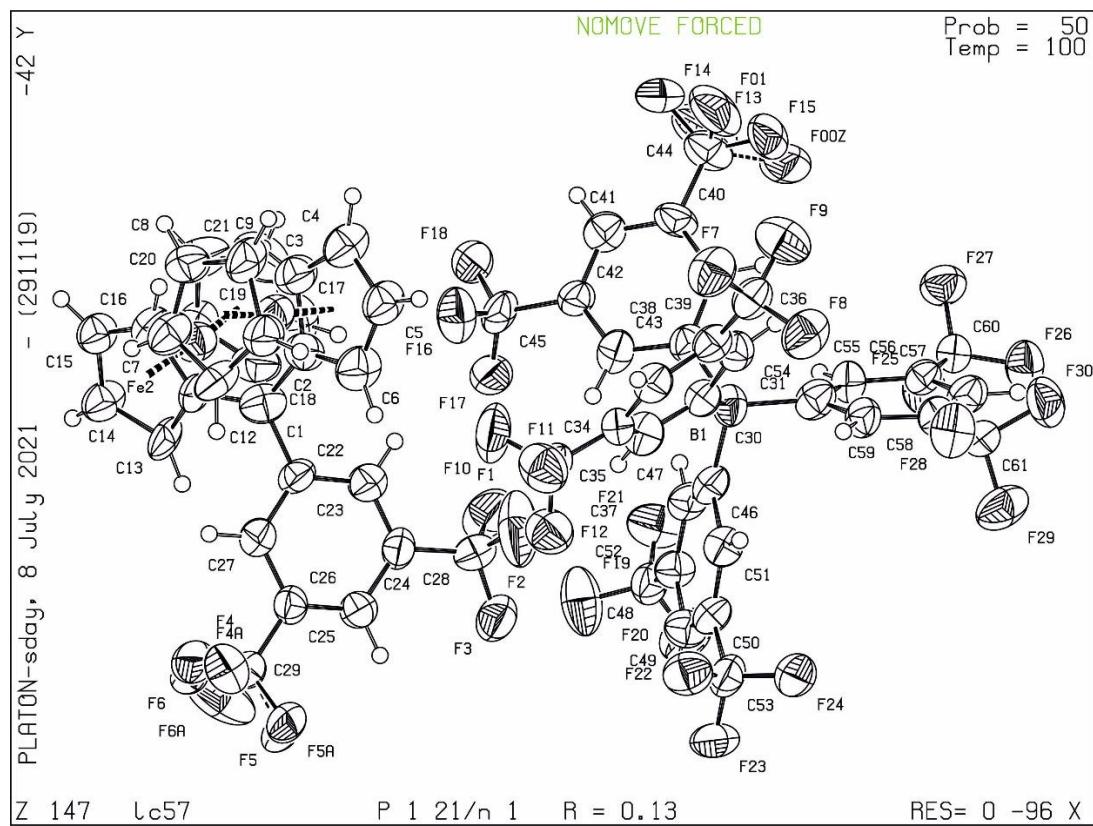
Figure S55: Perspective view of one of the independent molecules (cations and anions) in the unit cell of complex **4⁺**. The ellipsoids are displayed at a 50% probability level.

Table S9: Structure solution and refinement data for **4⁺**.

|	
Empirical formula	$C_{61}H_{33}BF_{30}Fe_2$
Formula weight	1458.38
Temperature/K	100
Crystal system	monoclinic
Space group	$P2_1/n$
a/Å	13.0996(5)
b/Å	20.2030(7)
c/Å	22.6739(9)
α/°	90
β/°	92.688(3)
γ/°	90
Volume/Å³	5994.1(4)
Z	4
$\rho_{calc}g/cm^3$	1.616
μ/mm^{-1}	5.104
F(000)	2904.0
Crystal size/mm³	0.2 × 0.1 × 0.01
Radiation	Cu Kα (λ = 1.54186)
2Θ range for data collection/°	5.862 to 135.268
Index ranges	-15 ≤ h ≤ 15, -23 ≤ k ≤ 22, -25 ≤ l ≤ 25
Reflections collected	32021
Independent reflections	10473 [R_{int} = 0.0804, R_{sigma} = 0.0840]
Data/restraints/parameters	10473/39/895
Goodness-of-fit on F^2	1.475
Final R indexes [I>=2σ (I)]	R_1 = 0.1348, wR_2 = 0.3436
Final R indexes [all data]	R_1 = 0.2048, wR_2 = 0.4318
Largest diff. peak/hole / e Å⁻³	1.72/-0.74
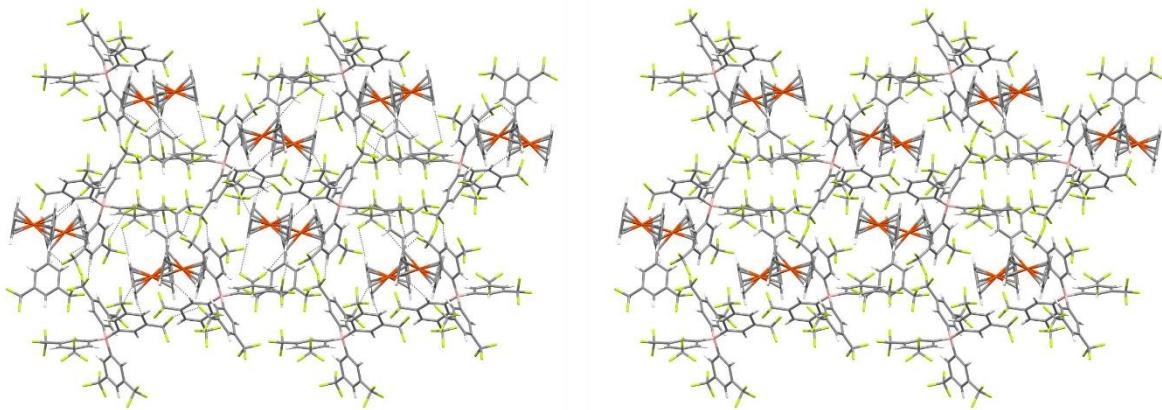
Figure S56: Perspective view on molecule (anion and cation) order within the molecules of complex **4⁺**.
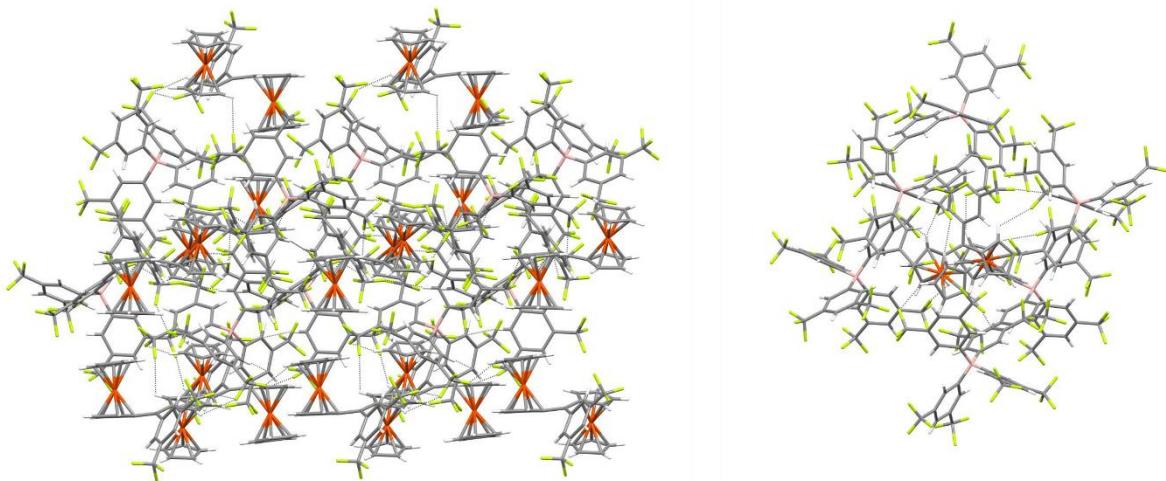
Figure S57: Side-on view on ferrocenes (left) and long distance bonding interaction between the anions and the centrally depicted cation (right) within the molecules of complex **4⁺**.

Crystal data and structure refinement for **5⁺**.
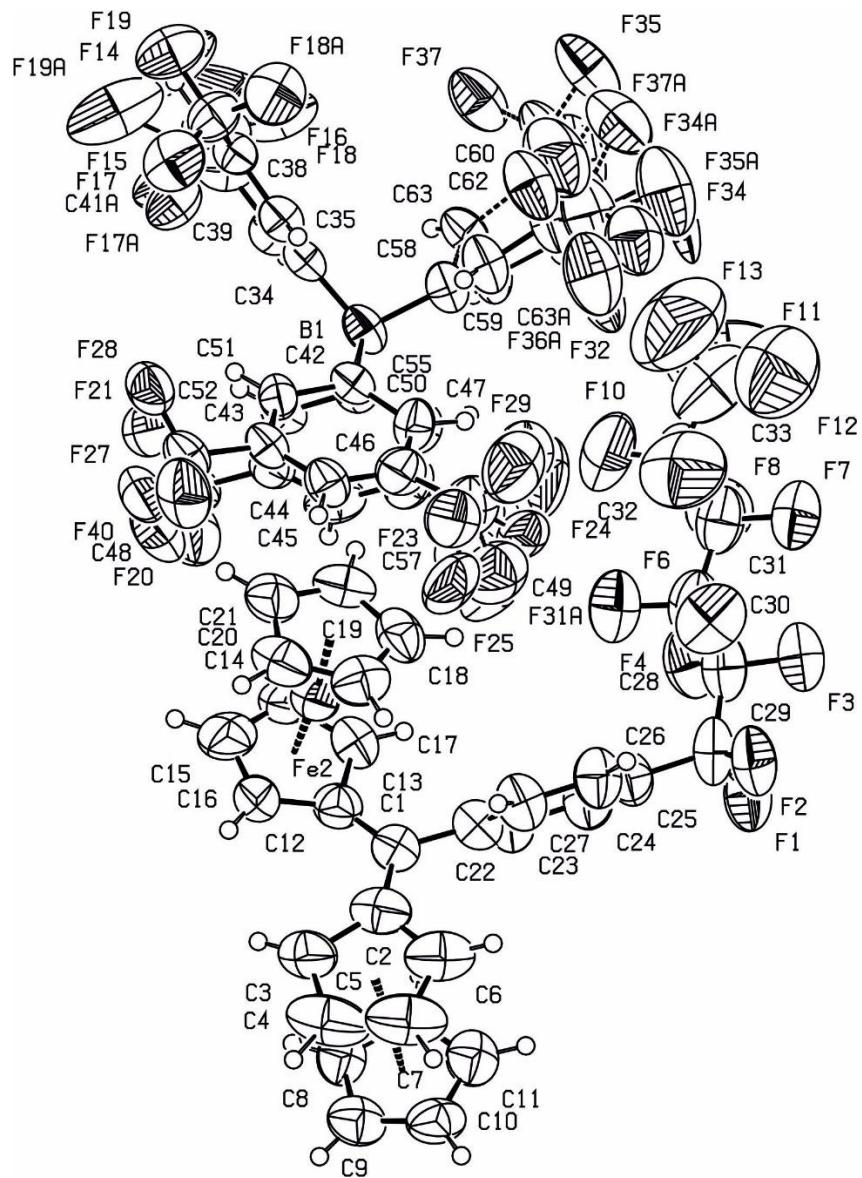
Figure S58: Perspective view of one of the independent molecules (cations and anions) in the unit cell of complex **5⁺**. The ellipsoids are displayed at a 50% probability level.

This crystal unfortunately did not provide data of sufficient precision for in-depth discussion of the bond lengths (see Table S10).

Table S10: Structure solution and refinement data for **5⁺**.

|	
Empirical formula	$C_{130}H_{68}B_2F_{74}Fe_4$
Formula weight	3280.86
Temperature/K	100.0
Crystal system	triclinic
Space group	P-1
a/Å	13.5975(8)
b/Å	14.2300(10)
c/Å	19.8660(15)
α/°	78.080(6)
β/°	85.474(6)
γ/°	66.115(5)
Volume/Å³	3438.9(4)
Z	1
ρ_{calc}g/cm³	1.584
μ/mm⁻¹	0.562
F(000)	1628.0
Crystal size/mm³	0.2 × 0.133 × 0.1
Radiation	MoKα (λ = 0.71073)
2Θ range for data collection/°	4.756 to 55.486
Index ranges	-16 ≤ h ≤ 17, -18 ≤ k ≤ 18, -25 ≤ l ≤ 25
Reflections collected	32324
Independent reflections	15784 [R_{int} = 0.0944, R_{sigma} = 0.1139]
Data/restraints/parameters	15784/331/1113
Goodness-of-fit on F²	1.102
Final R indexes [I>=2σ (I)]	R_1 = 0.1202, wR_2 = 0.3318
Final R indexes [all data]	R_1 = 0.2232, wR_2 = 0.3944
Largest diff. peak/hole / e Å⁻³	1.58/-0.67
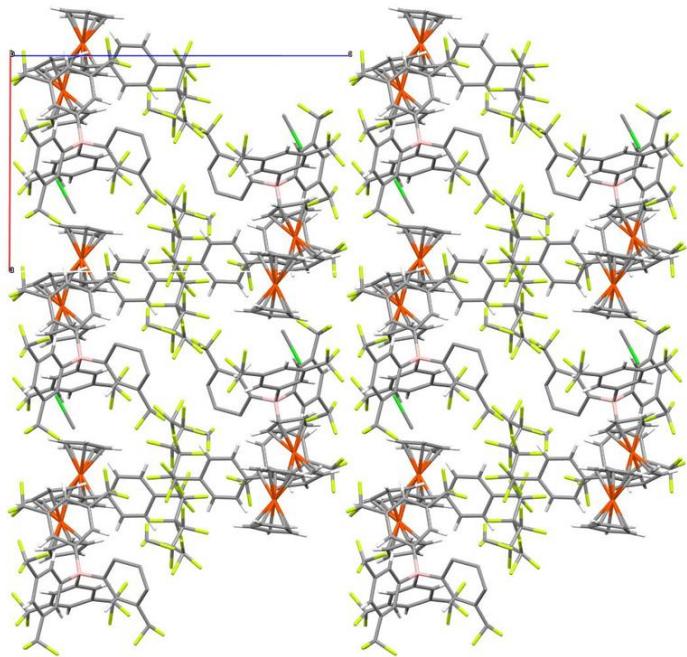
Figure S59: Perspective view on the perfluorinated chain interactions in crystalline **5**⁺ BAR$^F_{24}$⁻.
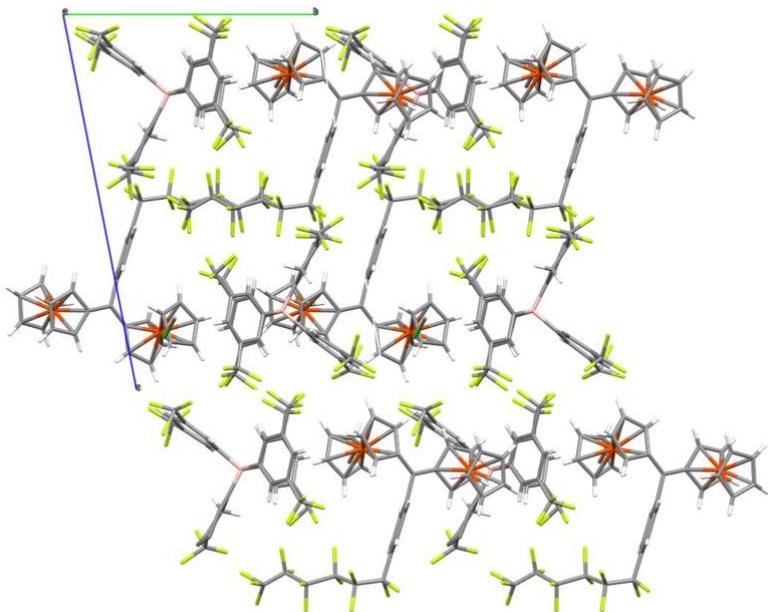
Figure S60: Different-angle perspective view on the perfluorinated chain interactions from complex **5**⁺.
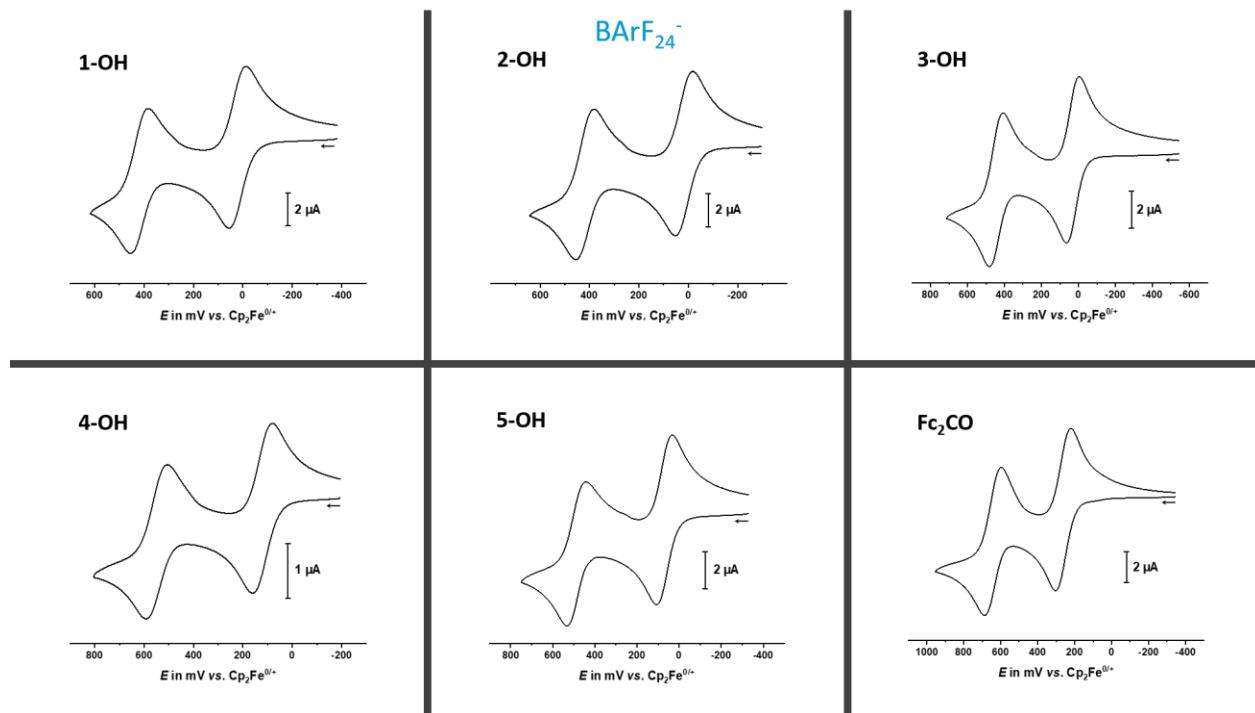
Figure S61: Cyclic voltammograms of the carbinol precursors **1-OH** – **5-OH** at v = 100 mVs^{-1} with y-axis peak current scales in 0.1 M CH$_2$Cl$_2$/ NBu$_4^+$ [BArF$_{24}$]$^-$.
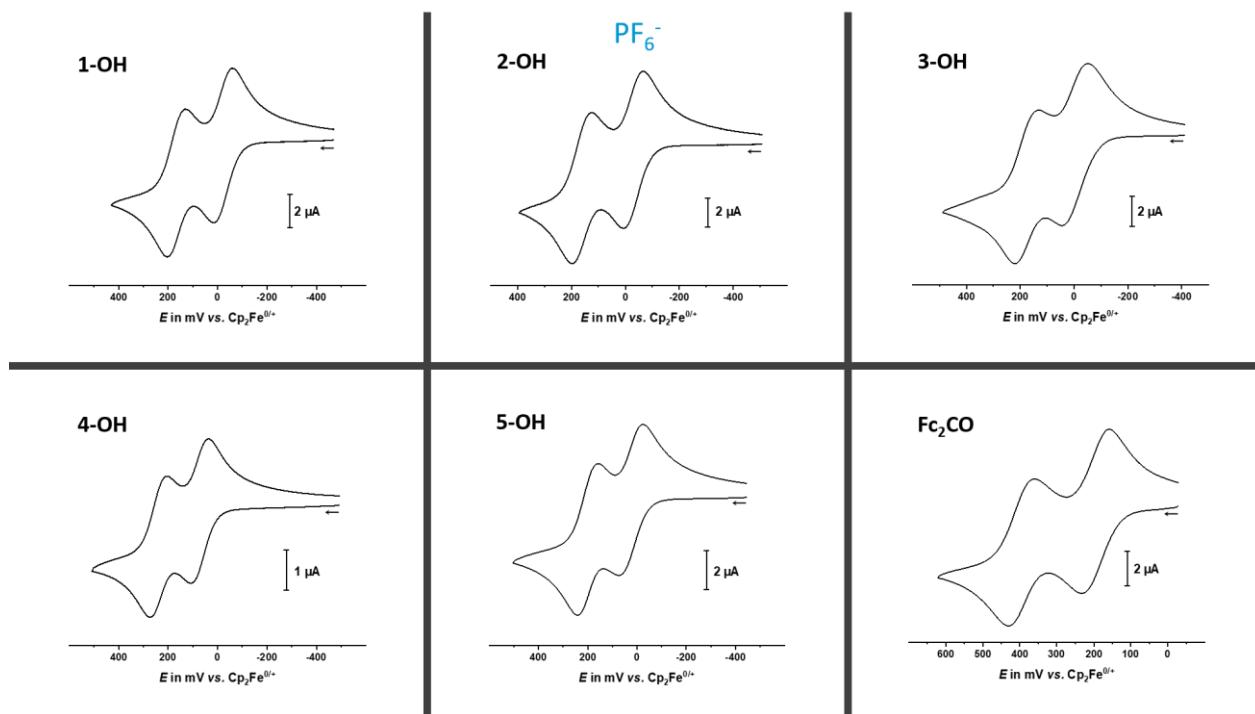
Figure S62: Cyclic voltammograms of the carbinol precursors **1-OH** – **5-OH** at v = 100 mVs^{-1} with y-axis peak current scales in 0.1 M CH$_2$Cl$_2$/ NBu$_4^+$ [PF$_6$]$^-$.
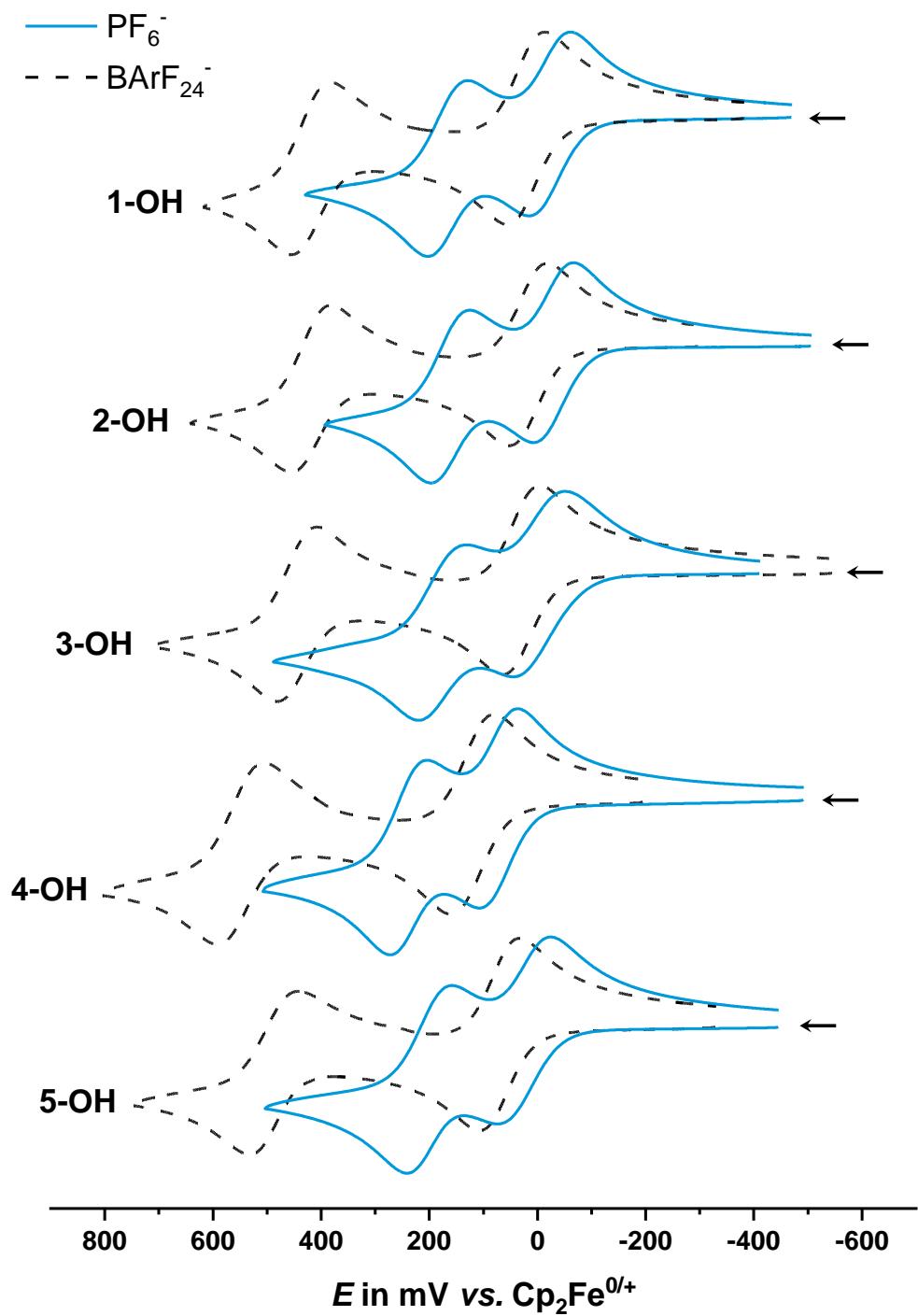
Figure S63: Cyclic voltammograms of the carbinol precursors **1-OH** (top) to **5-OH** (bottom) at v = 100 mVs^{-1} in 0.1 M CH$_2$Cl$_2$/ NBu$_4^+$ [PF$_6$]$^-$ (blue line) and in 0.1 M CH$_2$Cl$_2$/ NBu$_4^+$ [BArF$_{24}$]$^-$ (black dotted line).
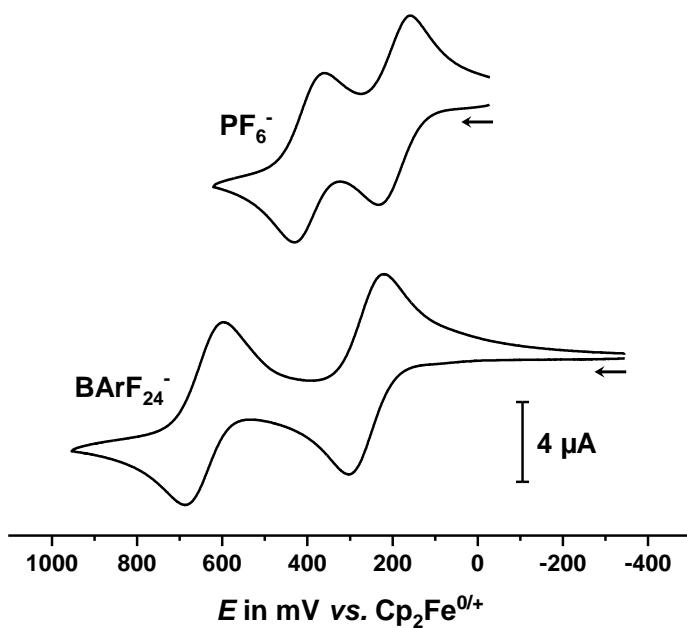
Figure S64: Cyclic voltammograms of the ketone **Fc₂CO** at v = 100 mVs^{-1} in 0.1 M CH₂Cl₂/ NBu₄$^+$ [PF₆]$^-$ (top) and CH₂Cl₂ / NBu₄$^+$ [BArF₂₄]$^-$ (bottom).

Table S11: Additional electrochemical and DFT-computed data for cationic ferrocenylmethylium complexes in CH₂Cl₂ / NBu₄$^+$ [BArF₂₄]$^-$.

X$^+$	$\Delta E_{1/2}$[a]	$\Delta_{HOMO-LUMO}$[b]
1	1575	3.104
2	1550	3.080
3	1510	3.063
4	1435	3.021
5	1530	3.030
FcPh₂C	1460	3.100
Fc₂PhC	1340	3.072
Fc₃C	1090	2.834

[b] Half-wave potential separation in mV. [b] From DFT calculations done in this work with charge 1 and multiplicity 1.
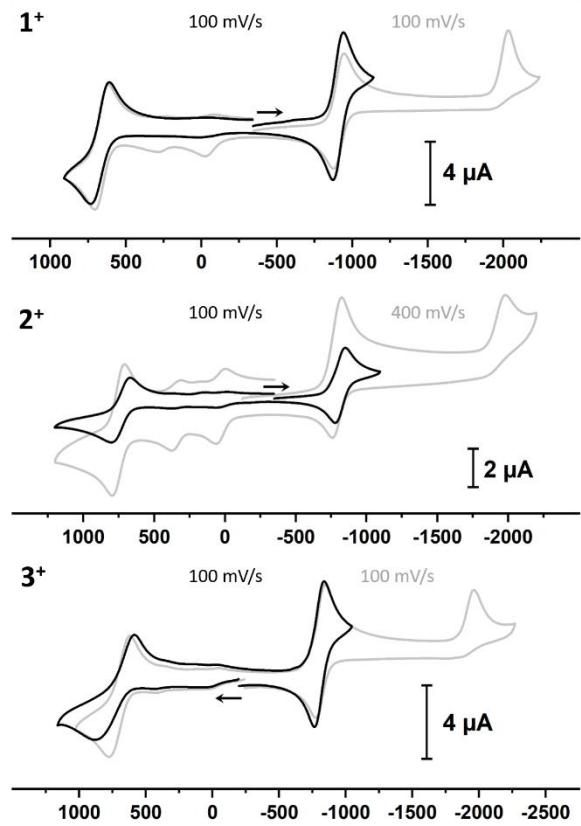
Figure S65: Comparison of cyclic voltammograms recorded after passing through the first (black lines) or the second (grey lines) reductions of cations **1⁺-3⁺**.

E in mV $vs.$ Cp$_2$Fe$^{0/+}$
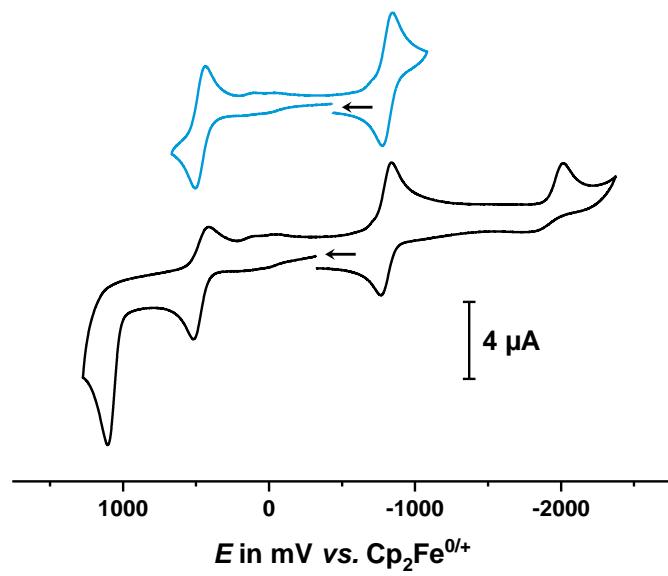
Figure S66: Cyclic voltammograms of **2⁺** at v = 100 mVs^{-1} in 0.1 M CH$_2$Cl$_2$/ NBu$_4^+$ [PF$_6$]$^-$.
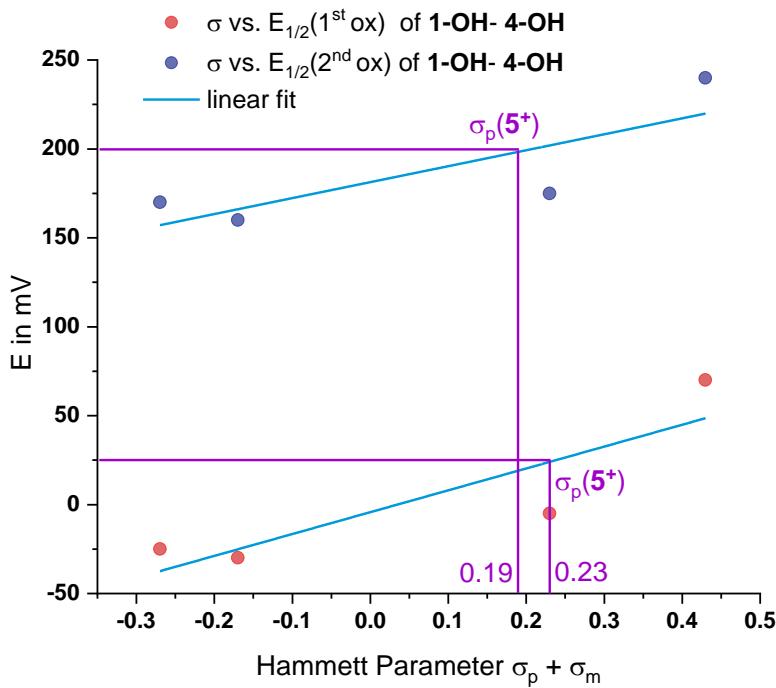
Figure S67: Hammett plot for the oxidation potentials of the first and the second oxidations in NBu_4^+ $[BAr^F_{24}]^-$ of the carbinols **1-OH** $-$ **4-OH**; σ_p (C_6F_{13}) is here approximated by the pink lines to +0.19 and +0.23.
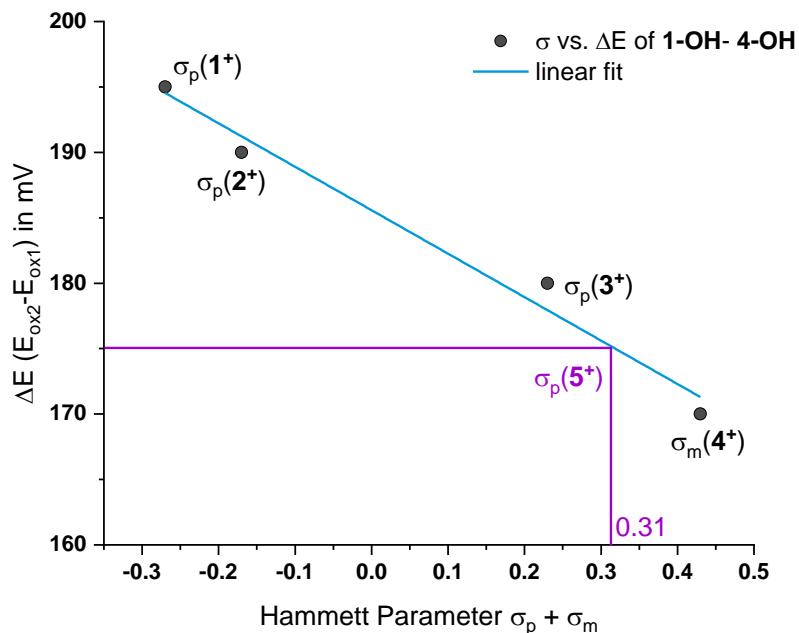
Figure S68: Hammett plot for the redox potential separation between second and the first oxidations of the carbinol complexes **1-OH** $-$ **4-OH** in NBu_4^+ $[BAr^F_{24}]^-$; σ_p (C_6F_{13}) is here approximated by the pink lines to +0.31.
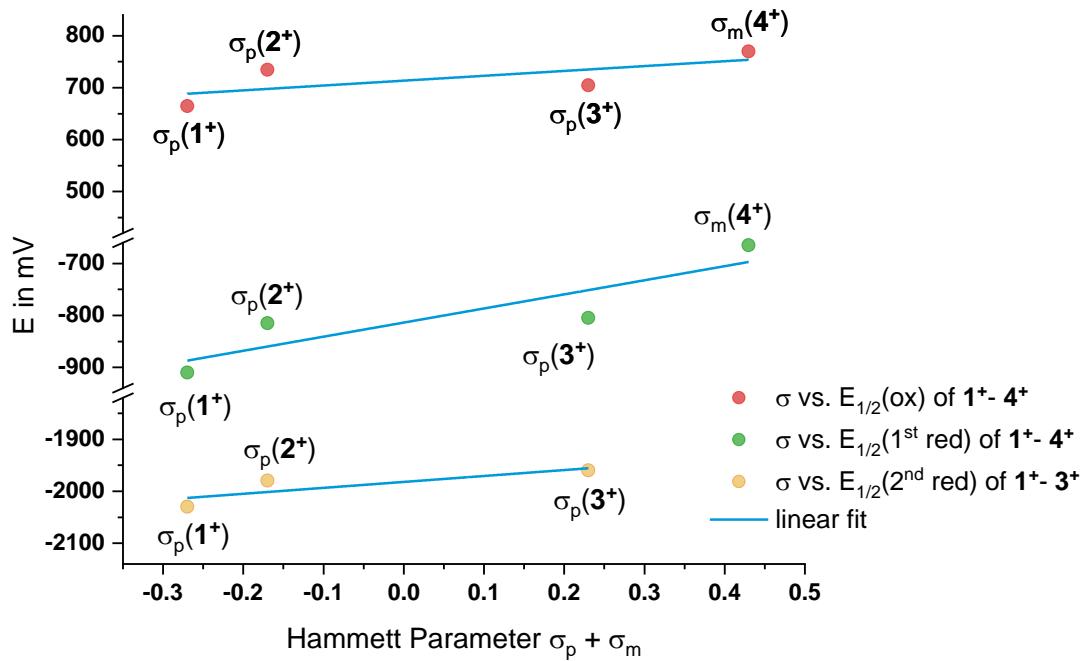
Figure S69: Hammett plot for the oxidation and reduction potentials of the cationic complexes $1^+ - 4^+$ in $NBu_4^+ [BAr^F_{24}]^-$.
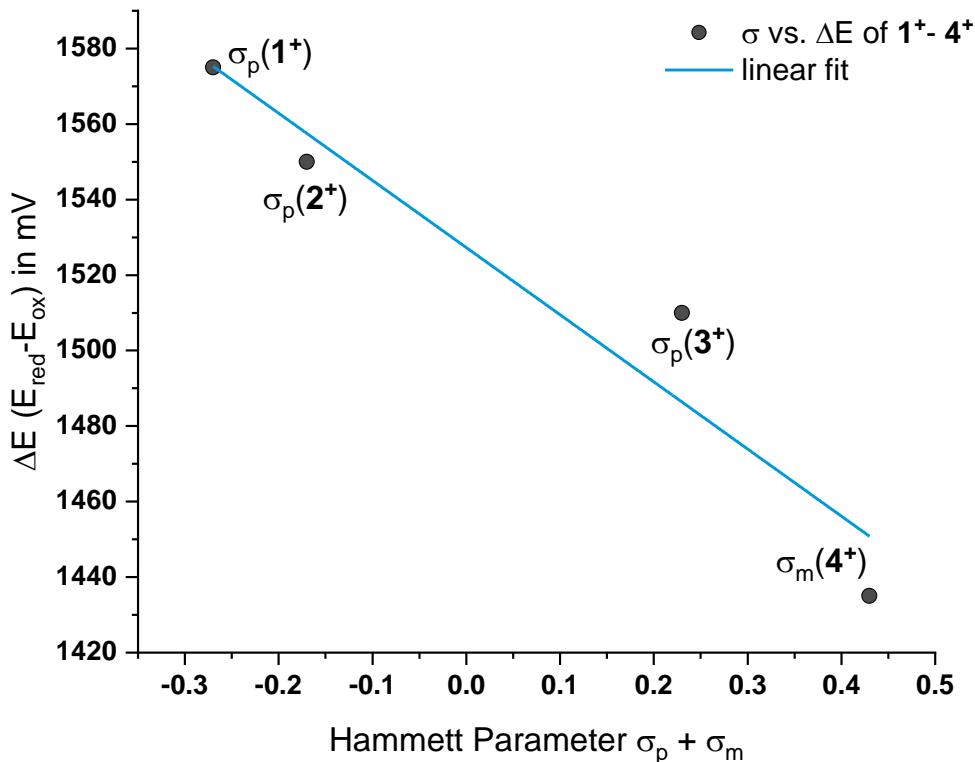
Figure S70: Hammett plot for the redox potential separation between the oxidation and the reduction of the cationic complexes $1^+ - 4^+$ in in $NBu_4^+ [BAr^F_{24}]^-$.

UV/Vis/NIR Spectro(electro)chemical Data and TD-DFT calculations
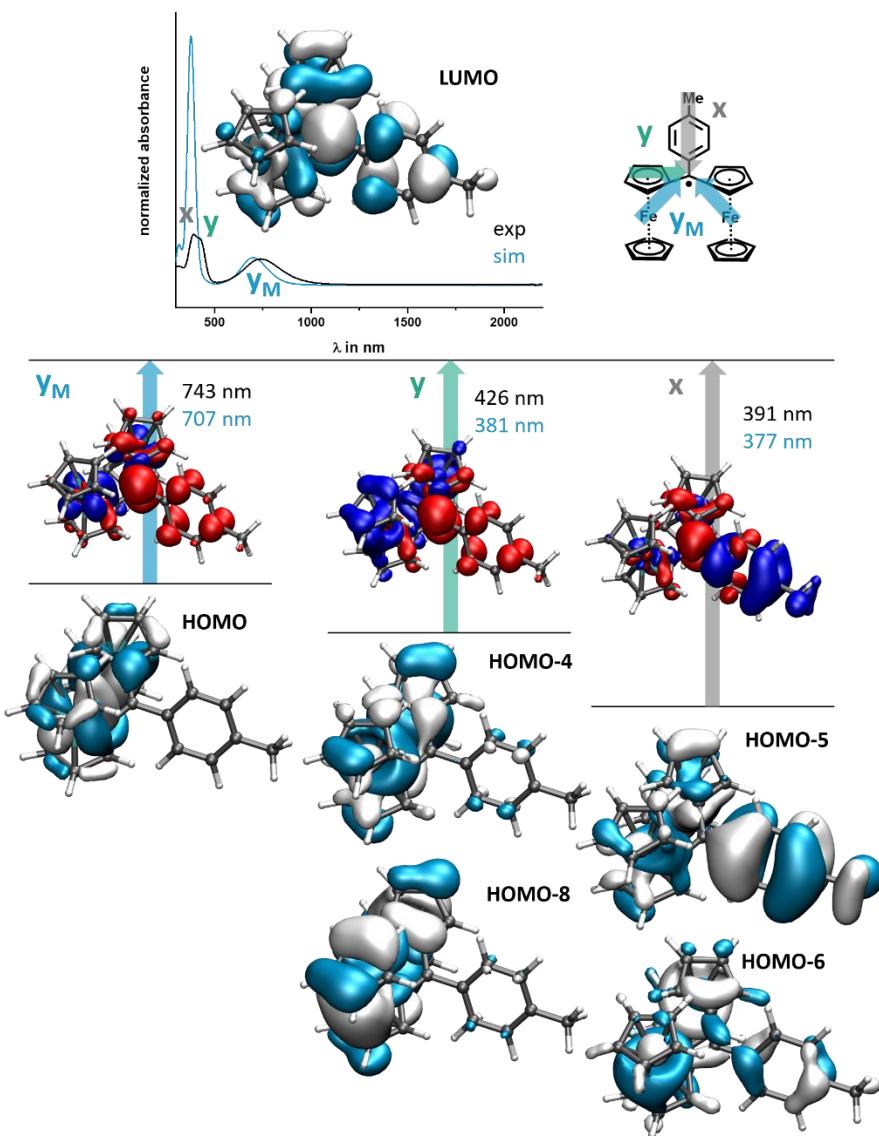
Figure S71: Molecular orbital contributions to major transitions of complex **2⁺** calculated *via* TD-DFT, EDDMs (electron density difference maps; blue: loss of electron density; red: gain in electron density). The top panel compares the experimental (black line) and the TD-DFT-calculated spectrum (blue line). A schematic assignment of the electronic transitions is given at the top right.
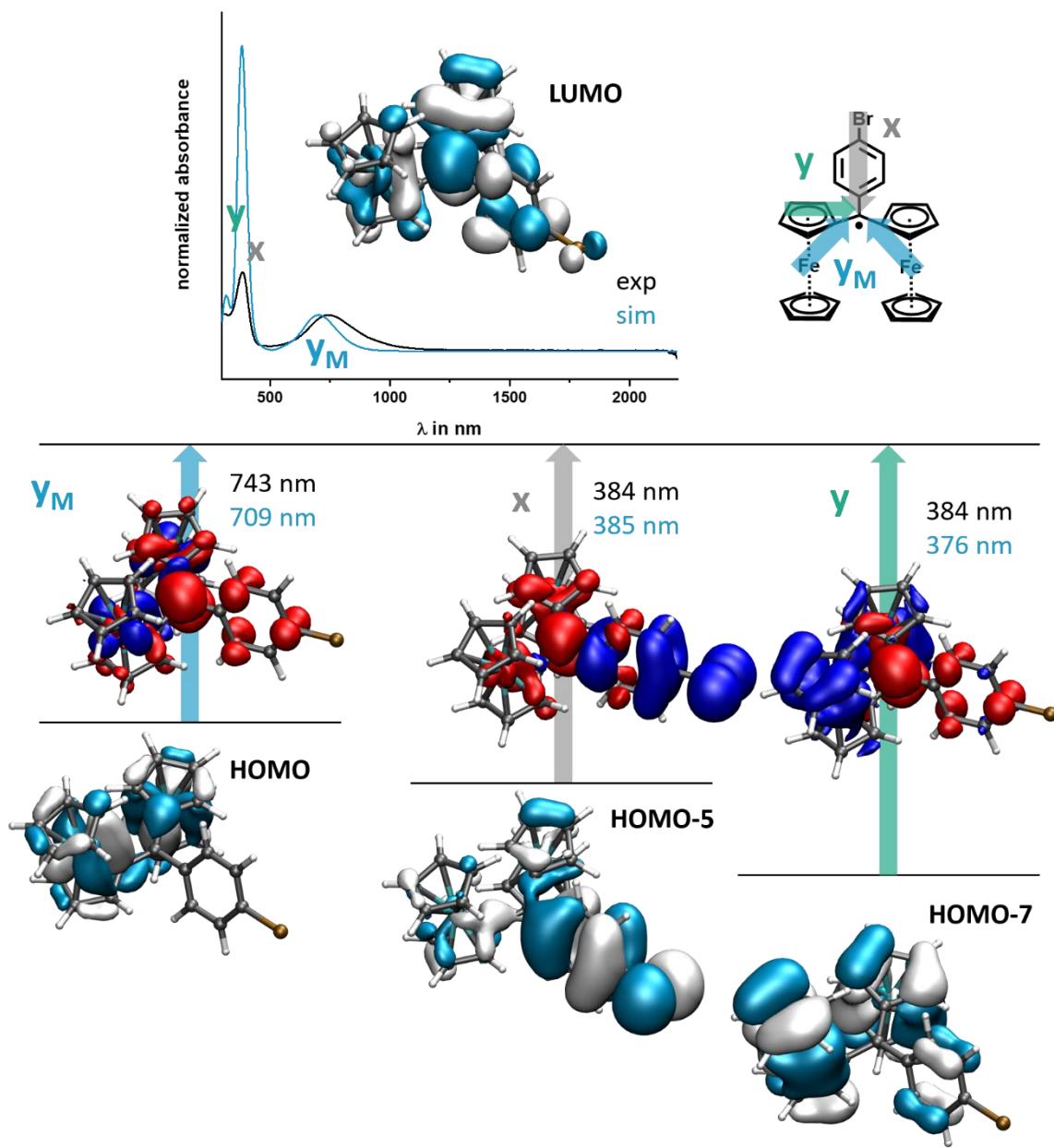
Figure S72: Molecular orbital contributions to major transitions of complex **3⁺** calculated *via* TD-DFT, EDDMs (electron density difference maps; blue: loss of electron density; red: gain in electron density). The top panel compares the experimental (black line) and the TD-DFT calculated spectrum (blue line). A schematic assignment of the electronic transitions is given at the top right.
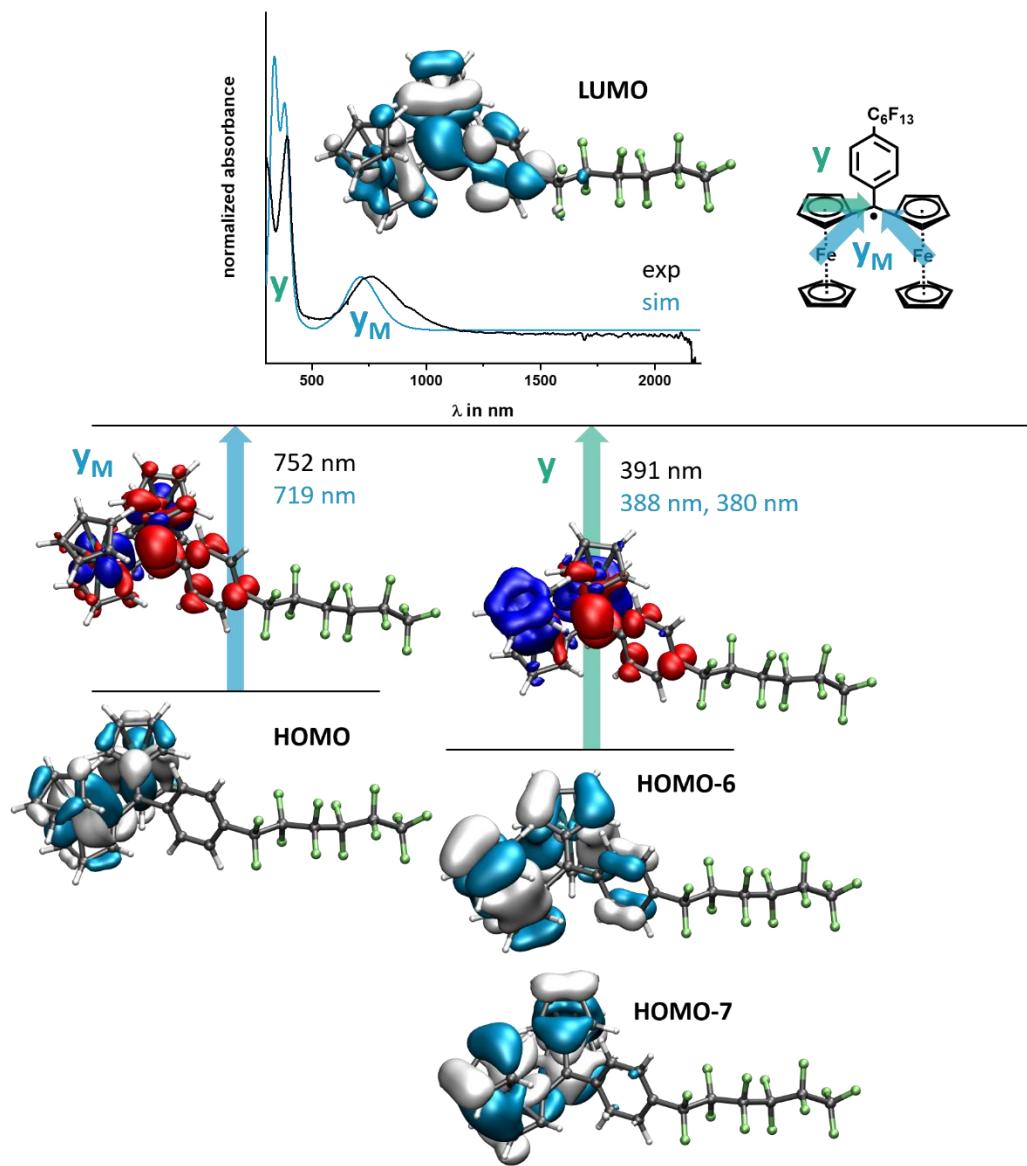
Figure S73: Molecular orbital contributions to major transitions of complex **5$^+$** calculated *via* TD-DFT, EDDMs (electron density difference maps; blue: loss of electron density; red: gain in electron density). The top panel compares the experimental (black line) and the TD-DFT calculated spectrum (blue line). A schematic assignment of the electronic transitions is given at the top right.

Table S12: UV/Vis/NIR data[a] of the complexes in their different redox states.

complex and redox state	λ [nm] (ε [10^3·Lmol^{-1} cm^{-1}])[b]
1$^\bullet$	561 (3.2), 516 (2.0), 348 (10.9)
1$^+$	743 (5.3), 423 (9.7), 393 (10.8)
1^{2+}	727 (1.9), 498 (3.7), 427 (5.1), 383 (6.4)
2$^\bullet$	563 (4.2), 511 (2.7), 391 (3.9), 345 (11.2)
2$^+$	743 (7.0), 426 (12.3), 391 (13.6)
2^{2+}	455 (4.0)
3$^\bullet$	560 (3.3), 524 (2.9), 346 (8.2)
3$^+$	743 (6.0), 384 (13.1)
3^{2+}	-
4$^\bullet$	1114 (0.5), 549 (5.4), 346 (9.8)
4$^+$	761 (6.8), 389 (11.4)
4^{2+}	745 (2.2), 495 (1.8), 377 (6.1)
5$^\bullet$	541 (3.7), 355 (7.9)
5$^+$	752 (2.5), 391 (4.2)
5^{2+}	739 (1.7), 628 (1.2), 384 (5.0)

[a] In 1,2-$C_2H_4Cl_2$/0.25 mM NBu_4^+ [$BArF_{24}$]$^-$ at 293(±3) K. [b] Absorption coefficients ±50 L·mol^{-1} cm^{-1}.
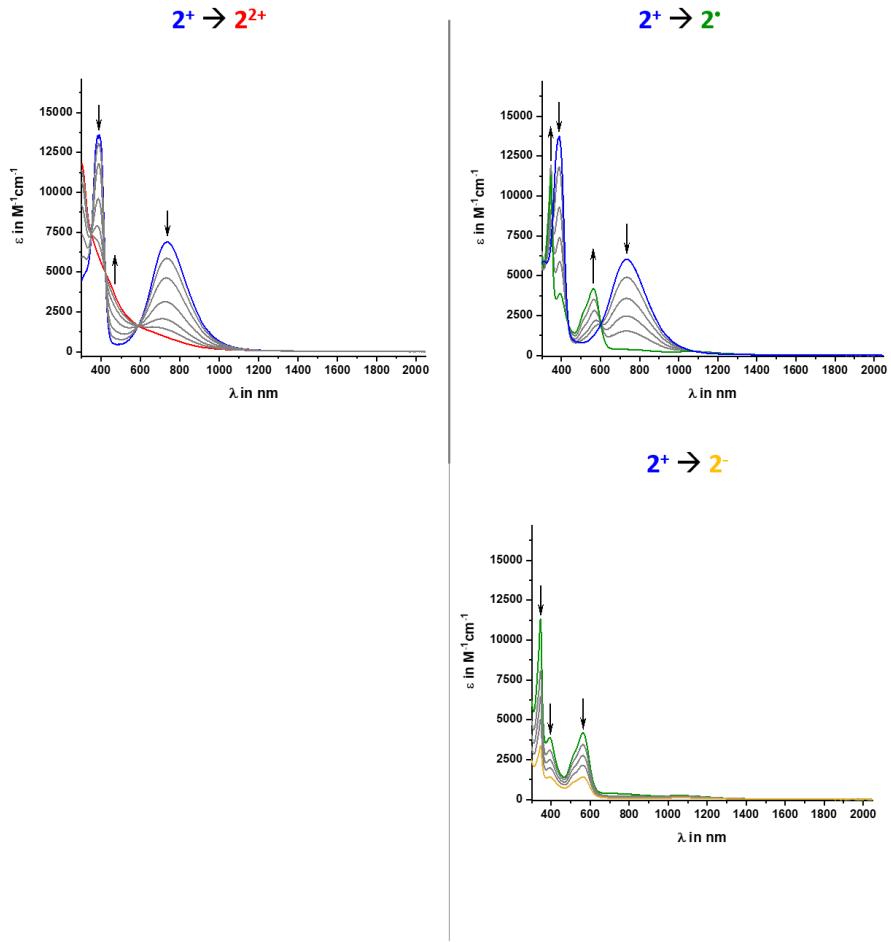
Figure S74: Spectroelectrochemistry of complex **2⁺.** Left: Oxidation from **2⁺** (blue line) to **2²⁺** (red line); top right: first reduction from **2⁺** (blue line) to **2•** (green line); bottom right: second reduction from **2•** (green line) to **2⁻** (yellow line).
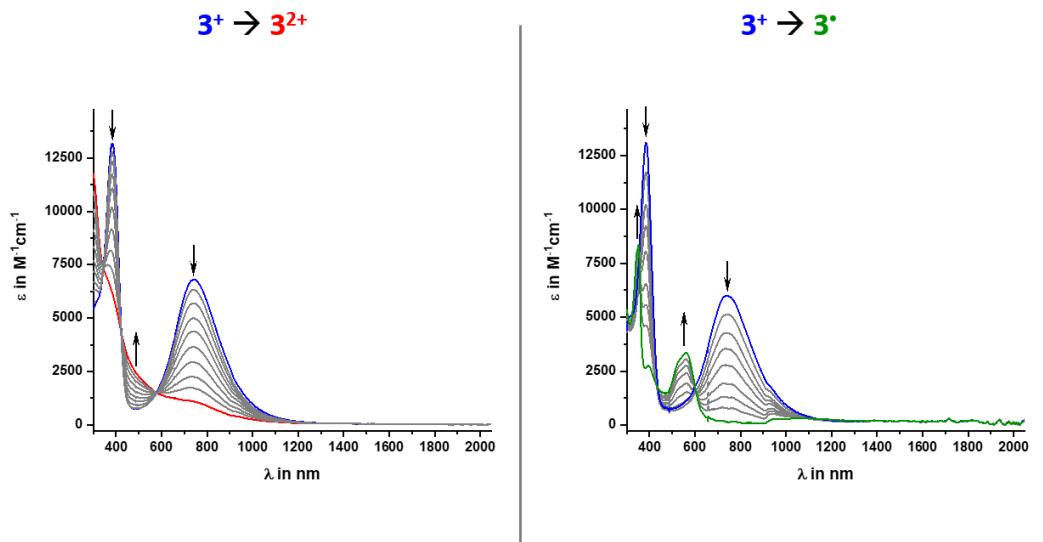
Figure S75: Spectroelectrochemistry of complex **3⁺**. Left: Oxidation from **3⁺** (blue line) to **3²⁺** (red line); right: reduction from **3⁺** (blue line) to **3•** (green line).
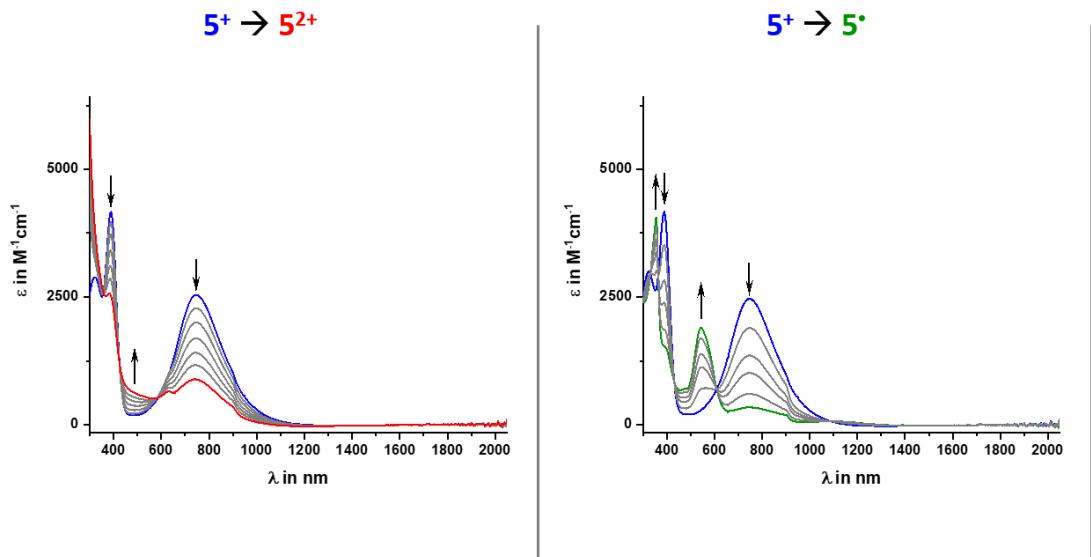
Figure S76: Spectroelectrochemistry of complex **5⁺**. Left: Oxidation from **5⁺** (blue line) to **5²⁺** (red line); right: reduction from **5⁺** (blue line) to **5•** (green line).
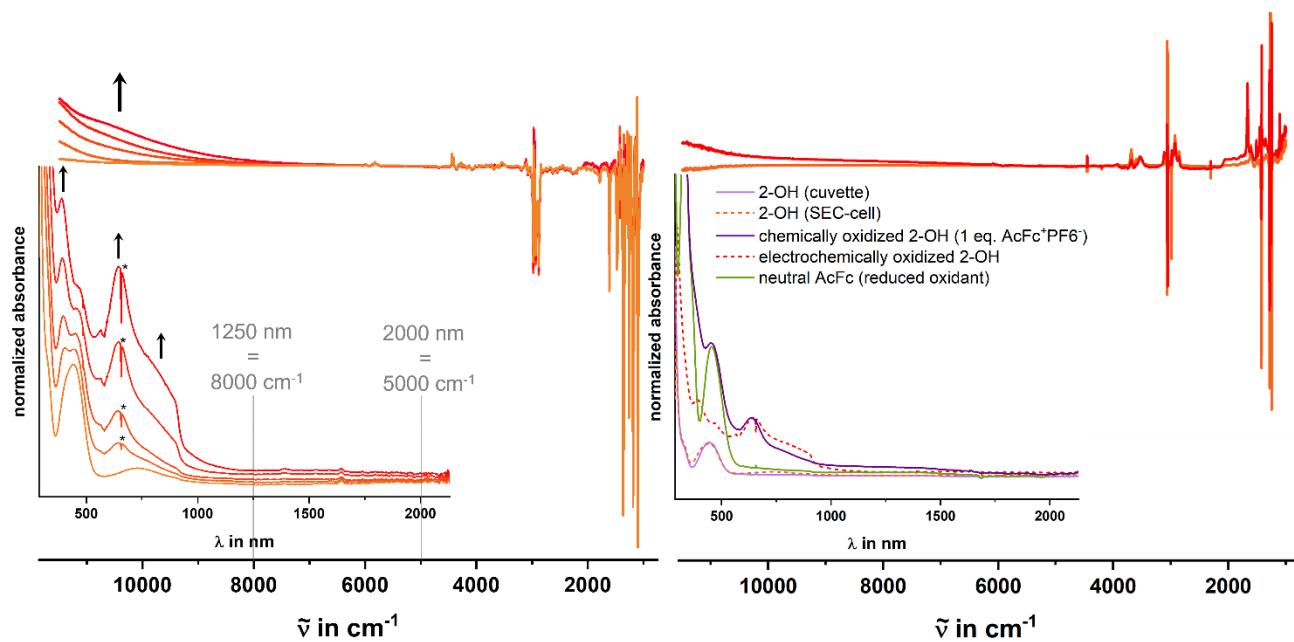
Figure S77: IR and Vis/NIR spectroelectrochemistry (left) and chemically oxidized (1 eq. acetylferrocenium PF$_6^-$) spectra (right) of complex **2-OH**. Left: Oxidation from **2-OH** (orange line) to **2-OH⁺** (red line); no IVCT bands are observed between 1250 nm (8000 cm^{-1}) and 2000 nm (5000 cm^{-1}); right: neutral carbinol **2-OH** (orange line in IR), chemically oxidized **2-OH⁺** (red line in IR), in the Vis/NIR spectrum: cf. legend; for comparison: neutral acetylferrocene (AcFc, green line) and data from electrochemistry (cf. dotted line), note that nm- and cm^{-1}-scales are not linearly comparable.

T-dependent and quantitative EPR Spectroscopy

Table S13: EPR data for all complexes.[a]

	g_{iso}[b]	DI (20°C)	c_{spin} [mM]	c_{spin}/c_{nom} [b,c]	dimer amount [b,c]
1°	2.0267	0.16	4.7 ±0.48	24 ±8	76 ±8
2°	2.0270	0.12	3.4 ±0.34	17 ±6	83 ±6
3°	2.0282	0.23	6.8 ±0.68	34 ±12	66 ±12
4°	2.0301	0.17	4.9 ±0.50	25 ±9	75 ±9
5°	2.0284	0.24	7.0 ±0.71	35 ±12	65 ±12

[a] All samples were reduced with a slight excess (1.1 equiv.) of cobaltocene and contained a nominal concentration c_{nom} of 20±5 mM. [b] At 20 °C. [c] in %.
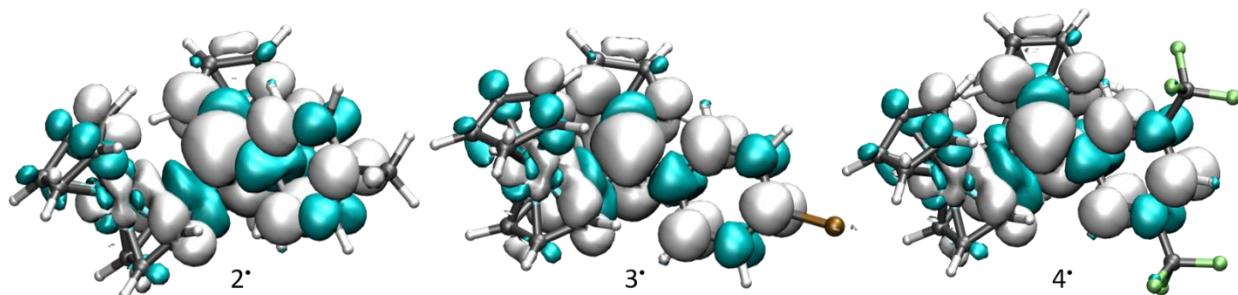

Figure S78: DFT-calculated spin density distributions for the reduced complexes **2°** - **4°**.

According to the Maxwell-Boltzmann relation of Equation 1, the signal intensity of a free radical is supposed to increase upon cooling due to a higher difference *ΔN* in occupancy between the ground and the excited states.

$$\Delta N \approx N \cdot \frac{g \cdot \mu_B \cdot B_0}{2 k_B T} \tag{1}$$
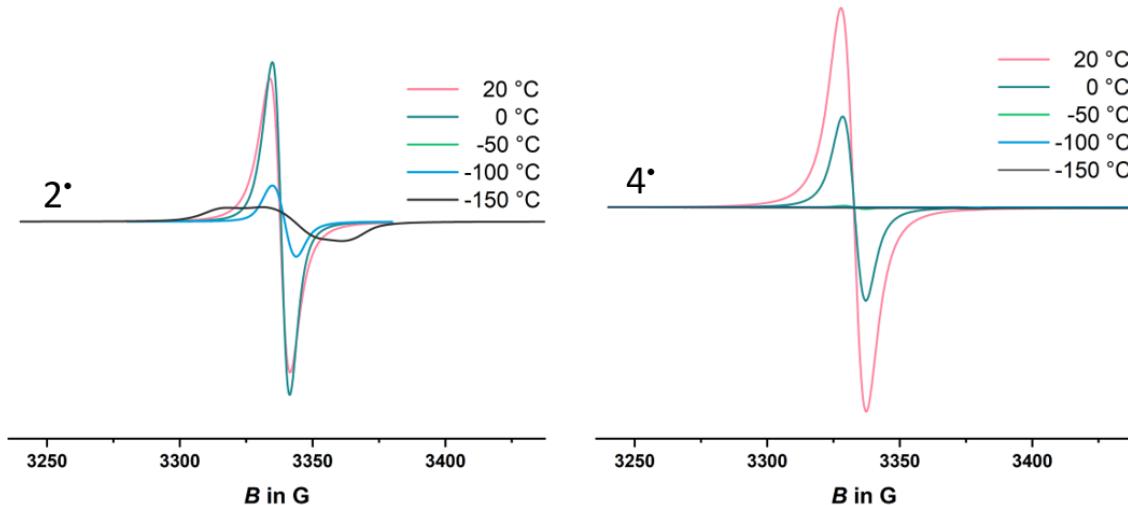
Figure S79: *T*-dependent EPR spectra of **2**$^\bullet$ and **4**$^\bullet$ recorded in CH_2Cl_2.

Spin counting quantification method

According to Eaton et al.,[1] the spin count of an EPR sample can be measured by its double integral DI through Equation 2. Therefore, it is crucial to use the same sample preparation and measurement parameters for every measurement. This has been ensured for all quantitative analysis of this work (cf. Experimental Section).

$$DI = c_{ns} \frac{\sqrt{P} \cdot B_m \cdot Q \cdot n_B \cdot S \cdot (S+1) \cdot n_s}{f(B_1, B_m)} \tag{2}$$

DI	Double Integral
c_{ns}	Setup constant
P	Microwave power
B_m	Modulation amplitude
Q	Resonator's quality factor
n_B	Boltzmann factor for temperature dependence
S	Total electron spin (1/2)
n_s	Number of spins in the sample
$f(B_1, B_m)$	Spatial distribution of microwave and modulation field in the sample

Evaluation of the data recorded at 20 °C has been done as follows:[2]

1) The background corrected spectrum (spectrum of pure CH_2Cl_2) was subtracted from the acquired spectrum
2) Zero-offset correction was applied
3) First integration was performed
4) Baseline correction of the first integration was applied
5) Second integration was performed
6) Double integral was determined from the results of the second integration
7) The spin concentration c_{spin} was determined *via* the linear equation established with the aid of the DPPH calibration curve (cf. Figure S80, Equation 3)
8) Calculated spin concentrations were then compared with the nominal concentrations c_{red} (Equation 4)
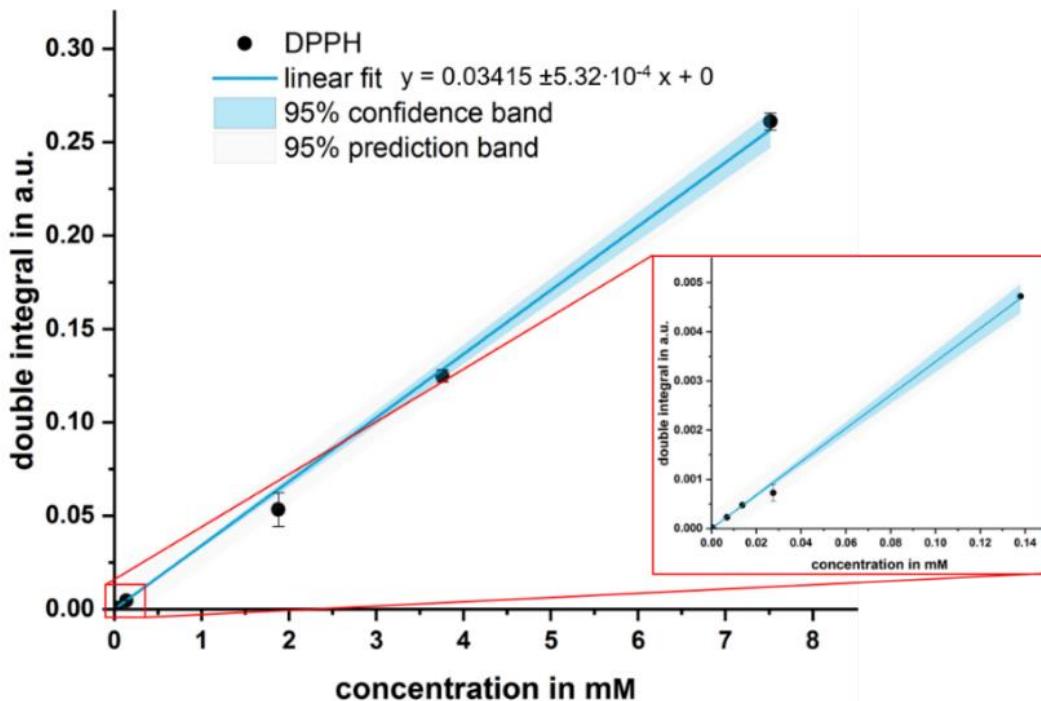

Figure S80: Calibration curve for quantitative EPR evaluation with 95% confidence and prediction band; lower right corner: magnification of the low concentration region.[2]

$$b(slope) = \frac{DI}{c_{spin}} \Rightarrow c_{spin} = \frac{DI}{b} = \frac{DI}{0.003415} \, mM \tag{3}$$

$$c_{red} = \frac{m}{M \cdot V} \tag{4}$$

Uncertainties (starting from: u_m = 0.05 mg, u_v = 50 µL, u_b = 5.32*10^{-4} for the calibration slope, u_{DI} = 10 % of the value of DI) were calculated using the GAUSSIAN formula for the propagation of uncertainties (**5-7**). Not included in these calculations is the error due to evaporation of solvent during sample preparation.

$$u_{c_{spin}} = \sqrt{\left(\frac{\partial c_{spin}}{\partial b} \cdot u_b\right)^2 + \left(\frac{\partial c_{spin}}{\partial DI} \cdot u_{DI}\right)^2} = \sqrt{\left(-\frac{DI}{b^2} \cdot u_b\right)^2 + \left(\frac{1}{b} \cdot u_{DI}\right)^2} \tag{5}$$

$$u_{c_{red}} = \sqrt{\left(\frac{\partial c_{red}}{\partial m} \cdot u_m\right)^2 + \left(\frac{\partial c_{red}}{\partial V} \cdot u_V\right)^2} = \sqrt{\left(\frac{1}{M \cdot V} \cdot u_m\right)^2 + \left(-\frac{m}{M \cdot V^2} \cdot u_V\right)^2} \tag{6}$$

$$u_{c_{spin}/c_{red}} = u_{ratio} = \sqrt{\left(\frac{\partial ratio}{\partial c_{spin}} \cdot u_{c_{spin}}\right)^2 + \left(\frac{\partial ratio}{\partial c_{red}} \cdot u_{c_{red}}\right)^2} \tag{7}$$

$$= \sqrt{\left(\frac{1}{c_{red}} \cdot u_{c_{spin}}\right)^2 + \left(-\frac{c_{spin}}{c_{red}^2} \cdot u_{c_{red}}\right)^2} \cdot 100 \ in \ [\%]$$

Table S13 compiles all quantitative data, including the measured double integrals DI, the derived spin concentrations c_{spin} and the concentrations of the complexes with their error margins, as well as a comparison between the two concentrations for all investigated complexes **1˙-5˙**. In the absence of dimerization, the concentration of the reduced complex in solution is expected to be equal to the nominal concentration of spins [as reduction should be complete using 1.1 eq. of cobaltocene as the reducing agent in a partially reversible reduction process as in this case, cf. CV]. As noted in Table S13, the spin concentrations are far lower than the complex concentrations suggesting a dimerization process with the difference between the two concentrations (100% - c_{spin}/c_{red}) amounting to the dimerization ratio.

References

1   G. R. Eaton, S. S. Eaton, D. P. Barr and R. T. Weber, *Quantitative EPR: A Practitioners Guide*, Springer Verlag, Vienna, Austria, 1st edn., 2010.

2   L. A. Casper, L. Wursthorn, M. Geppert, P. Roser, M. Linseis, M. Drescher and R. F. Winter, *Organometallics*, 2020, **39**, 3275–3289.